BLOOD-MIMICKING FLUID FOR BIOTECHNOLOGICAL APPLICATIONS.

FLUIDODYNAMIC BEHAVIOR OF RED BLOOD CELLS AND DROPLETS UNDER CONFINED SHEAR FLOW

Giovanna Tomaiuolo

Dottorato in Scienze Biotecnologiche – XXI ciclo
Indirizzo Biotecnologie Industriali
Università di Napoli Federico II

Dottorato in Scienze Biotecnologiche – XXI ciclo
Indirizzo Biotecnologie Industriali
Università di Napoli Federico II

BLOOD-MIMICKING FLUID FOR BIOTECHNOLOGICAL APPLICATIONS.

FLUIDODYNAMIC BEHAVIOR OF RED BLOOD CELLS AND DROPLETS UNDER CONFINED SHEAR FLOW

Giovanna Tomaiuolo

Dottoranda: Giovanna Tomaiuolo

Relatore: Prof. Stefano Guido

Coordinatore: Prof. Giovanni Sannia

“What is that feeling when you're driving away from people and they recede on the plain till you see their specks dispersing? It's the too huge world vaulting us, and it's goodbye. But we lean toward to the next crazy adventure beneath the skies”. Jack Kerouak - On the road, 1951

Ai miei genitori
A Francesco

Summary

Abstract

In spite of the development of cardio-vascular prosthetic devices, prosthetic heart valves, pulsatile blood pumps, models of the circulatory system, and sophisticated studies of flow through the complex geometries of the circulation, an analog test fluid with the rheological properties of blood is still lacking. The properties of blood pose several problems for quantitave applications as a test fluid: composition differs from donor to donor, precluding a fixed standard; properties change with time because of metabolic processes; opacity restricts optical studies of flow; blood samples can carry disease, thus presenting a biological hazard to workers; blood is a two phase, unstable system subject to sedimentation, and it can clot, thus blocking its fluid-like flow; the volume which can be withdrawn from a single donor is limited, restricting high volume applications.

To formulate a model blood fluid it is necessary to understand the rheological and fluidodynamic properties of blood and in particular of red blood cells (RBCs), because they form the major and the largest constituent of blood components. One of the most striking properties of red blood cells is their high deformability, which allows them to flow through vessels with radius smaller than cell size in microcirculation and is essential to maintain optimal blood circulation and gas transfer between blood and tissues. In this work, the attention was focussed on microconfined shear flow of RBCs in capillaries with radius comparable to average cell size. The main fluidodynamic observables are shape and velocity of the flowing RBCs, which depend on capillary radius, pressure drop, and RBC volume fraction in the capillary (referred to as tube hematocrit H_T). The microcapillaries are placed in a rectangular flow cell, where a suspension of RBCs is fed under the action of a liquid head in the physiological range. Video microscopy images of the flowing RBCs are acquired at high magnification and later processed by an automated image analysis macro. It was found that RBCs from healthy donors exhibit the classical parachute shape observed *in vivo*. Because the ability of red blood cell to deform and pass through capillaries is essential for continual flow of blood in the microvasculature, in this work was presented a novel tool for evaluating the impact of impaired deformability of RBCs on the flow of blood in the microvasculature by directly measuring perfusion of a test microchannel network (made by soft-lithography technique) with dimensions and topology similar to the real microcirculation. Furthermore, was analyzed the flow of deformable droplets of one Newtonian fluid suspended in another Newtonian fluid flowing in glass microcapillaries were. The resultant shapes of the liquid drops are similar to the shapes of red blood cells that have been observed in narrow glass capillaries as well as in blood vessels.

Riassunto

La formulazione di fluidi di interesse biologico e la relativa progettazione di sistemi di produzione è un'importante applicazione di biotecnologie industriali. In questo ambito un problema di particolare interesse è la verifica ed il controllo su base industriale di dispositivi medici cardiovascolari quali valvole cardiache protesiche, endoprotesi, assistenze ventricolari e dispositivi per circolazione extracorporea. Si tratta di un test cruciale, data la possibilità che, una volta impiantati, i dispositivi producano un danno a carico dei costituenti ematici a causa delle condizioni non fisiologiche del flusso generato. Attualmente, per testare i dispositivi medici artificiali, viene usato sangue bovino (molto costoso) o una soluzione newtoniana di acqua e glicerina che non riesce a mimare completamente e correttamente le complesse proprietà reologiche e fluidodinamiche del sangue umano. Il sangue è un fluido non-newtoniano costituito dagli elementi figurati (globuli rossi, bianchi e piastrine) e dal plasma; gli elementi del sangue con maggiore influenza sulla reologia e la fluidodinamica sono i globuli rossi, a causa della loro elevata concentrazione. Caratteristiche principali dei globuli rossi sono la forma a disco biconcavo, la capacità di deformarsi sotto gli sforzi applicati e la tendenza ad aggregarsi tra loro. Tra le proprietà reologiche, la viscosità del sangue è fortemente influenzata dalla deformabilità e dalla aggregazione dei globuli rossi, dall'ematocrito e dalla viscosità del plasma. E' quindi necessario conoscere in maniera approfondita le caratteristiche reologiche e fluidodinamiche del sangue e in particolare dei globuli rossi. L'obiettivo, quindi, di questo lavoro di tesi è la formulazione di un fluido modello avente proprietà reologiche simili a quelle del sangue umano (blood mimicking fluid) atto a testare e migliorare le performance di dispositivi medici artificiali.

Flusso di globuli rossi in microcapillari

La deformabilità dei globuli rossi circolanti nei vasi di piccolo calibro è una proprietà essenziale per mantenere un flusso ottimale e per consentire gli scambi gassosi fra sangue e tessuti. La misura della deformabilità e aggregazione dei globuli rossi è stata oggetto di numerosi studi in letteratura, con particolare enfasi sul flusso in capillari. Nella maggior parte degli studi sono stati utilizzati microcanali di dimensioni paragonabili ai capillari in vivo. Nella prima parte di questo lavoro di tesi l'attività di ricerca si è concentrata sulla messa a punto di un apparato sperimentale atto ad analizzare a morfologia e velocità di globuli rossi in flusso di scorrimento confinato in condotti artificiali di dimensioni paragonabili a quelle cellulari.

Apparato sperimentale

Negli esperimenti per lo studio della velocità e deformabilità di globuli rossi è stata progettata una cella di flusso (Figura 1a) costituita da due lastre di plexiglass trasparente separate da uno spaziatore di gomma; nella lastra inferiore c'è uno scavo atto all'inserimento di un vetrino (circa 0.13 mm di spessore) per l'osservazione ad alto ingrandimento con obiettivi ad immersione. Sulla lastra inferiore della cella di flusso sono stati alloggiati dei microcapillari di vetro (Figura 1b) con diametro compreso tra 4.7 e 10 μm. I due fori presenti sulla lastra superiore della

cella di flusso sono collegati a due tubi di gomma, connessi agli estremi liberi a due beaker contenenti la soluzione diluita di globuli rossi. Quest'ultima è costituita da 100

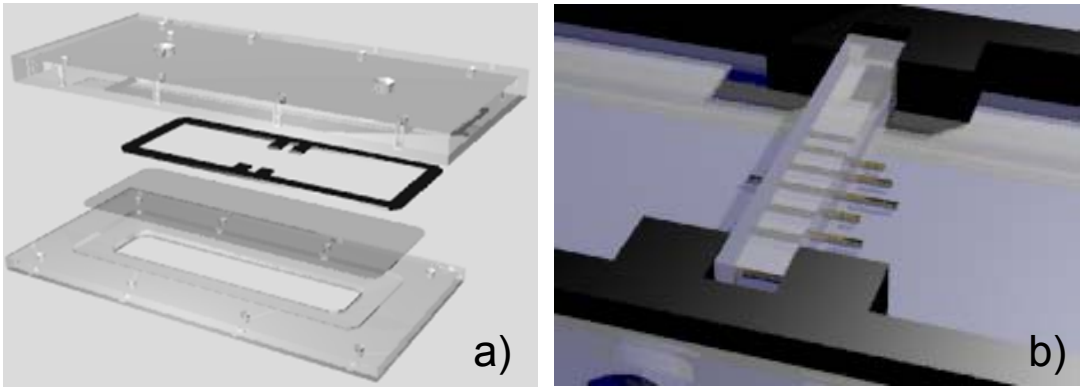

Figura 1: (a) Componenti della cella di flusso; (b) microcapillari di vetro

ml di anticoagulante ACD, 5 ml di albumina umana e 1 ml di sangue intero proveniente da volontari sani ed utilizzato entro quattro ore dal prelievo. Il flusso nei microcapillari viene controllato variando la distanza tra il pelo libero di soluzione nel contenitore d'ingresso e quello di uscita. E' stata utilizzata una videocamera ad elevata velocità per acquisire le immagini dei globuli rossi in flusso, che sono successivamente state elaborate con software di analisi dell'immagine per determinare velocità e morfologia delle cellule.

Risultati

I risultati ottenuti evidenziano caratteristiche fluidodinamiche osservato *in vivo*, come la classica forma a paracadute. In figura 2a viene mostrata la forma di globuli rossi in funzione del diametro del capillare e della velocità della cellula stessa.

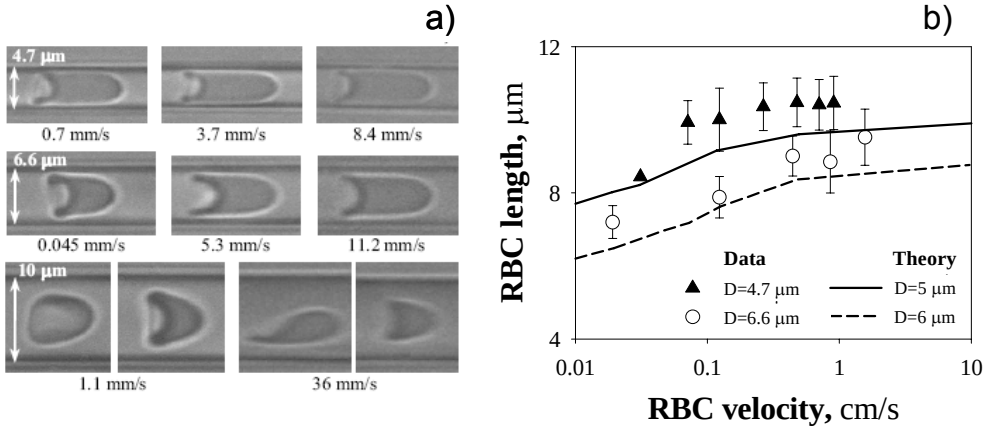

Figura 2: (a) Immagini di globuli rossi in microcapillari di diverso diametro; (b) lunghezza dei globuli rossi in funzione della velocità

Usando tecniche di analisi delle immagini è stato osservato che tale forma varia in funzione del diametro del capillare e della velocità; in particolare, è stato possibile misurare la lunghezza di un globulo rosso come l'asse maggiore rettangolo in cui il globulo è inscritto. Tale dimensione aumenta man mano che diminuisce il diametro del capillare in quanto il globulo rosso tende a schiacciarsi per attraversare un capillare più piccolo della sua dimensione caratteristica. Inoltre la lunghezza del

globulo aumenta all'aumentare della velocità (Figura 2b) fino a raggiungere un valore asintotico. Questi risultati sono stai confrontati con un modello teorico (Secomb 1986) ed è stato riscontrato un ottimo accordo tra i risultati sperimentali e i dati di letteratura. In Figura 3 è diagrammata la velocità dei globuli rossi in flusso in capillari di diverso diametro (4.7, 6.6 e 10 μm) in funzione della pressione imposta. Si può notare che la velocità dei globuli rossi aumenta linearmente all'aumentare della pressione imposta ΔP e che dipende dal diametro del capillare in cui fluiscono: globuli rossi in capillari di diametro pari a 10 μm hanno velocità maggiori rispetto a quelli in capillari di diametro pari a 4.7 μm. La linee solida rappresenta la velocità media del fluido sospendente calcolata utilizzando l'equazione di Poiseuille (Eq.1), dove R e L sono rispettivamente il raggio e la lunghezza del capillare, ΔP la pressione imposta e μ la viscosità calcolata utilizzando un viscosimetro a capillare.

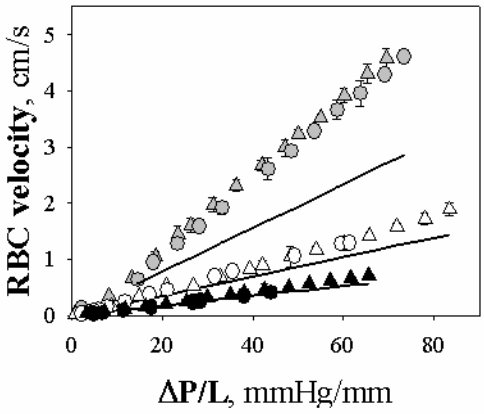

Figura 3: Velocità vs ΔP a D = 4.7, 6.6e 10 μm.

$$\langle v_z \rangle = \frac{\Delta P R^2}{8 \mu L} \qquad \text{Eq. 1}$$

Analizzando più campioni di sangue provenienti da diversi donatori è stata generata una vera e propria "master curve" della velocità di globuli rossi sani in funzione del ΔP. In altre parole, il comportamento dei globuli rossi sani in flusso in microcapillari non dipende dal donatore (sano), ma può essere usato come riferimento a cui paragonare situazioni patologiche.

Microdispositivi per simulare la microcircolazione

Parallelamente è stata messa a punto una tecnica tipo *microfluidics* per la creazione di una rete di microcanali di geometria tale da riprodurre le caratteristiche del microcircolo sanguigno umano. Per la realizzazione di tali microcanali è stata usata una tecnica nota come soft-lithography.

Soft-lithography

Per microfluidica si intende la scienza e la tecnologia di sistemi che processano piccole quantità di fluido usando canali di dimensioni dai 10 ai 100 mm. Il poter eseguire analisi precise e veloci e soprattutto a basso costo e con un consumo minimo di materiale è di grande interesse in campo biomedico. La tecnologia utilizzata per la creazione di canali di piccole dimensioni è nota come litografia. Con la litografia è possibile trasferire un disegno voluto da una maschera su uno strato di resist (una sostanza fotosensibile) spalmato su di un substrato. Ciò avviene

attraverso due passi distinti: esposizione a raggi UV sviluppo, ovvero rimozione selettiva di alcune parti di resist. La fotomaschera utilizzata è una lastra di quarzo trasparente ai raggi UV (Figura 4a), coperta da un sottile strato di cromo (100nm); su di essa è riprodotto il *pattern* che si intende riportare sullo strato di resist. I disegni delle reti di microcanali che costituiscono la maschera sono stati realizzati utilizzando un software commerciale per il disegno di microcircuiti elettrici (LASI 7). In particolare si è scelto di riprodurre reti di microcanali che potessero simulare il microcircolo sanguigno (Figura 4b).

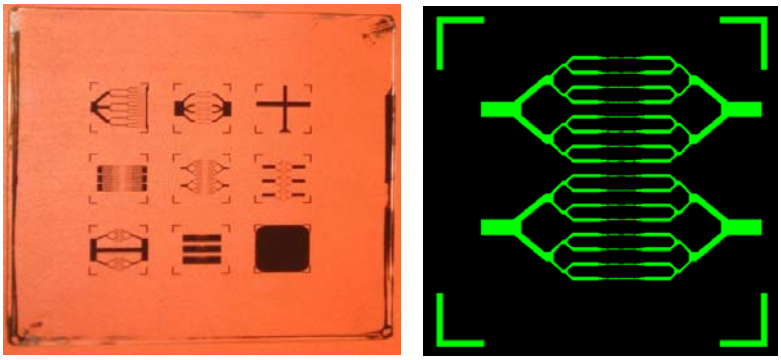

Figura 4: (a) Fotomaschera al cromo; (b) particolare disegno di microcanali 1cm x 1cm

Il master di resist ottenuto servirà da stampo per la creazione di microcanali in materiale elastomerico, in particolare silicone (*polidimethylsiloxane* o PDMS), per questo motivo tale tipo di litografia è noto come soft-lithography. Il PDMS è un silicone elastomerico inerte chimicamente, trasparente ed elastico; è costituito da due elementi: la base e l'agente di curing. La preparazione del PDMS viene eseguita mescolando la base e l'agente di curing in rapporto in peso di 10:1. Un volta preparato il PDMS è possibile procedere alla creazione dei microcanali: si ricopre il master di resist con una goccia di PDMS liquido, si pone in forno a circa 150 °C e si aspetta che il materiale polimerizzi. Una volta indurito, il PDMS può essere rimosso dalla superficie del master ed essere attaccato su di un vetrino. Per far aderire in modo irreversibile il PDMS (contenente la rete di microcanali) si utilizza uno strumento chiamato *Laboratory Corona Treater*. Il LCT modifica la superficie del PDMS (da idrofoba a idrofila) mediante ioni elettrici altamente carichi e crea legami irreversibili tra la superficie del PDMS e quella del vetro.
In Figura 5 sono mostrati i microcanali realizzati in PDMS a diverso ingrandimento.

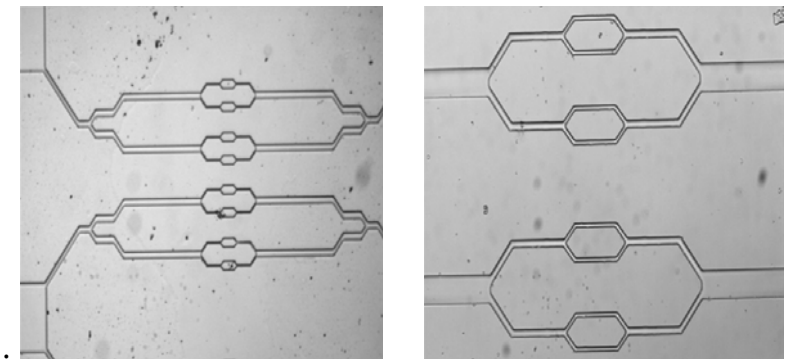

Figura 5: Microcanali in PDMS

Risultati

Prima di tutto è stato verificato che l'utilizzo di canali a sezione rettangolare piuttosto che circolare non compromettesse l'analisi di grandezze fluidodinamiche, come per esempio la velocità. In figura 6 si può notare come l'andamento della velocità dei globuli rossi misurata in microcanali con diametro equivalente pari a 8.5 sia in buon accordo con quella calcolata in capillari con diametro pari a 6.6 e 10 μm.

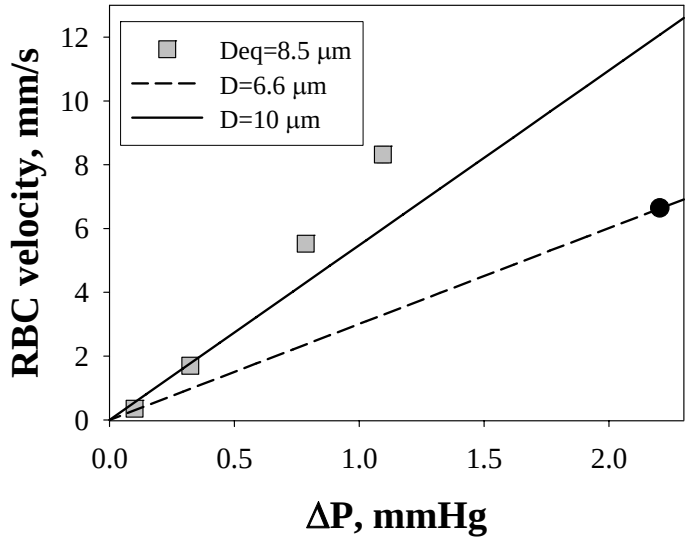

Figura 6: Velocità vs ΔP in microcanali e microcapillari

E' stata poi valutato l'andamento della velocità (a un ΔP fissato) di un globulo rosso in una canale a sezione variabile, in particolare in un divergente, funzione della sua posizione nel canale (Figura 7); la velocità diminuisce all'aumentare della sezione del microcanale, come ci ricorda l' equazione di continuità.

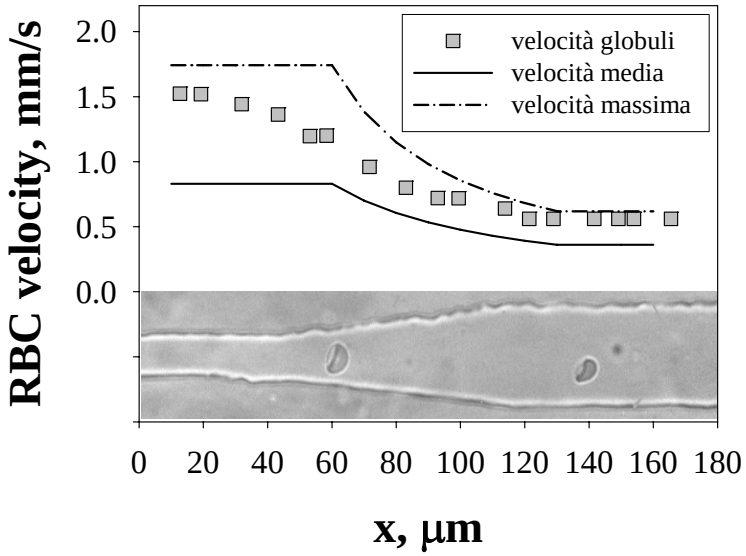

Figura 7: Velocità in un canale divergente

Nel grafico sono anche riportate, con linea solida e tratteggiata, rispettivamente la velocità media e massima calcolate del fluido sospendente.
La velocità dei globuli rossi inizialmente (nel tratto più stretto a sezione costante) ha valori compresi tra le velocità media e massima calcolate poi, man mano che la sezione aumenta, si avvicina sempre, fino a raggiungere, la velocità massima poiché non si risente più dell'effetto dell'effetto delle pareti. Le stesse miure sono state portate aventi al variare della pressione imposta: naturalmente la velocità diminuisce al diminuire del ΔP.

Formulazione di un fluido modello del sangue

Le conoscenze acquisite sul comportamento reologico del sangue sono state il punto di partenza per la formulazione di un fluido modello, con proprietà reologiche e meccaniche simili al sangue. Di notevole interesse in questo senso, risulta essere il sistema costituito da una goccia di fluido dispersa in matrice entro un capillare di dimensioni paragonabili a quelle della goccia stessa. Si è iniziato con l'analizzare il caso più semplice di un sistema composto da una goccia sottoposta a flusso di shear microconfinato, per approdare quindi ad un sistema che permetta di studiare il flusso microconfinato in microcapillari, situazione molto vicina a quella d'interesse. La scala dimensionale del sistema modello è stata, per semplicità di analisi, di due ordini di grandezza maggiore (decine di mm). Il flusso in microcapillari invece tramite un sistema di pompe a siringa e microcapillari di silica opportunamente assemblati.

Materiali e metodi

Il sistema modello utilizzato è stato: per la matrice esterna PolyButene, avente una viscosità η_c di circa 0.26 Pa·s a 23 °C, mentre per la fase dispersa è stata utilizzata una miscela di Oli Siliconici di concentrazione tale da ottenere rapporto di viscosità λ=1 o 4. Le misure di viscosità sono state effettuate usando il reometro rotazionale a stress controllato (Bohlin CVO 120). Entrambi i fluidi possono essere considerati Newtoniani nel range di stress di interesse (10^{-2} – 10^{2} Pa). L'apparato sperimentale utilizzato è costituito da una cella di flusso costituita da due vetrini di 50x50x1 mm, tra i quali vengono posti tre capillari con una estremità confluente, non a contatto, due di essi sono coassiali, il loro asse coincide con la direzione del flusso, il terzo è perpendicolare all'asse di flusso. I capillari, di vetro, hanno diametro interno di 319 µm. In Figura 8 sono riportate alcune immagini acquisite durante l'iniezione della goccia nel capillare.

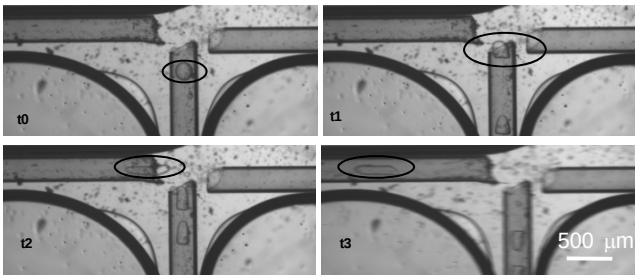

Figura 8: Fase di iniezione della goccia nel capillare di flusso

Misurato il contorno della goccia in flusso all'interno del capillare, ne è stato calcolato il volume, approssimando la goccia ad un solido di rotazione, ed il raggio della goccia indeformata (a) per conservazione del volume. È stato quindi misurato il profilo di velocità parabolico nel capillare in assenza di gocce, aggiungendo delle sfere di polistirene (9.7 μm) come tracciante alla fase continua. La velocità media del flusso (V) è stata calcolata come parametro di fit dell'equazione di Poiseuille. Il fenomeno della deformazione della goccia in flusso micro confinato, oltre che dai parametri a e V, dipende anche da: Velocità della goccia (U), Viscosità della fase dispersa (η_d) e continua (η_c), Tensione interfacciale tra le fasi (σ), Asse maggiore della goccia deformata (L), Raggio del capillare (R). Questi parametri consentono di definire i seguenti gruppi adimensionali, descrittivi del fenomeno: il numero di Capillare ($Ca = V\eta_c/\sigma$), il rapporto tra le viscosità delle due fasi $\lambda = \eta_d/\eta_c$, un parametro geometrico $K = a/R$.

Risultati

In Figura 9 sono rappresentati gli start up del flusso, riportando il parametro di deformazione (L/2a) in funzione del tempo di flusso adimensionale (Vt/D), a partire da una condizione statica, per gocce di diverse dimensioni, caratterizzate cioè da un differente parametro geometrico K, tutte soggette allo stesso numero di capillare = 0.6. Si nota che al crescere di K cresce il tempo richiesto per raggiungere la deformazione stazionaria. Per K > 1, si nota che al tempo zero, a flusso assente, il parametro di deformazione è maggiore dell'unità, in quanto la goccia inserita in un capillare più piccolo delle sue dimensioni non è sferica.

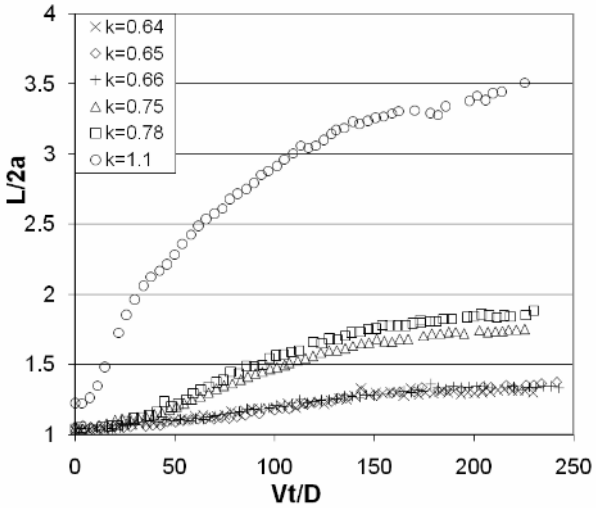

Figura 8: Transitorio a Ca = 0.6, λ=1. Lunghezza adimensionale in funzione del tempo adimensionale, parametrico in K.

In Figura 9 si riporta la dipendenza dei transitori dal numero di capillare, analizzando due gocce aventi K = 1.1 soggette a diversi Ca. Anche in questo caso, il tempo per raggiungere lo stazionario aumenta al crescere di Ca.

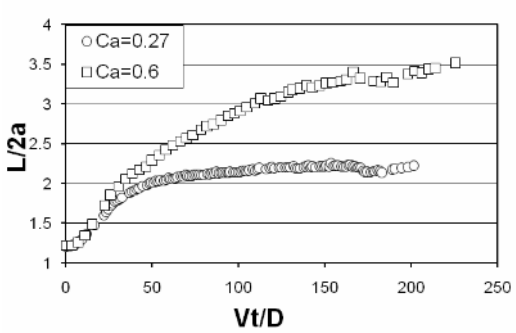

Figura 4: Transitorio a K = 1.1, λ=1. Lunghezza adimensionale in funzione del tempo adimensionale, parametrico in Ca.

In Figura 10 sono riportate delle immagini di gocce allo stazionario corrispondenti a differenti valori di K e di portata nominale imposta (Q). Si evince chiaramente come a bassi valori di K, la goccia si discosti solo di poco dalla sua forma iniziale sferica, mentre assume una forma più pronunciata al crescere del numero di capillare. L'effetto di quest'ultimo si risente maggiormente in corrispondenza di K >1, laddove la goccia inizia ad assumere una forma "a proiettile", con una punta diretta come il flusso, proprio come avviene nel caso dei globuli rossi.

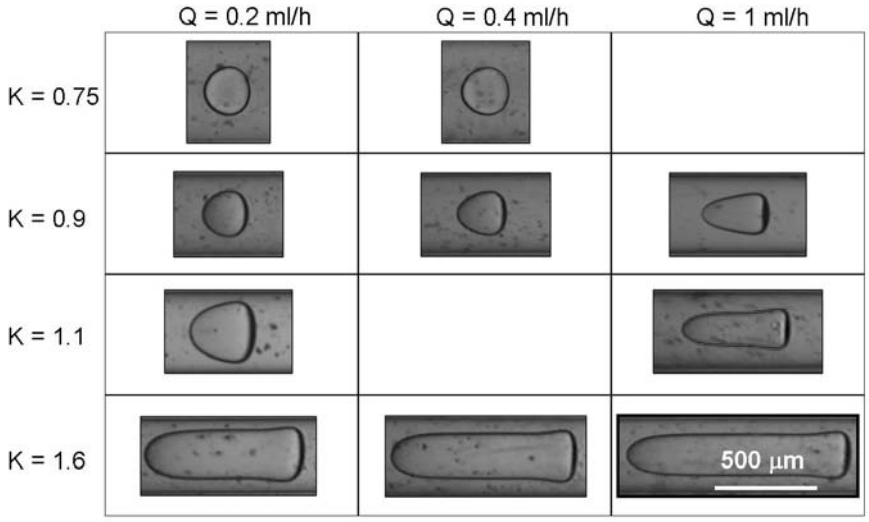

Figura 10: Morfologia della goccia allo stazionario,al variare di K e Q. λ=4.

Conclusioni

In conclusione, i risultati raggiunti in questo lavoro di tesi di dottorato possono essere così riassunti:

- ✓ Messa a punto di un apparato per l'analisi della deformabilità dei globuli rossi durante il flusso in microcapillari
- ✓ Messa a punto di una tecnologia tipo microfluidics per simulare la fluidodinamica del sangue nella microcircolazione
- ✓ Messa a punto di un apparato per l'analisi di gocce di dimensioni paragonabili a quelle del capillare durante il flusso di shear semplice ed il flusso di microcapillari
- ✓ La forma delle gocce durante il flusso alla Poiseulle, per λ ≥ 1, richiama quella eritrocitaria, e quindi possono essere un buon modello dei globuli rossi.

Chapter 1 BLOOD MIMICKING FLUID

1.1 INTRODUCTION

The development of blood-contacting artificial organs requires that special attention be paid to blood damage that occurs during the device operation. Generally, blood trauma remains a key challenge in the development and improvement of heart-assist devices, blood oxygenators, dialysis machines and peripheral access systems. For example, the major bioengineering challenge in the design of a permanent artificial heart is the reduction of blood damage within the pump, cannulae, and connectors. Because, by definition, these devices must augment the pressure and blood flow delivered to the circulatory system, it is difficult to completely avoid the extremely high shear stress, turbulence, and other hemodynamic and surface related factors which can cause hemolysis and thrombosis. These factors togheter with possible heat generation may cause mechanical destruction of some erythrocytes (i.e. hemolysis) and changes in their mechanical properties. Hemolysis starts when the RBC membrane stretches, developing holes, and leaks hemoglobin. Free hemoglobin in the blood stream is toxic. Catastrophic hemolysis occurs when the RBC membrane ruptures.
Moreover, the critical importance of timely replenishment of blood loss, whether due to injury or surgery, has led to large-scale efforts to develop blood substitutes over the past 20 years. Despite the research and development efforts of many laboratories, both public and private, no substitute has yet been developed that can carry out the essential functions that whole blood performs in the circulatory system and especially in the microcirculation.
The cardiovascular device industry drives a strong need for tools to facilitate the development of blood-contacting technologies rapidly and inexpensively. Traditional cardiovascular device development involves multiple phases that typically require in vivo evaluation of safety of prototype designs in animals, often for several iterations, before product design freeze. These iterations are costly and time-consuming. The ability to pre-screen blood circuits utilizing accurate, simulations validated through follow-up in vivo safety studies, would result in the selection of optimal blood circuit geometries and flow conditions before implementation in animal and clinical studies and in substantial reduction of design iteration cycle times and of the cost of animal studies and numbers of animals required.
In spite of the development of artificial devices an analog test fluid with the rheological properties of blood is still lacking and it is an important biotechnological and environmental engineering application.
There is a need to better understand how the special characteristics of blood and its flow properties make it such an effective means for delivery and exchange in the microcirculation.

1.2 HUMAN BLOOD

Blood is a specialized bodily fluid that performs many important functions within the body including:

- Supply of oxygen to tissues (bound to hemoglobin which is carried in red cells). About 98.5% of the oxygen in a sample of arterial blood in a healthy human breathing air at sea-level pressure is chemically combined with the hemoglobin (Hgb). About 1.5% is physically dissolved in the other blood liquids and not connected to Hgb. The hemoglobin molecule is the primary transporter of oxygen. With the exception of pulmonary and umbilical arteries and their corresponding veins, arteries carry oxygenated blood away from the heart and deliver it to the body via arterioles and capillaries, where the oxygen is consumed; afterwards, venules and veins carry deoxygenated blood back to the heart. Under normal conditions in humans at rest, hemoglobin in blood leaving the lungs is about 98-99% saturated with oxygen. In a healthy adult at rest, *deoxygenated* blood returning to the lungs is still approximately 75% saturated.
- Supply of nutrients, such as amino acids and fatty acids (dissolved in the blood or bound to plasma proteins (e.g. blood lipids).
- Removal of waste such as carbon dioxide, urea and lactic acid.
- Immunological functions, including circulation of white cells, and detection of foreign material by antibodies. In mammals, blood is in equilibrium with lymph, which is continuously formed in tissues from blood by capillary ultrafiltration. Lymph is collected by a system of small lymphatic vessels and directed to the thoracic duct, which drains into the left subclavian vein where lymph rejoins the systemic blood circulation.
- Coagulation, which is one part of the body's self-repair mechanism.
- Messenger functions, including the transport of hormones and the signaling of tissue damage.
- Regulation of body pH (the normal pH of blood is in the range of 7.35 - 7.45).
- Regulation of core body temperature. Blood circulation transports heat throughout the body, and adjustments to this flow are an important part of thermoregulation. Increasing blood flow to the surface (e.g. during warm weather or strenuous exercise) causes warmer skin, resulting in faster heat loss, while decreasing surface blood flow lowers heat transport.
- Hydraulic functions. The restriction of blood flow can also be used in specialized tissues to cause engorgement resulting in an erection of that tissue.

The average adult has a blood volume of roughly 5 litres, composed of plasma and several kinds of cells (called *corpuscles or formed elements*); these are erythrocytes (red blood cells - RBCs), leukocytes (white blood cells) and thrombocytes (platelets). About 55% of whole blood is blood plasma, a fluid that is the blood liquid medium, which by itself is straw-yellow in color. The blood plasma volume totals of 2.7-3.0 litres in an average human. It is essentially an aqueous solution containing 92% water, 8% blood plasma proteins, and trace amounts of other materials. Plasma circulates dissolved nutrients, such as glucose, amino acids and fatty acids (dissolved in the blood or bound to plasma proteins), and removes waste products, such as carbon dioxide, urea and lactic acid. Other important components include: serum albumin, blood clotting factors (to facilitate coagulation), immunoglobulins (antibodies), lipoprotein particles, various other proteins, various electrolytes (mainly sodium and chloride). Plasma also circulates hormones transmitting their messages to various tissues.

The normal pH of human arterial blood is approximately 7.40 (normal range is 7.36-7.44), a weak alkaline solution. Blood pH, partial pressure of oxygen (P_{O_2}), partial pressure of carbon dioxide(P_{CO_2}) and HCO_3 are carefully regulated by a number of homeostatic mechanisms, which principally exert their influence through the

respiratory system and the urinary system in the control of the acid-base balance and respiration.

The various cells of blood are made in the bone marrow in a process called hematopoiesis, which includes erythropoiesis, the production of red blood cells, and myelopoiesis, the production of white blood cells and platelets. During childhood, almost every human bone produces red blood cells; as adults, red blood cell production is limited to the larger bones: the bodies of the vertebrae, the breastbone (sternum), the ribcage, the pelvic bones, and the bones of the upper arms and legs. In addition, during childhood, the thymus gland, found in the mediastinum, is an important source of lymphocytes. The proteinaceous component of blood (including clotting proteins) is produced predominantly by the liver, while hormones are produced by the endocrine glands and the watery fraction is regulated by the hypothalamus and maintained by the kidney.

Healthy erythrocytes have a plasma life of about 120 days before they are degraded by the spleen, and the Kupffer cells in the liver. The liver also clears some proteins, lipids and amino acids. The kidney actively secretes waste products into the urine.

One microliter of blood contains:

- 4.7 to 6.1 million (male), 4.2 to 5.4 million (female) erythrocytes**:** in mammals, mature red blood cells lack a nucleus and organelles. They contain the blood hemoglobin and distribute oxygen. Hemoglobin is the principal determinant of the color of blood in vertebrates. Each molecule has four heme groups, and their interaction with various molecules alters the exact color. In vertebrates and other hemoglobin-using creatures, arterial blood and capillary blood are bright red as oxygen imparts a strong red color to the heme group. Deoxygenated blood is a darker shade of red; this is present in veins, and can be seen during blood donation and when venous blood samples are taken. Blood in carbon monoxide poisoning is bright red, because carbon monoxide causes the formation of carboxyhemoglobin. In cyanide poisoning, the body cannot utilize oxygen, so the venous blood remains oxygenated, increasing the redness. While hemoglobin containing blood is never blue, there are several conditions and diseases where the color of the heme groups make the skin appear blue. If the heme is oxidized, methemoglobin, which is more brownish and cannot transport oxygen, is formed. In the rare condition sulfhemoglobinemia, arterial hemoglobin is partially oxygenated, and appears dark-red with a bluish hue (cyanosis). The red blood cells (together with endothelial vessel cells and other cells) are also marked by glycoproteins that define the different blood types. The proportion of blood occupied by red blood cells is referred to as the hematocrit (Hct), and is normally about 45%. The combined surface area of all the red cells in the human body would be roughly 2,000 times as great as the body's exterior surface.
- 4,000-11,000 leukocytes**:** white blood cells are part of the immune system; they destroy and remove old or aberrant cells and cellular debris, as well as attack infectious agents (pathogens) and foreign substances. The cancer of leukocytes is called leukemia.
- 200,000-500,000 thrombocytes**:** thrombocytes, also called platelets, are responsible for blood clotting (coagulation). They change fibrinogen into fibrin. The fibrin creates a mesh onto which red blood cells collect and clot, which then stops more blood from leaving the body and also helps to prevent bacteria from entering the body.

Therefore, RBCs form the major and the largest constituent of formed elements (99%). They behave as neutrally buoyant microcapsules with tremendous deformabilty but small areal stretchability. A RBC at rest is a biconcave disc (Figure 1-1); its membrane has a relaxation time of approximately 200 ms which depends on the age of the cell and it can support an estimated areal strain of 6% before rupture. Owing to its biconcave shape, a RBC has 40% excess surface area compared to a sphere of the same volume. The excess surface enables RBCs to undergo both volume and surface area preserving deformations.

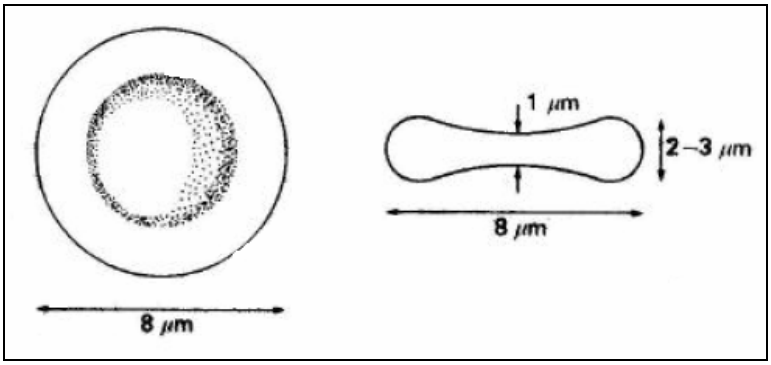

Figure 1-1: Red blood cell shape at rest

1.3 PRINCIPLES OF RHEOLOGY

Rheology is the scientific field that deals with the flow and deformation behavior of materials, with the materials under consideration being solids or fluids, including liquids and gases. *Deformation* can be defined as the relative displacement of material points within the body. Solids react to the application of a force by a given deformation. If a solid is elastic, the deformation is proportional to the applied force, and, if the deformation is not too large, the original shape is recovered when the force is removed. If a permanent deformation remains after the removal of force, the solid is said to be plastic. Fluids continuously deform - or flow - as a result of the application of external forces. Some materials exhibit viscoelastic behavior, which is a combination of fluid-like and solid-like behavior. In studying the degree of deformation (or flow) of a material, the force applied per unit area must be considered. This deforming force, called *stress*, may have several components, including shear stress, the force per unit area acting parallel to the surface, and normal stress, the force per unit area acting perpendicular to the surface. The latter is defined as pressure in a fluid. The degree of deformation is called *strain*, which also has various components associated with the different stress components. For example, shear stress results in shear strain, in which the layers of material move parallel to each other in a continuous manner. During slow flow in a tube the pressure drop (reflecting the resistance to flow) is proportional to the speed of flow. Under these conditions, it has been observed that the liquid particles move smoothly in adjacent planes (laminae) parallel to the tube wall; this type of flow is called *laminar flow*.

With increasing flow rate, there is a tendency for the fluid flow to become irregular, with fluid moving in swirls and irregular patterns. This type of chaotic flow is termed turbulent, with the degree of turbulence increasing with flow rate. Under such

turbulent conditions, the pressure drop is proportional to the square of the speed of flow, and thus for the same pipe and fluid, resistance to flow is greater with turbulence than it is for laminar flow.
Under laminar flow conditions, a shear stress - shear rate relationship is used to define the fluidity of liquids. This relationship reflects the internal resistance between fluid layers (laminae) and thus reflects the viscosity of the fluid; the viscosity of a liquid can be calculated by dividing the shear stress by the shear rate. From a rheological point of view, liquids can be divided into two main groups (Figure 1-2):

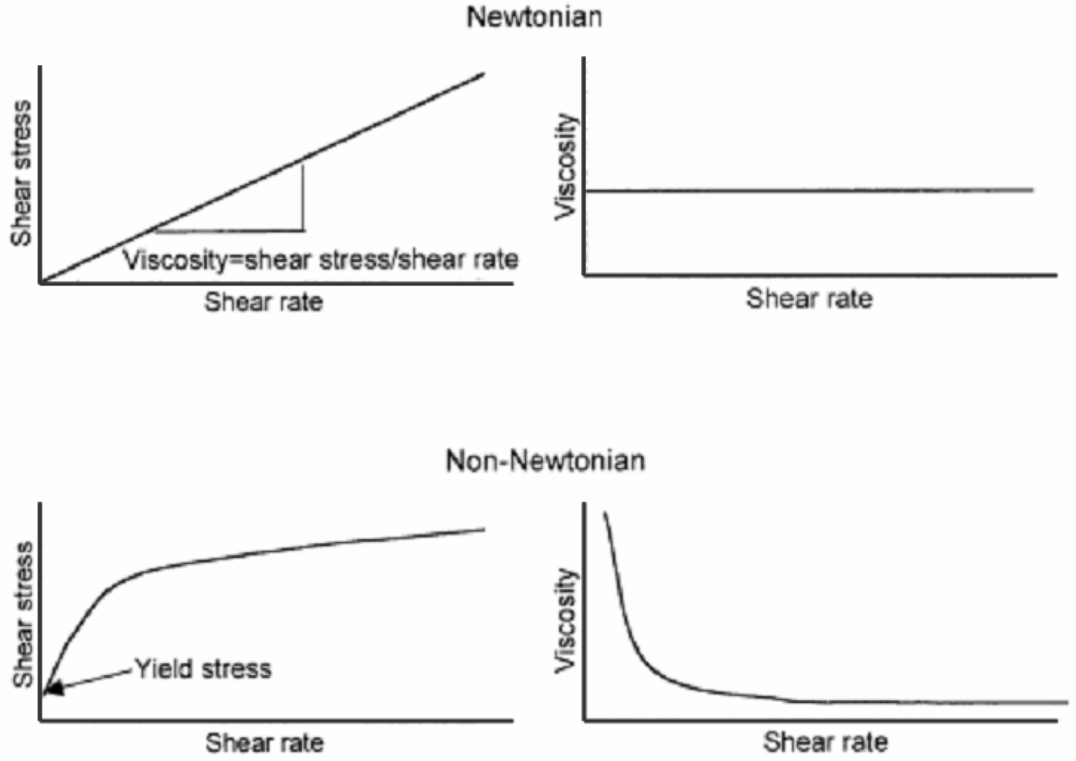

Figure 1-2: Shear stress – shear rate and viscosity – shear rate relations for Newtonian and non-Newtonian liquids

1. In Newtonian liquids, the viscosity is independent of variations in shear rate or shear stress. For these fluids the slope of the shear stress–shear rate relation is constant over the range of shear stress examined, and thus the viscosity is constant.
2. In non-Newtonian liquids, the apparent viscosity is not a constant but it depends on the magnitude of the shear stress or shear rate and can be calculated as the ratio of shear stress to shear rate. The viscosity of a non-Newtonian fluid may decrease (shear - thinning behavior) or increase (shear - thickening behavior) as the shear rate is increased. Non-Newtonian liquids may have a yield stress below which the shear rate is zero (no shear flow), resulting in an infinite value for apparent viscosity. The flow behavior of non-Newtonian liquids may also be time dependent; the viscosity of a thixotropic liquid decreases with time at a fixed shear rate. For both classes of fluids, the viscosity of a liquid depends on its temperature, and for most fluids viscosity decreases with increasing temperature.
Several units have been used for viscosity, with the most common being milliPascal*sec (mPa*sec), which is numerically equal to centipoise (cP); water at 20°C has a viscosity of 1.0 mPa*sec or 1.0 cP. The viscosity of a liquid can be

measured by a viscometer, which is a device built for studying stress - strain relations. Capillary viscometers are widely used devices for measuring viscosity of Newtonian liquids. The working principle of a capillary viscometer is based on the measurement of flow rate of the liquid through a well-defined capillary tube under a certain pressure difference; at constant temperature and pressure difference, the flow rate decreases with increasing viscosity. Capillary viscometers can also be used for flow measurements of non-Newtonian liquids, but estimation of viscosity is difficult because the shear rate varies across the diameter of the tube (i.e., maximum at the wall, zero at the center). Rotational viscometers of various types are thus more commonly used for studying non-Newtonian liquids. In a rotational viscometer, the liquid under investigation is sheared between two surfaces, either under constant shear stress or shear rate, and the response (resulting shear rate or shear stress, respectively) is measured. The geometric design of the shearing portion varies among instruments but is usually designed to provide a uniform shear rate or shear stress throughout the sample being studied.

1.4 HEMORHEOLOGY

Hemorheology deals with the flow and deformation behavior of blood and its formed elements (RBCs, WBCs, platelets). The rheological properties of blood are of basic science and clinical interest: the details of blood rheology are still being studied, and blood rheology can be altered in many disease states. There is an increasing amount of clinical and experimental data clearly indicating that the flow behavior of blood is a major determinant of proper tissue perfusion.
From a biological point of view, blood can be considered as a tissue comprising various types of cells (formed elements) and a liquid intercellular material (plasma). From a rheological point of view, blood can be thought of as a non-Newtonian two-phase liquid; it can also be considered as a solid - liquid suspension, with the cellular elements being the solid phase. However, blood can also be considered as a liquid-liquid emulsion based on the liquid-like behavior of RBCs under shear.

1.4.1 Blood Viscosity

The apparent viscosity of blood depends on the existing shear forces (i.e., blood behaves as a non-Newtonian fluid) and is determined by plasma viscosity, hematocrit, RBC deformability and RBC aggregation. Because blood is a non-Newtonian suspension, its fluidity cannot be described by a single value of viscosity. As shown in Figure 1-3, normal human blood exhibits shear-thinning behavior.

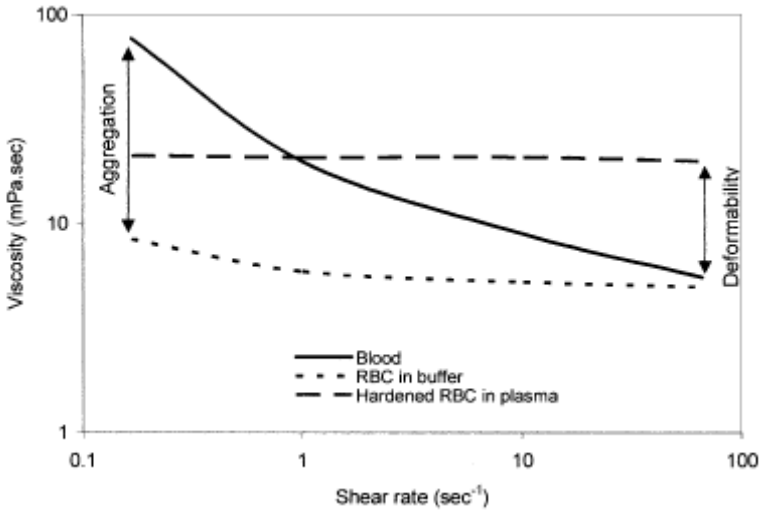

Figure 1-3: Shear rate-viscosity curves for normal blood, RBCs suspendend in protein-free buffer (a medium that doesn't induce RBC aggregation), and chemically rigified RBCs suspended in plasma

At low shear rates or shear stresses the apparent viscosity is high, whereas the apparent viscosity decreases with increasing shear rate and approaches a minimum value under high shear forces. At high shear rates above 100 to 200 sec^{-1} the viscosity of normal blood measured at 37ºC is about 4 to 5 cP and is relatively insensitive to further increases of shear rate. However, the viscosity becomes increasingly sensitive to shear rates below 100 sec^{-1} and increases exponentially as the shear rate is decreased. Thus, at lower shear rates, blood viscosity becomes extremely sensitive to the decrement in shear forces. At stasis, normal blood has a yield stress of about 2 to 4 mPa. RBCs are highly deformable, and this physical property significantly contributes to aiding blood flow both under bulk flow conditions and in the microcirculation. The tendency of RBCs to undergo reversible aggregation is an important determinant of apparent viscosity because the size of RBC aggregates is inversely proportional to the magnitude of shear forces; the aggregates are dispersed with increasing shear forces, then reform under low-flow or static conditions. RBC aggregation also affects the *in vivo* fluidity of blood, especially in the low-shear regions of the circulatory system.

Blood rheology has been reported to be altered in various physiopathological processes: (1) Alterations of hematocrit significantly contribute to hemorheological variations in diseases and in certain extreme physiological conditions; (2) RBC deformability is sensitive to local and general homeostasis, with RBC deformability affected by alterations of the properties and associations of membrane skeletal proteins, the ratio of RBC membrane surface area to cell volume, cell morphology, and cytoplasmic viscosity. Such alterations may result from genetic disorders or may be induced by such factors as abnormal local tissue metabolism, oxidative stress, and activated leukocytes; and (3) RBC aggregation is mainly determined by plasma protein composition and surface properties of RBCs, with increased plasma concentrations of acute phase reactants in inflammatory disorders a common cause of increased RBC aggregation. In addition, RBC aggregation tendency can be modified by alterations of RBC surface properties because of RBC *in vivo* aging, oxygen-free radicals, or proteolytic enzymes. Impairment of blood fluidity may significantly affect tissue perfusion and result in functional deteriorations, especially if disease processes also disturb vascular properties.

Plasma viscosity: Plasma is the suspending phase for the cellular elements in blood, and thus a change in its viscosity directly affects blood viscosity regardless of the hematocrit and the properties of the cellular elements. The normal range of plasma viscosity is between 1.10 and 1.35 cP at 37ºC, but higher values are seen in disease states or after tissue injury. Plasma is a Newtonian fluid. In general, the level of plasma viscosity is a good, nonspecific indicator of disease processes and is increased in pathophysiological conditions associated with acute phase reactions. This increase is closely related to the protein content of plasma. Acute phase reactants, such as fibrinogen, contribute significantly to the nonspecific increase of plasma viscosity in disease processes. Plasma viscosity can increase up to 5 to 6 cP in patients with abnormal protein levels such as seen in clinical states termed paraproteinemias.

Hematocrit value: Under laminar flow conditions, the presence of cellular elements disturbing the flow streamlines is the primary reason why blood viscosity is higher than plasma viscosity. The contribution of this disturbance to the magnitude of blood viscosity can be appreciated by calculating the relative viscosity of blood (i.e., blood viscosity divided by plasma viscosity). With increasing amounts of cells, flow lines are progressively disturbed, and relative viscosity increases above its value of 1.0 for plasma alone. The degree of disturbance of flow streamlines, and consequently the viscosity of blood, thus strongly depends on the concentration of the cellular elements. As shown in Figure 1-4, there is an exponential relationship between the hematocrit value and blood viscosity, such that at higher levels of hematocrit, blood viscosity becomes increasingly sensitive to hematocrit alterations. At medium to high shear rates, there is about a 4% increase of blood viscosity per unit increase of hematocrit (e.g., a change from 45 to 46% hematocrit increases blood viscosity by 4%).

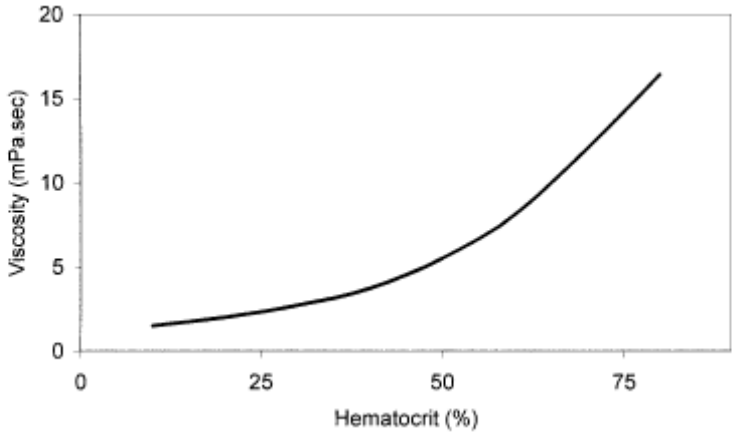

Figure 1-4: Effect of hematocrit on blood viscosity

In addition to the concentration of cellular elements in blood, their rheological properties are important determinants of blood fluidity. That is, the disturbance of flow streamlines depends not only on the concentration of blood cells but also on the behavior of these cells under shear forces. RBCs are the major determinant of this effect, with these cells exhibiting a very special rheological behavior. Normal RBCs are highly deformable bodies and tend to orient themselves with the flow streamlines,

especially if the shear forces are high enough to slightly deform these cells. In fact, it has been observed that RBCs behave like fluid drops under most flow conditions. Thus, RBC deformation and orientation are the primary cellular factors affecting blood viscosity at high shear rates.
Another important rheological feature of RBCs is their tendency to aggregate into linear arrays, termed rouleaux, in which they are arranged like stacks of coins. Linear aggregates then interact to form three-dimensional structures. Fibrinogen and other large plasma proteins promote RBC aggregation, which is dependent on the magnitude of shearing forces acting on the cells. Increased shear disrupts the aggregates, whereas reduced shear favors aggregation. Because of the increased effective particle size, the disturbance of flow streamlines becomes more pronounced when RBC aggregates are formed and blood viscosity is significantly increased. RBC aggregation is thus the major determinant of blood viscosity under low shear conditions. So, when studied in large geometry systems (i.e., large blood vessels, rotational viscometers with large spaces between measuring surfaces), the non-Newtonian behavior of blood is closely related to RBC deformability and RBC aggregation. RBC deformability and aggregation also affect blood flow in smaller blood vessels and in the microcirculation. Blood cellular elements other than RBCs (e.g., various WBCs, platelets) have no significant effect on the macroscopic flow properties of blood (i.e., blood viscosity measured in large geometry systems) but may contribute strongly to blood flow resistance and flow dynamics in the microcirculation where vessel diameters are 100 μm or less.

Red blood cell deformability: The normal human erythrocyte is shaped like a biconcave disc as long as it is not subjected to external stresses or constraints. However, when blood flows through a capillary, the flexible disc-like red cell is easily deformed. If the capillary diameter is slightly greater than the red cell diameter, deformation is produced by the action of the shear and pressure fields in the flowing plasma on the flexible nearly neutrally buoyant red cell. For a capillary diameter which is less than the cell diameter, the deformation of a static cell in a static fluid is simply caused by the constraining wall of the capillary while the deformation of a moving cell is, as before, produced by the resulting pressure and shear fields in the plasma. From these observations it appears that the “degree of deformation” of the red blood cell strongly depends on both the tube diameter and flow rate with minimum deformation occurring in large tubes at low or zero flow rates and maximum deformation occurring in small tubes at high flow rates. This unique characteristic of an erythrocyte transforming into a parachute-like shape in capillaries is expected for high fluidity in microcirculation and for high efficiency of oxygen diffusion to tissues by increasing the surface area in close contact with the endothelial cells. A fundamental process in the supply of oxygen to tissues is the unloading of oxygen from erythrocytes in capillaries; thus oxygen change in tissues relies on blood flow in microcirculation. Erythrocyte deformability is therefore an important index of blood flow and oxygen transport in microcirculation. The unique shape and structure of RBCs confer special mechanical properties to these cells. RBCs respond to applied forces by extensive changes of their shape, with the degree of deformation under a given force known as RBC deformability. The extent and geometry of these shape changes are functions of the magnitude and orientation of the applied forces, with RBC cellular properties acting as important determinants of the degree of deformation under a given stress. RBCs behave as elastic bodies, and thus the shape change is reversible when the deforming forces are removed. RBCs also

exhibit viscous behavior and thus respond as a viscoelastic body. Like shock absorbers on cars, the force needed to deform a RBC increases with both the extent and the rate of deformation. In addition, the RBC membrane can exhibit plastic changes under some pathological circumstances and can be permanently deformed by excessive shear forces.
The RBC membrane, including its underlying cytoskeleton, is the structured element that primarily determines the cell dynamic mechanical behavior. The lipid bilayer of the membrane is purely viscous and makes almost no contribution to the elastic behavior of the RBC membrane. Rather, it is now generally accepted that the RBC membrane cytoskeleton is mainly responsible for the maintenance of the biconcave-discoid shape. The RBC membrane cytoskeleton is a network of proteins lying just beneath the cell membrane, with the protein spectrin the most important component of this network. The spectrin network is attached to the membrane integral proteins such as band and glycophorins. Although the details of the network organization are not completely resolved, there is an increasing amount of data suggesting that the organization depends on maintaining RBC intracellular homeostasis. For example, membrane rigidity seems to depend on cytosolic calcium concentration, and thus the maintenance of normal mechanical behavior depends on a low cytosolic calcium level maintained by an active ATP-dependent calcium pump within the RBC membrane. In addition to membrane elastic and viscous properties as determinants of RBC deformability, two additional factors also contribute to this cellular property: (1) the cytoplasmic viscosity of RBCs, which in normal RBCs is solely determined by the hemoglobin concentration, and (2) the biconcave discoid geometry, which provides excess area for the contained volume and thus enables shape changes without increasing the surface area of the membrane. It is obvious from geometric principles that an increase of surface area is necessary in order to deform a sphere, yet the RBC membrane is extremely resistant to area increases.

Red blood cell aggregation: If RBCs are suspended in autologous plasma and observed at rest via light microscopy, they form large aggregates resembling a stack of coins (Figure 1-5). These aggregates, known as *rouleaux*, are easily dispersed by fluid forces (e.g., generating a local flow by applying a pressure on the coverslip), but form again as soon as the fluid forces are removed.

Figure 1-5: RBCs aggregates

However, such aggregation does not occur if RBCs are suspended in simple, isotonic salt solutions, and several studies have indicated that the extent and rate of RBC

aggregation strongly depend on the type and concentration of macromolecules in the suspending medium. In plasma, fibrous rather than globular proteins are responsible for aggregation, with fibrinogen concentration being the most important determinant of the aggregating property of plasma. Other macromolecules, such as high-molecular-weight dextrans or other water-soluble polymers, can also induce RBC aggregation.

1.5 MICROCIRCULATION

The microcirculation represents the smallest blood vessels in the body and it consists of the capillary network, the smallest vessels of 4-8 μm inner diameter (ID), the arterioles, vessels up to 100 μm ID in the arterial system and the venules, vessels somewhat larger in the venous system. The microcirculation is responsible for regulating blood flow in individual organs and for exchange between blood and tissue. Approximately 80% of the total pressure drop between the aorta and the vena cava occurs in these vessels. These features differentiate the microcirculation from the larger vessels of the macrocirculation, which serve as conduits to and from the heart and peripheral organs and as high and low pressure reservoirs essential to cardiac function. Another distinction is that microcirculatory vessels are embedded within an organ whereas most macrocirculatory vessels are not. This enables communication between the parenchymal tissue and these vessels. The deleterious consequences of diseases such as hypertension, sickle cell anemia, and diabetes exclusively, or to a great extent, afflict the microcirculation. Major blood loss due to injury or other causes, if not rapidly replenished, can lead to irreversible malfunctions in the microcirculation (circulatory shock) and death. Microcirculatory disorders are major contributors to morbidity and mortality and constitute a significant fraction of total health costs to society. Both basic and clinical research have focused on the means of preventing or ameliorating the damaging effects of these disorders on normal bodily function.

The history of experimental studies on microvessels goes back to the seventeenth century with the advent of the microscope. This led to Malpighi's discovery of the capillary system while van Leeuvenhoek described the complex branching network of microcirculatory vessels in the tail of an eel and measured the velocity of red cells in precapillary vessels to be on the order of 2 mm/s. To understand better the factors that determine flow in the blood vessels, in 1830 a French physician, Poiseuille, performed his now-classic experiments on the hydrodynamics of tube flow. The principles revealed in those studies form the basis of much of our current understanding of blood flow in the larger vessels and in the microcirculation. In the 1930s, a Swedish physiologist, Fåhræus, investigated the unique properties of blood flow in small glass tubes and set the foundation for subsequent research on microvascular flow and hemorheology. If blood is made to flow through a narrow vessel the volume concentration of the red cells within the vessel is lower than that of the outflowing blood. This so-called *Fåhræus effect* is one of the phenomena constituting the anomalous flow properties of blood. According to its first description by Fåhræus (1928) this effect is the consequence of the difference in traveling speed between red blood cells and their suspending fluid which in turn results from a nonuniform distribution of the flowing cells across the tube. Due to wall exclusion and additional axial migration (Taylor 1955; Bayliss 1959; Goldsmith and Mason 1961; Bugliarello et al. 1963) the red cells preponderantly occupy the central regions of the

velocity profile where higher local flow velocities are prevailing; on the other hand, a substantial volume fraction of the suspending fluid is confined to the slowly moving marginal regions of the flow. The higher velocity of the blood cells relative to the suspending fluid causes their volume concentration within the tube (dynamic tube hematocrit H_T) to be lower compared to the volume concentration of the cells in the blood entering and leaving the tube (discharge hematocrit H_D).
Quantitatively, this dynamic reduction of hematocrit is therefore dependent on two parameters: the radial distribution of red cells across the tube and the shape of the velocity profile. In addition, the apparent viscosity of blood measured in long tubes < 300 μm in diameter shows a precipitous decrease with decreasing diameter, reaching a minimum at diameters of 5-7 μm, corresponding to the diameter of capillary blood vessels. This trend is known as *the Fåhræus - Lindqvist effect*. The apparent or effective viscosity, μ_a, is defined as

$$\mu_a = \frac{\pi \, \Delta p \, D^4}{128 \, Q \, L} \qquad (1)$$

where Δp is the pressure drop, D is the tube inner diameter, L is its length, and Q is the volumetric flow rate. For a Newtonian fluid Equation 1 becomes the Poiseuille law. Fåhræus and Fåhræus - Lindqvist effects (Figure 1-6) are similar to those observed in other concentrated suspensions of deformable particles (Popel and Johnson, 2005).

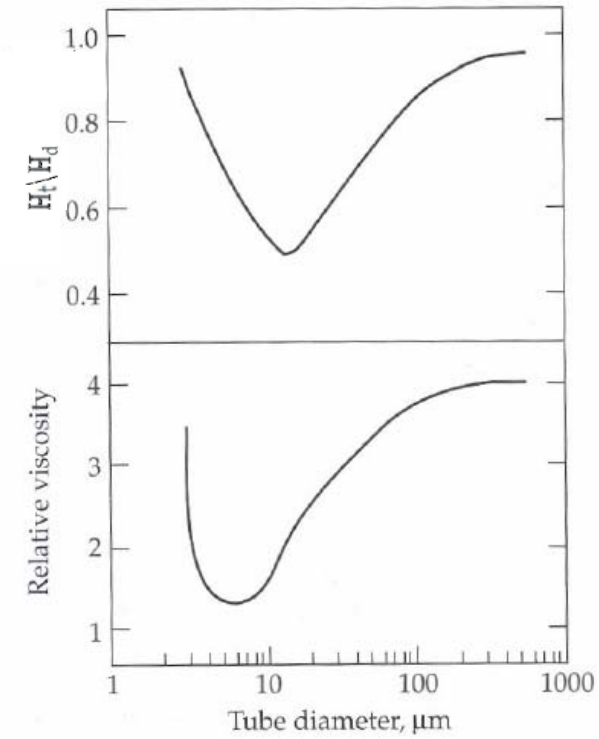

Figure 1-6: Fåhræus and Fåhræus - Lindqvist effects

Simple qualitative physical arguments show that these effects are interrelated. The experimentally observed migration of RBCs away from the wall and the formation of

a cell-depleted layer near the wall result in the mean RBC velocity being higher than the mean blood velocity.
A mass-balance analysis shows that the Fåhræus effect is a consequence of this phenomenon. Furthermore, because the viscosity of the cell-depleted layer is lower than the viscosity of the concentrated RBC core suspension, the apparent viscosity of blood is lower than the bulk viscosity of the uniform suspension as measured in tubes of large diameter or in rotational viscometers.
A number of studies (Thomas 1962; Gupta, Nigam & Jaffrin 1982) have modelled blood rheology in microvessels with a wide range of diameters to include the effects of cell-free or cell-depleted regions near the vessel walls. These studies usually involve one or more parameters which must be obtained empirically by fitting to experimental data. A more fundamental approach is to predict rheological properties starting from known mechanical properties of individual blood cells. This approach is particularly suitable for modelling flow in capillaries with diameters less than about 8 μm, in which red blood cells frequently travel in single file, each cell almost filling the lumen. Starting with the work of Barnard, Lopez & Hellums (1968) and Lighthill (1968), most theoretical studies of blood flow in narrow capillaries have rested on two key approximations. Firstly, the fact that individual cells almost fill the lumen has suggested the use of lubrication theory to describe the fluid flow in the narrow gap between the cells and vessel walls. In lubrication theory, the equations of fluid motion are simplified by the neglect of inertia and by the assumption that the thickness of the gap between the two surfaces is small compared with the other dimensions involved. Secondly, microscopic observations have shown that red blood cells in narrow capillaries may have approximately axisymmetric shapes, and the deformed cell geometry has been assumed to be axisymmetric. Some studies have been based on different assumptions. Zarda, Chien & Skalak (1977) also assumed axisymmetric geometry in analysing capillary flows at low velocities, but used a finite-element method which did not require the narrow-gap approximation of lubrication theory. Secomb and co-workers developed a more manageable model for tightly fitting cells based on the lubrication approximation, and formulated a boundary-value problem involving ordinary differential equations. More recently, Secomb and co-workers generalized the lubrication-flow model to account for the endothelial surface layer. In related efforts, Barthès-Biesel and coworkers studied the axisymmetric passage of capsules with spherical and spheroidal unstressed shapes through pores, tubes, and constrictions. Hsu and Secomb extended the lubrication-flow model to three dimensions, and studied the nonaxisymmetric motion of tightly fitting cells off the axis of a cylindrical capillary, accounting for the membrane tank-treading motion. Their results showed that the membrane tank-treading velocity is much smaller than the cell velocity, and the tank-treading motion acts to reduce the flow resistance, at most, by a few percent relative to that of a rigid cell with the same shape. These conclusions have provided support for the physical relevance and predictive ability of the axisymmetric flow model developed in the earlier studies. The finite-element formulation of Zarda et al (1977). and subsequent authors neglects cell interactions and describes the motion of the individual cells as though it occurred in isolation. On the other hand, the lubrication-flow model concentrates on the flow inside the small gap between the cell side surface and capillary wall, and assumes that the motion between adjacent cells is well approximated by the unperturbed parabolic Poiseuille flow. Moreover, in most studies, the lubrication flow model is indifferent to the undeformed cell shape, that is, if the flow is stopped, the cells will revert to the unstressed shape of a sphere. In the simulations of Secomb et al. (1986), the surface

area of this equivalent sphere is equal to the surface area of the actual red cell. This limitation was removed recently by Secomb and co-workers (2001).
Moreover, a large number of experimental techniques aimed at quantifying RBC deformability under various conditions has been developed to date, including ektacytometry, micropipette aspiration, filtration through a polycarbonate or nickel mesh filter, single pore filtration, dragging by optical tweezers, and passage through parallel arrays of capillary-like microchannels. Each of these methods allows for examination of the behaviour of RBCs in response to a single mode of deformation - folding or shear. In recent years, experiments using a flow channel device made out of silicon by semiconductor processing techniques have been reported. In particular, a new technique using microchannels as a capillary model to measure blood rheology has been described. Cokelet et al. (1993) developed a microvascular flow system with circular cross sections by etching glass plates with mirror images of the vascular pattern, Tracey et al. (1995) and Sutton et al. (1997) developed silicone-based capillary models and observed flowing cells. However, there have been few deformability measurements using a microchannel in which erythrocytes deform to a parachute shape in a similar manner to that seen *in vivo*. In 2000 Tsukada et al., in order to identify the difference in erythrocyte deformability between control and diabetic erythrocytes, measured erythrocyte deformability using transparent crystal microchannels and a high-speed video camera system. They observed axisymmetrically deformed erythrocytes flowing in microchannels (Figure 1-7) in a "parachute configuration". In order to estimate their deformability the deformation index DI = l/d, where d is the diameter of the erythrocyte in the parachute configuration and l is the erythrocyte length, was defined.

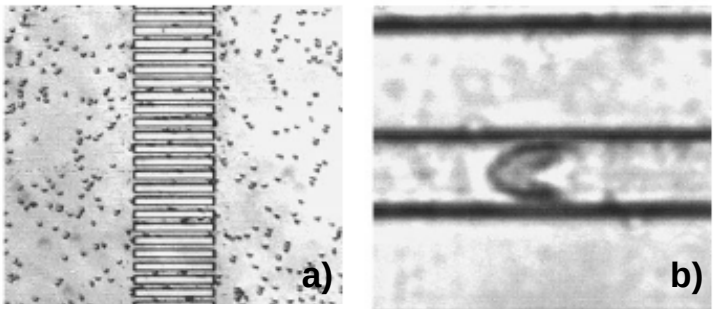

Figure 1-7: Low- (a) and high-(b) magnification images of erythrocytes flowing in glass microchannels recorded with a high-speed camera system (Tsukada et al, 2000)

Moreover, data of RBC velocity as a function of pressure drop in microcapillaries are scarce and limited in range (up to a few mm/sec). In fact, a simultaneous, systematic acquisition of shape and velocity of RBCs flowing in microcapillaries of comparable size, which is still lacking, would be at order to improve our understanding of the RBC flow behavior in the microcirculation.

1.6 MICROFLUIDICS

Microfluidics is the science and technology of systems that process or manipulate small (10^{-9} to 10^{-18} litres) amounts of fluids, using channels with dimensions of tens to hundreds of micrometres. The first applications of microfluidic technologies have been in chemical analysis, for which they offer a number of useful capabilities: the

ability to use very small quantities of samples and reagents, and to carry out separations and detections with high resolution and sensitivity, low cost, short times for analysis and small footprints for the analytical devices. In microfluidic channels the flow is completely laminar: all the fluid particles move in the same direction and at the same speed. Unlike turbulent flow, this allows the transport of molecules in the fluid to be very predictable. It offers fundamentally new capabilities in the control of concentrations of molecules in space and time.
The origins and the motivations of microfluidics could be found in four fields: molecular analysis, biodefence, molecular biology and microelectronics. The first motivation of microfluidics lie in microanalytical methods - gas-phase chromatography, high-pressure liquid chromatography and capillary electrophoresis, which, in capillary format, revolutionized chemical analysis. These methods (combined with the power of optical detection by laser techniques) made it possible to simultaneously achieve high sensitivity and high resolution using very small amounts of sample. The second motivation for the development of microfluidic systems came with the realization - after the end of the cold war - that chemical and biological weapons posed major military and terrorist threats. To counter these threats, the Defense Advanced Research Projects Agency (DARPA) of the US Department of Defense supported a series of programmes aimed at developing field-deployable microfluidic systems designed to serve as detectors for chemical and biological threats. The third motivational force came from the field of molecular biology: the explosion of genomics in the 1980s, followed by the advent of other areas of microanalysis related to molecular biology, such as high-throughput DNA sequencing, required analytical methods with much greater throughput, and higher sensitivity and resolution than had previously been contemplated in biology. The fourth contribution was from microelectronics. The original hope of microfluidics was that photolithography and associated technologies that had been so successful in silicon microelectronics, and in microelectromechanical systems (MEMS), would be directly applicable to microfluidics. Some of the earliest work in fluidic microsystems did, in fact, use silicon and glass, but these materials have largely been displaced by plastics. For analyses of biological samples in water, devices fabricated in glass and silicon are usually unnecessary or inappropriate. Silicon, in particular, is expensive, and opaque to visible and ultraviolet light, so it cannot be used with conventional optical methods of detection. It is easier to fabricate the components required for microanalytical systems - especially pumps and valves - in elastomers than in rigid materials. Neither glass nor silicon have all the properties (especially permeability to gases) required for work with living mammalian cells.

1.6.1 Lab on chip

One of the latest developments toward the realm of the small is the so-called "*lab on a chip*" (LOC) - a device about the size of a palm, able to perform a myriad of tasks associated with a standard laboratory. This idea has been around for a while, and certainly the idea of fitting a lot of equipment on a portable device is convenient, whereby the LOC is envisioned to be a simple tool, that is both easy to operate, and also offers a way to do things where very small amounts of sample are required. As well, such devices are disposable, which make them extremely useful for clinical procedures. For instance, it is possible to conceive a device that needs only a small sample of bodily fluid to diagnose a patient's illness. LOCs are also of great interest to safety and military departments, who would greatly benefit from having portable

chemical detection systems. Although the concept of scaling down a system seems simple, the operation of LOC devices is quite complicated. Different rules apply at small scales: viscous friction (or the resistance to flow) dominates the micro world. The media that a molecule such as a protein moves in, is in effect incredibly dense, because the atomic size of the fluid molecules is comparable in size to the protein itself. Every time a macroscopic object moves, it will displace millions of other molecules in the fluid: but for a microscopic entity dislodging similar sized molecules this movement can be especially challenging. Therefore, gravity and inertial effects no longer matter at this scale. Instead, a molecule has to primarily confront viscous forces and random Brownian motion. For these reasons, the design of a device intended to be very small and yet precise is not easy. From an engineering point of view, it is essential to keep in mind how differently the system is going to behave compared to the macro scale. One of the main players in the lab on a chip industry is the *microfluidics* platform. Microfluidic devices are generally made in glass or plastics but several laboratories utilize PDMS, a type of silicone.
PDMS is an optically transparent, soft elastomer. The ease with which new concepts can be tested in PDMS and its ability to support certain very useful components (such as pneumatic valves), have made it the key material for exploratory research and research engineering at the early stages of development. Moreover, the biocompatibility of PDMS suggests that it might ultimately be possible to embed microfluidic devices *in vivo* for certain types of biomedically relevant analysis. More advantages of PDMS are that it is very cheap, optically clear and permeable to several substances, including gases. Since air can quickly diffuse out, the latter aspect is very convenient, making it possible to inject fluid into a channel that has no outlet. PDMS is commonly used as a stamp resin in the procedure of soft lithography, making it one of the most common materials used for flow delivery in microfluidics chips.

1.6.2 Soft lithography

The patterning required in microfabrication is usually carried out with photolithography, but it shows some disadvantages: the sizes of the features it can produce are limited by optical diffraction, and the high-energy radiation needed for small features requires complex facilities and technologies; it'is expensive; it cannot be easily applied to nonplanar surfaces; it tolerates little variation in the materials that can be used and it provides almost no control over the chemistry of patterned surfaces, especially when complex organic functional groups of the sorts needed in chemistry, biochemistry, and biology are involved. So, there is a new alternative, non-photolithographic microfabrication method that would complement photolithography: this technique would ideally circumvent the diffraction limits of photolithography, provide access to three dimensional structures, tolerate a wide range of materials and surface chemistries, and be inexpensive, experimentally convenient, and accessible to molecular scientists. This technique is called *soft lithography*. It provides a convenient, effective, and low-cost method for the formation and manufacturing of micro- and nano-structures. In soft lithography, an elastomeric stamp with patterned relief structures on its surface is used to generate micropatterns and microstructures. With this type of technique it is possible to produce devices which can be used in the areas of optic telecommunications or biomedical research. For PDMS devices, soft lithography is based on the utilization of substances that become soluble to particular solvents when exposed to UV light. These substances

are called photoresists and they appear to be very dense transparent liquids. Upon baking their consistency becomes harder. This technique allows the production of countless features in the same time needed for one (essentially by shining the appropriate pattern of light). Unlike machining the time required does not scale with the increased number of elements.
Two of the key features of soft lithography are the use of elastomeric (that is, mechanically soft) materials to fabricate the pattern transfer elements by molding, and the development of techniques that pattern complex biochemicals. Both features involve organic materials and polymers - “soft matter,” in the language of physics.

1.6.3 Blood on a chip

Microfluidic devices have found numerous applications in biology, biochemistry, and medicine because of their ability to efficiently control and replicate microenvironments. They also offer practical benefits such as limiting human exposure to large amounts of biohazardous samples. Microfluidic systems are easy to fabricate, owing to recent advancements in rapid prototyping, and provide an ideal environment for testing either bulk samples or single entities, such as individual cells. Recognizing the need for devices that mimic the capillary microenvironment, many researchers have designed capillary-like channel systems in silicon and glass substrates. The ability to fabricate micrometer-sized features in glass and silicon makes these materials attractive options for making capillary-sized structures. Through these studies, it has been possible to record normal erythrocyte area, volume, and deformability. Many of these devices are integrated into comprehensive test platforms with controlled flow rate, temperature and pressure. This advance enabled researchers to develop systems that closely mimic the *in vivo* environment. Although providing a geometrically similar environment to capillaries, silicon and glass channels do not have the structural properties, such as elastic modulus, of capillary tissue. Recently, structural information of normal erythrocytes was determined by using a human erythrocyte microchannel analyzer made in PDMS (Gifford et al, 2003). So, a microfluidic device allows to evaluate the effect of RBC deformability on microvascular perfusion by directly measuring the flow of blood through a microchannel network with realistic dimensions and architecture similar to real microcirculation.
For clinical applications, bringing complete labs for blood analysis to the bedside through point-of-care analyzers capable of comprehensive diagnostic is poised to reshape the delivery of health care. New devices for convenient use at home or in doctors’ offices would allow for rapid and accurate diagnostic and prognostic, based on blood cells, of infectious diseases, cancers, and inflammatory responses. These may also allow better matching between drugs and patient pathophysiology, reducing side effects and improving efficiency of therapy. In drug discovery, microfluidic devices may redefine the entrance criteria for clinical trials and test for these criteria in a time- and cost-effective way. Moreover, in small-animal studies, microfabricated devices would only use minute amounts of blood for analysis, allowing for repetitive sampling at multiple time points and minimizing the adverse effects of blood drawing. On the whole, on-chip blood sample preparation would lead to more gentle, fast, and consistent manipulation of the living cells, and therefore more accurate and better quality of extracted information.

1.7 BLOOD ANALOGS

In spite of the development of cardio-vascular prosthetic devices, prosthetic heart valves, pulsatile blood pumps, models of the circulatory system, and sophisticated studies of flow through the complex geometries of the circulation, an analog test fluid with the rheological properties of blood is still lacking. The properties of blood pose several problems for quantitave applications as a test fluid: composition differs from donor to donor, precluding a fixed standard; properties change with time because of metabolic processes; opacity restricts optical studies of flow; blood samples can carry disease, thus presenting a biological hazard to workers; blood is a two phase, unstable system subject to sedimentation, and it can clot, thus blocking its fluid-like flow; the volume which can be withdrawn from a single donor is limited, restricting high volume applications. Consequently, it would be highly desirable to use have blood analogs free of such complications. In addition, the stress-strain-shear rate relation for blood varies with the timing, rate, and duration of flow because blood is a viscoelastic, non-Newtonian, thixotropic, and dilatants fluid.

The classical analog, a mixture of glycerine and water, which at 45% glycerine gives a Newtonian viscosity of 3.97 mPa·s at 25°C about twice the viscosity of blood plasma, but in the neighborhood of that of normal blood at high steady shear rates. It is low cost and transparent, but exhibits none of the viscoelastic flow properties of human blood, so it lacks elasticity and provides only viscous and inertial effects.

Since the discovery of the viscoelasticity of blood, much effort has been devoted to finding a suitable analog that possesses this property. Ideally, a suspension of spherical particles with oblate shape, having elastic properties similar to red blood cells and some aggregation tendency would be a good candidate. In this direction, 1 mm diameter polystyrene spheres suspended in water with addition of Dextran 70 and calcium chloride to induce aggregation produced some limited range of viscoelastic properties. Suspensions of biconcave, disc-shaped particles in Dextran 70 also have be used to produce a viscoelastic analog (Fukada, 1989). Shear rate dependent viscoelastic character very similar to blood has been found using solutions of water soluble polymers. These are usable for modeling blood flow in uniform channels with cross sections large compared to the size of blood cells.

1.8 THE RHEOLOGY OF DROPLET-BASED BIPHASIC SYSTEMS

The flow of deformable droplets of one Newtonian fluid suspended in another Newtonian fluid shows non-Newtonian features, similar to flow behavior of blood in capillaries. Hence, a system constituted by a suspension of liquid drops could be considered in developing model of blood flow.

The easiest situation to study is a single deformable drop in shear flow between two infinite parallel planes. From the pioneering work of Taylor in the 1930s, most of the literature on flow-induced drop deformation is devoted to the unbounded flow situation. The classical fluidodynamic problem is given by an isolated drop in a simple shear flow field, where the only intrinsic length scale is the undeformed drop radius R_0. When the drop is sufficiently small with respect to any typical dimension L of its ambient of motion, i.e., when $R_0 << L$, the “outer” dynamics is dictated by the undisturbed flow. In this simplest case, one assumes that the drop is suspended in an unbounded fluid, and the undisturbed velocity field “at infinity” is linear. Another usual assumption is that the Reynolds number of the fluid motion governing the deforming drop is low (Eq. 2)

$$Re = \frac{\rho v R_0}{\eta} << 1 \qquad (2)$$

with ρ and η the density and viscosity of the external fluid, respectively.
To keep the situation as simple as possible, external and buoyancy forces are assumed negligible, the two fluids are taken to be incompressible and mutually immiscible, and isothermal conditions hold. In such a case, the two nondimensional parameters governing drop shape and stability are the ratio of shear and interfacial stresses, expressed by the capillary number (Eq. 3) where η_c is the continuous phase viscosity, $\dot{\gamma}$ is the shear rate, σ is the interfacial tension, and the viscosity ratio λ (Eq. 4) is the ratio between drop and continuous phase viscosity.

$$Ca = \frac{\eta_c R_0 \dot{\gamma}}{\sigma} \qquad (3)$$

$$\lambda = \frac{\eta_d}{\eta_c} \qquad (4)$$

Typical stationary drop images at low to moderate drop deformations are shown in Figure 1-8a for the lateral view (along the vorticity axis), and in Figure 1-8b for the top view (along the velocity gradient). In the images, the most significant (and readily observable) geometric parameters are also shown, namely: i) (Figure 1-8a) the maximum and minimum distances R_{MAX} and R_{MIN} of the contour from the drop centre, and the angle ϕ between R_{MAX} and the shear direction x in the lateral view; ii) (Figure 1-8b) the maximum and minimum distances R_P and R_Z of the contour from the drop centre in the top view. In both views, the drop contour is very well approximated by an ellipse.

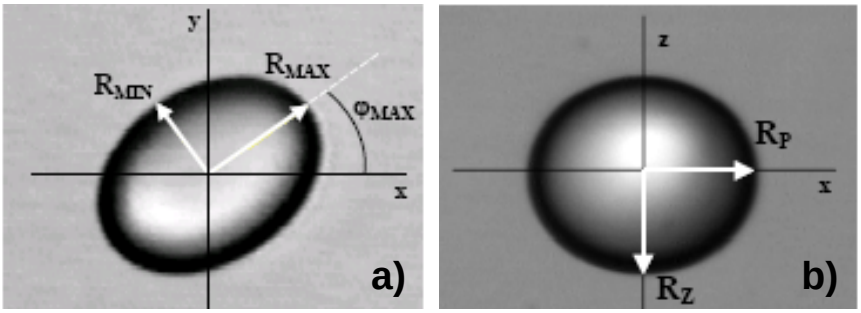

Figure 1-8: Side view (a) and top view (b) images of a drop during shear

A parameter that describes drop deformation is the so-called deformation parameter D (Eq. 5), originally introduced by Taylor.

$$D = \frac{R_{MAX} - R_{MIN}}{R_{MAX} + R_{MIN}} \qquad (5)$$

Hence, the three axes $R_{MAX,}$ R_{MIN} and R_Z, and the angle ϕ provide a meaningful representation of drop shape.
To better understand the transport of cells or other biological media in capillaries and microfluidic devices, droplet motion in confined geometries is more relevant. The deformation of a droplet in a continuous immiscible liquid phase under microconfined flow is a subject of growing interest in several applications. The current understanding of the effects of confinement on drop deformation, even in well-controlled flow fields, is rather limited, and the design issues concerning drop rheological behavior in microdevices are often addressed on an empirical basis. Wall effects on drops deformation are therefore of practical interest, and, as in the case of unconfined flows, the starting point has been the investigation of Newtonian systems. In 2006 Sibillo et al. have studied the evolution of a single sheared drop immersed in an equiviscous fluid as a function of the capillary number Ca and of the degree of confinement a/h (where a is the drop radius and h the gap between the plates). In 2007, Vananroye et al. have explored the steady state behavior of a single Newtonian drop in a confined Newtonian shear flow for several viscosity ratios and degrees of confinement and found that wall effects enhance drop deformation at any viscosity ratio. The problem of the confined drop has been investigated also numerically (Janssen and Anderson 2007) substantially confirming the experimental observations. From a theoretical point of view, the first papers on the deformation of a single drop under confined flows traced back to the work of Shapira and Haber (1988), where both the full hydrodynamics and drop deformation have been derived in the limit of low Reynolds numbers for a single drop moving between parallel plates. The authors used the Lorentz's reflection method (Happel and Brenner 1983), and thus, only steady states were predicted. Successively, the same authors (Shapira and Haber 1990) derived the hydrodynamics and drop deformation in the limit of low Reynolds numbers for a single drop in a confined shear flow. They predicted that the confinement enhances the steady deformation at any viscosity ratio, as later on experimentally confirmed by Sibillo et al. (2006) and by Vananroye et al. (2007).
While attention has been mostly paid to the study of "Newtonian systems", i.e., systems made of a Newtonian drop immersed in a Newtonian matrix (Rallison 1984; Stone 1994; Guido and Greco 2004), in recent years, the case of a single non-Newtonian drop immersed in a non-Newtonian matrix subjected to a generic flow field has been addressed. Greco (2002) developed a theory for small drop deformation, while, for instance, Minale and Maffettone (2004) developed a phenomenological model. Several experimental investigations have also been run (e.g. Guido et al. 2003; Verhulst et al. 2007). The interest for this system is driven by the observation that in real processing conditions, very often non-Newtonian fluids are encountered. However, during processing the drops in a polymer blend often flow through channels or in the vicinity of the devices walls. The combined effect of flow confinement and non-Newtonian character of the components fluids of a polymer blend has not been tackled so far.
In the field of biomechanics, the problem that has received considerable attention is the motion of deformable drops through cylindrical tubes. Liquid drops are crude models of red blood cells whose motion is of paramount significance on the physiology of blood flow in the microcapillaries. Although the interface of a red blood cell is considerably more complex than that between two immiscible fluids, the common feature of deformability gives partial reason to extracting information on the former by studying the latter. The dimensionless parameters that govern the motion of a single drop in a cylindrical tube are the Capillary number Ca (Eq. 6), where η_C is

the viscosity of the suspending fluid, V is the average velocity of the two-phase flow and σ is the interfacial tension between the drop fluid and the suspending fluid; the ratio of the viscosity of the drop fluid to the viscosity of the suspending fluid is λ (Eq. 7), and K (Eq. 8) is the ratio between the undeformed radius of the drop and the radius of the tube.

$$Ca = \frac{\eta_c V}{\sigma} \tag{6}$$

$$\lambda = \frac{\eta_d}{\eta_c} \tag{7}$$

$$k = \frac{a}{R} \tag{8}$$

In 1972 Hyman and Skalak have analyzed the axisymmetric flow of a suspension of deformable liquid drops through a rigid cylindrical tube. The liquid in each drop and the suspending fluid have been both assumed to be Newtonian and incompressible, and a surface tension was assumed to act at the interface. The motion was assumed to be sufficiently slow so that inertial terms in the equation of motion may be neglected. Olbricht and Kung (1992) have experimentally studied the motion of drops in straight tubes for an extensive range of parameters. The axisymmetric motion of deformable drops in pressure-driven flow has been considered by Martinez and Udell (1990). The deformation of axisymmetric drops and bubbles moving through straight tubes and constrictions under pressure-driven flow have been studied by Tsai and Miksis (1994) as a function of the capillary number. Using a combination of lubrication theory for the thin film between the drop and the tube wall and a two dimensional boundary-integral representation for the internal flow, Hodges et al. (2004) recently considered the motion of a semi-infinite drop moving through a cylindrical tube. Coulliette and Pozrikidis (1998) considered the transient motion of a periodic file of three-dimensional drops in a cylindrical tube (Figure 1-9) by numerical simulation for subcritical capillary numbers.

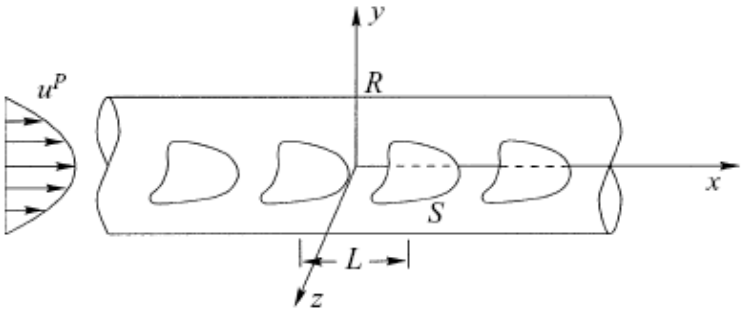

Figure 1-9: Schematic illustration of pressure-driven flow of a file of deformable drops through a circular tube

In their study, the drop-to-medium viscosity and density ratios were fixed at unity and the surface tension was assumed constant. The principal objective of the analysis was to extend previous two-dimensional and axisymmetric studies of drop motion by examining the dynamics of droplet migration, when the droplets are initially placed off the tube centerline. Assuming that the capillary number is sufficiently large, the droplets begin to deform from their initially spherical shape, migrate towards the centerline of flow, and then approach a steady shape after a preliminary stage of rapid deformation. When the capillary number is sufficiently low, a quasi-steady state is established where changes in the drop shape are caused predominantly by the radial migration. The quasi-steady shapes are significantly affected by the the off centre distance from the centreline and the drop separation. Moreover, there is a general similarity between the drop shapes formed by the periodic file shown in Figure 1-9 and those of the red blood cells flowing in microcapillaries. It should be pointed out, however, that the drops develop a slipper-like shape only when the capillary number is high enough, whereas the red blood cells appear to do so always, as long as the tube radius is sufficiently small. In the work of Sibillo et al. (2006) the drop deformation in microconfined shear flow was studied. The following will focus mainly on this work because it was carried on in the same laboratories as where all the experiments for this phD thesis were performed. Moreover, it was the starting point on which chapther 4, about the drop flow in microcapillaries, is based. In the work of Sibillo et al. all the experiments were carried out at λ=1 and along the vorticity axis. The experiments are started with an initial setting of the gap *h* between the confining plates high enough that no significant wall effects are anticipated. Several shear flow runs are then carried out at increasing values of shear rate (from one run to the other, the drop is allowed to retract back to the spherical shape at rest). This shear rate sweep is iterated at progressively lower gap settings by reducing the distance between the parallel plates (while maintaining the drop in the center of the gap) through a micrometric translating stage. The nondimensional gaps *a/h* investigated (whit drop radius *a* ranging from 50 to 200 μm) in this work range from 0.07 to 1 (the latter corresponds to the case of drop diameter twice the gap size). Images from two representative runs at Ca=0.4 and nondimensional gap *a/h* =0.07 and 0.5 are shown in Figure 1-10, where images taken at different times are presented for each run.

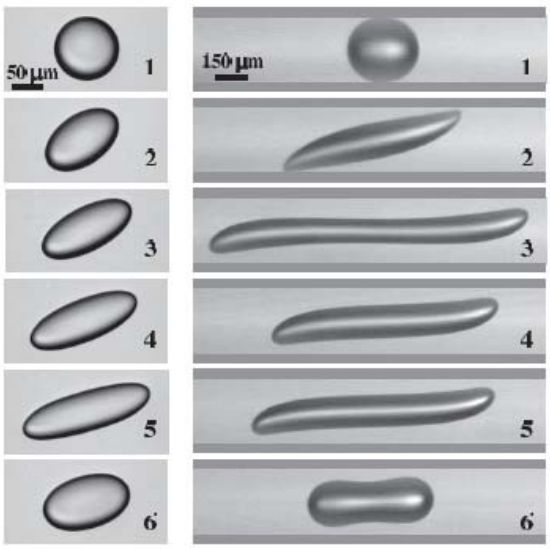

Figure 1-10: Transient drop deformation at Ca= 0.4 and a/h = 0.07 (left sequence) and 0.5 (right sequence) as observed along the vorticity direction in a parallel flow apparatus. The viscosity ratio λ is equal to unity within experimental error

The left sequence, which is referred to *a/h*=0.07 (*h*=940 μm), shows the typical shapes that are observed in the absence of wall effects. Starting from the spherical configuration at rest (1), the drop becomes more deformed and oriented in the flow direction (2)–(4) until a steady state shape is reached (5). Upon cessation of flow, drop deformation is relaxed (6) towards the equilibrium spherical shape. A striking difference in shape is found in the right image sequence, which corresponds to *a/h*=0.5 (*h*=345 μm; the walls have been highlighted in the images for the sake of clarity). In this case, starting again from the spherical configuration (1), the steady state shape (5) is not attained monotonically, but drop deformation and orientation go through maxima (3) and minima (4) in a damped oscillatory fashion. Furthermore, at *a/h*=0.5 the deformed drop is not ellipsoidal, as in the ‘‘unconfined’’ flow case (*a/h*=0.07), but exhibits sigmoidal shapes, with pointed ends in the startup transient (2). As before, once the flow is stopped, drop relaxation towards the spherical configuration is observed, though with different retraction shapes (6). A quantitative representation of this trend is displayed in Figure 1-11, where the nondimensional drop axis $R_{MAX}/2a$ is plotted as a function of the nondimensional time t^* (given by the actual time multiplied by the shear rate). For the sake of comparison, $R_{MAX}/2a$ versus time at *a/h*=0.07 is shown in the inset in Figure 1-11. It can be noticed that the stationary value of $R_{MAX}/2a$ is almost 1.7 times higher when *a/h*=0.5 as compared to the unconfined case. In other words, the higher the confinement, the more extended is the drop shape at steady state. Furthermore, apart from the complex transient behavior, which is missing for *a/h*=0.07, the two cases differ in the time scale required to reach steady state conditions, which is an order of magnitude higher at *a/h*=0.5. We found indeed that, at a given value of *a/h*, the startup transients became slower and slower with increasing Ca until it was not possible anymore to reach steady state within the total travel allowed by the apparatus.

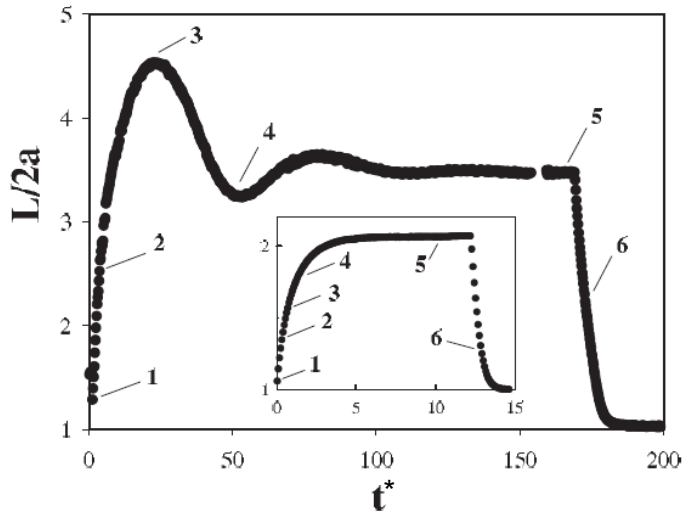

Figure 1-11: Quantitative representation of the transient drop deformation at Ca= 0.4 and a/h = 0.07 and 0.5 (inset)

In the small to moderate deformation regime, analytical expressions of drop deformation in confined shear flow have been derived by Shapira and Haber based on Lorentz's reflection method. The resulting first-order corrections for wall effects show that drop shape, as calculated by Taylor, is not altered with respect to unbounded shear flow, only the magnitude of deformation is increased. A comparison of these predictions for two-wall effects with experimental data, which is not available at present in the literature, is presented in Figure 1-12, where the deformation parameter is plotted as a function of *a/h* for Ca=0.1, 0.2 and 0.3. As shown before, at each value of Ca, drop deformation increases with *a/h*, i.e., by reducing the gap between the plates.

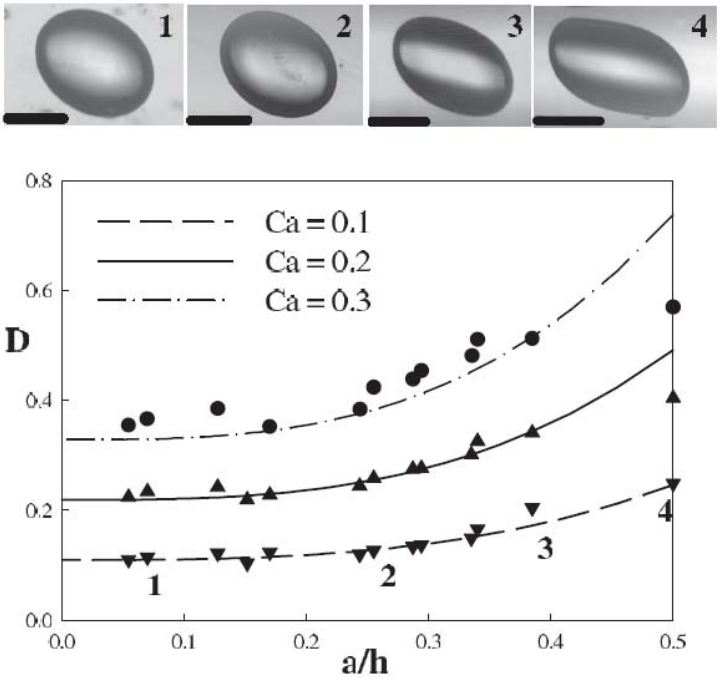

Figure 1-12: Comparison between experimental data and the predictions of Shapira and Haber at Ca= 0.1, 0.2 and 0.3

The corresponding stationary drop shapes for Ca=0.1 are shown in the upper panel in Figure 1-12, and it is interesting that even at the higher values of a/h, where distortions from the quasi-ellipsoidal shape are clearly visible, the agreement with theory is still quite satisfactory. This behavior is in line with the finding that Taylor predictions for D are in good agreement with experimental data up to drop deformations well beyond the range of validity of the small deformation theory, even though the observed drop shape is quite different from the predicted one. The Shapira and Haber predictions are still in good agreement with data at values of Ca=0.2 and 0.3, except when the drop gets too close to the wall (see the last point at a/h=0.5), where the reflection analysis is expected to fail. As a consequence of the increased drop deformation at reduced gap size, highly elongated shapes, which would be unstable in the unbounded case, are observed at steady state in confined shear flow. Furthermore, the deformed drop is more oriented along the flow direction in the latter case. These trends are emphasized when drop diameter is greater than gap size (i.e., when a/h > 0.5). The stabilization of elongated drop shape can be explained in terms of wall-induced distortion of the shear flow field. Small wall separations, indeed, increase the amount of rigid-body rotation in the flow with respect to simple shear and thus result in nearly closed flow streamlines. Boundary-integral simulations demonstrates that this confines the droplet to rotating within the closed streamlines, in contrast to the no-wall case, in which shear flow streamlines are open and droplet deformation can be unbounded thus leading to breakup. The major consequence of this phenomenon is that higher droplet deformations are stable and breakup is hampered. Another remarkable aspect of confined drop deformation is related to the critical behavior at breakup. In this work it was found that both the critical capillary number and the breakup time are somehow increased with respect to the unbounded case. An example is shown in Figure 1-13, where selected images illustrating drop shape evolution with time are presented at Ca=0.46 for *a/h*=0.35 (top sequence) and Ca=0.5 and *a/h*=0.5 (bottom sequence). In the slightly supercritical conditions at Ca=0.46 of the top sequence in Figure 1-13, the breakup dynamics is characterized by drop elongation followed by pinch-off at the ends of the neck region (at $R_{MAX}/2a=6$). The fragments generated upon breakup are three main daughter drops and two minor satellites in between them (image 5). An interesting feature of this breakup mode is that the central daughter drop is just slightly different (5% in radius) than the two daughter drops at the ends. Such behavior is at variance with the unbounded case, where the central fragments are smaller than the two main daughter drops at the ends. This suggests that confined shear flow could be exploited to generate quasi monodisperse emulsions by controlled breakup under near critical conditions. It can be noticed that the capillary number in the top sequence in Figure 1-13 is slightly higher than the critical value for breakup in unbounded shear flow at λ=1, which is ca. 0.43.

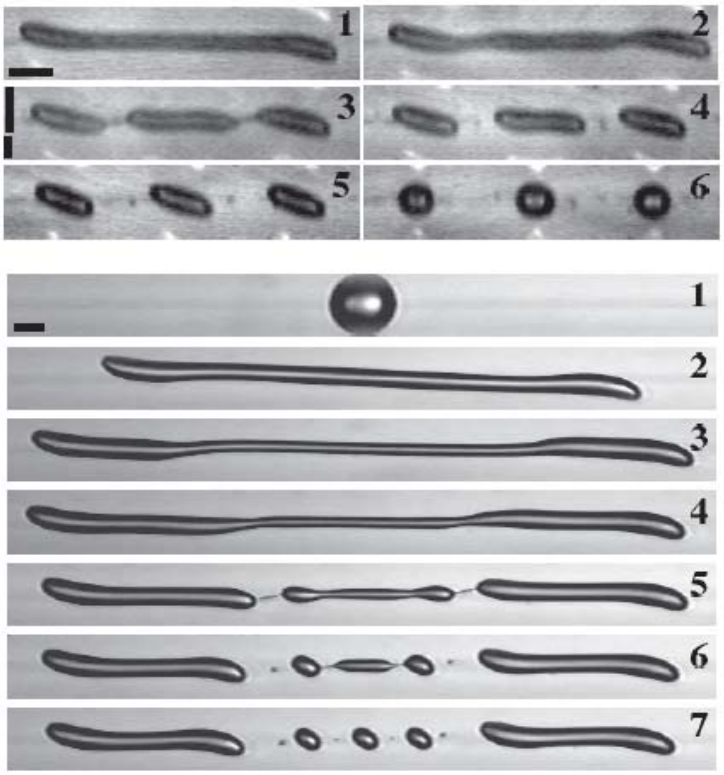

Figure 1-13: Drop breakup dynamics at Ca= 0:46 and a/h= 0.7 (top sequence, scale bar=100 μm) and Ca=0.5 and a/h=1 (bottom sequence, scale bar=150 μm)

The nondimensional breakup time, however, is more than twice the corresponding value for unbounded flow, thus confirming the slowing down of drop deformation kinetics induced by microconfined flow. Furthermore, the nondimensional drop axis at breakup is also higher than the corresponding value in unbounded shear.

The effect of confinement becomes more pronounced when drop diameter approaches gap size. At *a/h=0.*5, the deformed drop tends to a stable stationary shape, following a transient with damped oscillations, still at Ca=0.48, which would correspond to a supercritical condition (i.e., leading to breakup) in unbounded shear. At Ca=0.5, as in the bottom sequence of Figure 1-13, no oscillations are observed since the drop keeps elongating up to a point where pinch off takes place (at $R_{MAX}/2a=10$). The conical neck left behind retracts forming a bulbous part, where a further breakup event takes place. This is a common behavior in free-surface flows, such as jet breakup. The breakup time, which is ca. 65, is more than 3 times higher compared to the value for unbounded flow at the same value of Ca [ca. 20]. Overall, nine fragments are generated upon breakup, including two larger daughter drops, three main, and four smaller satellites (image 5). It so appears that, at a given Ca, breakup occurs at a higher elongation and at longer times in the confined case due to the stabilizing effect of the walls, thus generating more fragments compared to unbounded flow.

In conclusion, deformation and breakup of an isolated drop undergoing two-phase confined shear flow in a precision sliding plate apparatus at a $\lambda=1$ were described. Wall effects act to stabilize elongated drop shapes, which would be otherwise unstable in the unbounded case, by confining the drop to rotate within closed streamlines.

1.9 AIM OF THE THESIS

The goal of this work is to investigate blood flow in confined geometries as relevant to the development of a blood analog fluid having blood-like rheological properties. Such blood analog fluid would be a valuable testing toolto assess the performance of artificial devices, such as heart-assist devices, blood oxygenators, dialysis machines and peripheral access systems, which are currently tested, in most cases, by using water-glycerol solutions, a Newtonian fluid quite different from human bloodIn order to reach this objective, a better understanding of how the microstructural characteristics of blood and its flow properties make it such an effective means for delivery and exchange in the microcirculation is needed.
More in detail, the aims of this work can be summarized as follow:

- ⇒ setup of an experimental methodology to analyse the velocity and the deformability of red blood cells in microcapillaries and microchannels
- ⇒ confined Poiseuile flow of a model fluid to mimick the rheological behavior of blood

In the first part of the work a novel technique to measure velocity and deformability af RBCs in confined flow geometries *in vitro* will be presented. The experiments will be carried out on RBCs suspensions flowing in silica cylindrical tubes placed in a flow cell and having diameters close to the average cell size. Moreover, a silicon-made microfluidic device to study whole blood behavior during the flow in a microchannel network with dimensions and topology similar to the real microcirculation will be setup. Both the techniques wil be based on direct visualization of flowing RBCs by video-enhanced microscopy and automated image analysis procedures to measure cell velocity and deformation.
In the second part of this thesis the behavior of a model system will be studied by using both parallel plates and silica tubing. In this case too, video-enhanced microscopy and automated image analysis procedures will be used.

Chapter 2 RED BLOOD CELLS FLOWING IN MICROCAPILLARIES

2.1 MATERIALS AND METHODS

2.1.1 Blood samples

Fresh heparinized venous blood was obtained from healthy consenting volunteers. All blood samples were used within 4h of collection. Approximately 1 mL of whole blood was diluted with 100 mL of anticoagulant ACD, (0.6% citric acid, 1.1% dextrose anhydrous, 2.3% sodium citrate, 96% water) and 5 mL of human albumin. ACD (Acid Citrate Dextrose Solution, sometimes called Anticoagulant Citrate Dextrose Solution) is a solution of citric acid, sodium citrate and dextrose in water; it is mainly used as an anticoagulant to preserve blood, and during procedures such as plasmapheresis instead of heparin.
Albumin is the most abundant blood plasma protein and is produced in the liver. It normally constitutes about 70% of human plasma proteins; all other proteins present in blood plasma are referred to collectively as globulins. Albumin is important in regulating blood volume by maintaining the osmotic pressure of the blood compartment. It also serves as carrier for molecules of low water solubility, including lipid soluble hormones, bile salts, bilirubin, free fatty acids (apoprotein), calcium, iron (transferrin), and some drugs. Competition between drugs for albumin binding sites may cause drug interaction by increasing the free fraction of one of the drugs, thereby affecting potency.
The 1:100 level of dilution ensured optimal performance of the flow cell. The viscosity of the suspending fluid as a function of temperature was measured by a Ubbelohde glass viscometer. The presence of RBCs at the dilution used in the experiments did not change significantly the value of fluid viscosity. Furthermore, RBC viability was checked before each experiment by observing cell morphology under static conditions at high magnification (100x objective) (Figure 2-1).

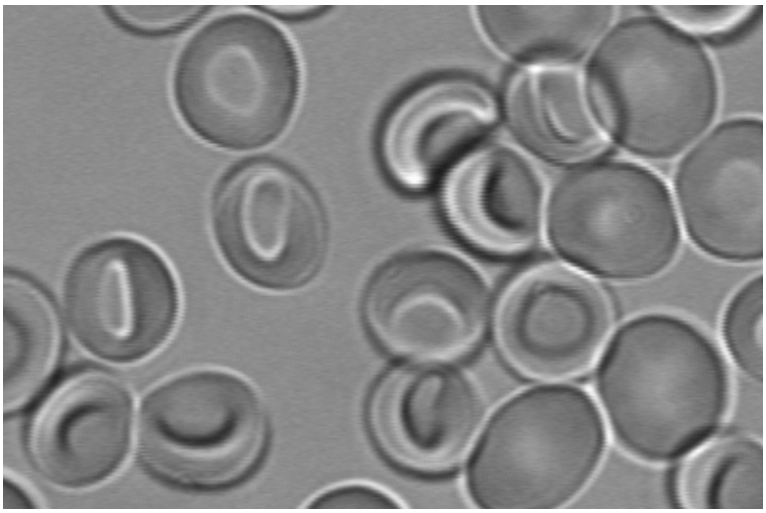

Figura 2-1: Red blood cells at rest

2.1.2 Flow cell

The flow cell (a schematic is shown in Figure 2-2) was made of two Plexiglass plates separated by a rubber spacer. A window was cut in the bottom plate to allow insertion of a coverslip slide for observations at high magnifications with oil immersion objectives.

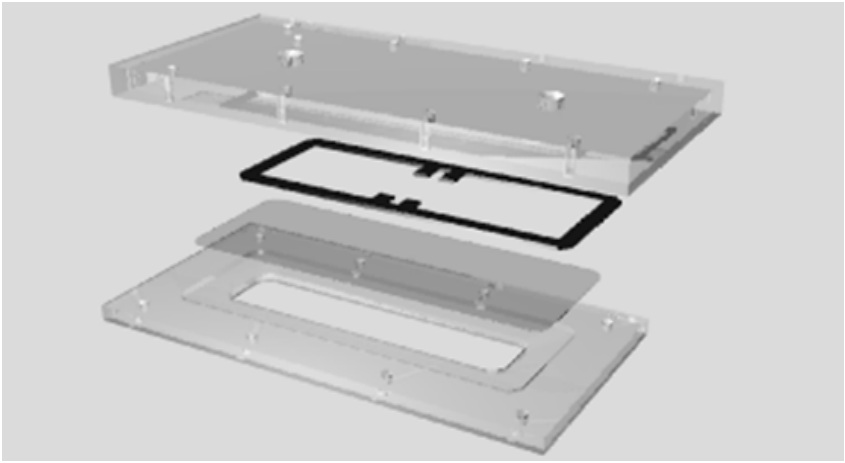

Figura 2-2: Component of the flow cell

The microcapillaries used in this work were made of silica (with 4.7, 6.6 and 10 μm ID, Polymicro Technologies). They were cut to about 3-4 mm and then placed in parallel on the flow cell coverslip (Figure 2-3). The diameter and length of all the capillaries used in this work were carefully measured by video microscopy.

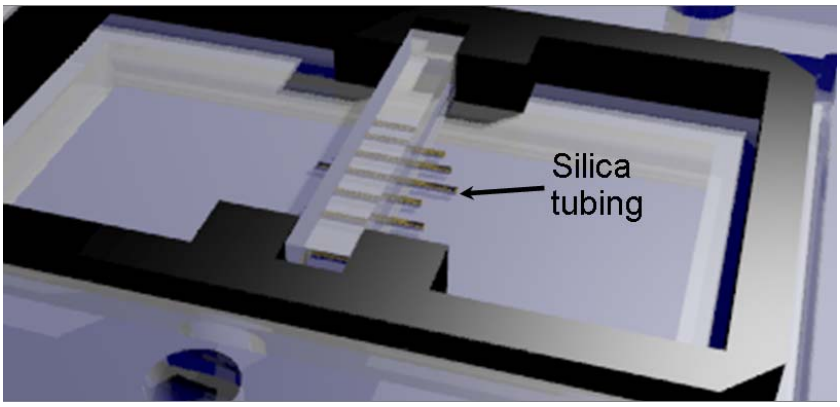

Figura 2-3: Detail of the flow cell: silica tubing

The measurements were carried out by filling the capillaries with an isorefractive silicone fluid to avoid optical distortions. A thin stripe of PDMS (polydimethylsiloxane, Sylgard 184, Dow Corning) has been put on the tubes to avoid optic distorsion caused by curvature of tube walls. PDMS was used because it has almost the same refraction index of silica.
The RBC suspension was fed to the flow cell through an input hole by a flexible tubing connected to a glass reservoir. The suspension coming out from the flow cell through an output hole was collected by a plastic tubing in another glass reservoir placed on a vertical translating stage. The pressure drop across the microcapillaries was regulated by adjusting the relative liquid levels in the entrance and the exit

reservoirs. At the beginning of each experiment the pressure was set to 150 cmH_2O for about 5 minutes to fill the tubes with the sample more quickly.

2.1.3 Experimental apparatus

The flow cell was placed on the motorized x-y stage of an inverted microscope (Zeiss Axiovert 100) (Figure 2-4) equipped with a motor assembly for focus control. Sample positioning was controlled by a custom LabView routine. Images of the flowing RBCs were acquired either by a high speed (Phantom 4.3, operated up to 1,000 frames/s) or a high resolution video camera (CD8488, Hamamatsu). When blood flow is recorded on videotape under physiological conditions, it is difficult to observe an individual erythrocyte in each frame with a standard video system, which operates at a rate of 25 frames/s. On the other hand, the high-speed video system, acquiring 1000 frames/s, can record clear images of individual erythrocytes. The high resolution video camera instead was used to get high quality snapshots of RBC shape by using a short exposure time (60 ms). Such sharp images of deformed erythrocytes enable us to make a quantitative analysis of erythrocyte deformation in the silica microcapillaries, which are a valuable tool for measuring erythrocyte deformability.

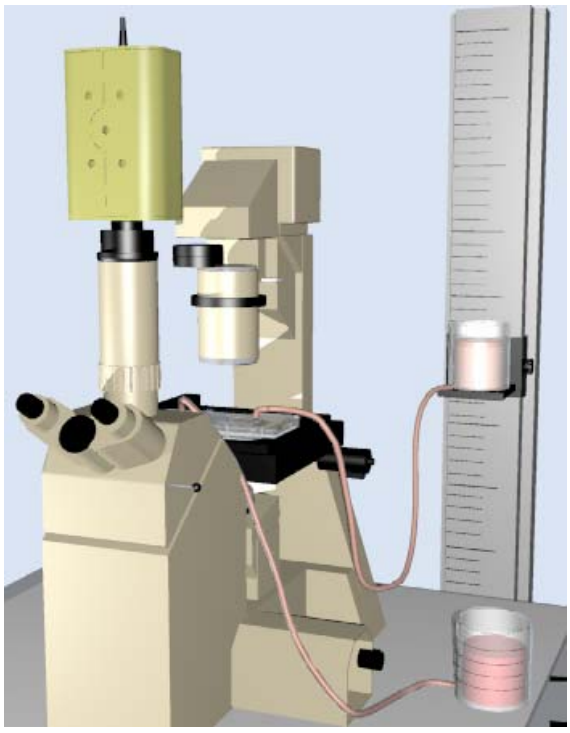

Figura 2-4: Detail of the flow cell: silica tubing

The large arrays of images (around 15,000 for each run) recorded by the high speed camera were processed off-line by a custom macro based the library of a commercial software package (Image Pro Plus 4.5) and allowing to isolate the subsets of images with cells passing through the field of view. Other macros were then used to calculate the velocity and shape parameters of each RBC. Around 300-500 RBCs were analyzed at each pressure drop.
In all the experiments, observations were performed in bright field, using short working distance optics (oil immersion objective, 100x Achroplan, Zeiss). The total

magnification was varied by using an additional lens holder (Optovar slider, Zeiss), with factors of 1.25x and 1.6x, and a zoom lens with a continuously adjustable zoom factor in the range 0.5 - 2.0x. The whole apparatus, which is shown schematically in Figure 2-4, was placed on a vibration-isolated workstation (Newport).

2.1.4 Image analysis

A cumbersome task like measuring thousands of cells can only be handled by automated methods. Image analysis techniques have been used to automatically measure red blood cell velocity and shape. The basic steps are background correction, edge cell detection and measurement and cell position measurement. These steps were implemented in a macro calling standard image analysis routines from a library of a commercial software package (Image Pro Plus). The main advantage of this approach is that it allows one to process a large number of images (typically corresponding to a few hundreds of cells), which would be very time-consuming if carried out manually. The measured quantitiesinclude is red blood cell velocity and contour points, thus allowing to reconstruct the 3D morphology of each cell.
During the experiment, at each pressure drop one movie is acquired. A movie usually contains about 15000 images (frames). In this work two different macros were used, to analyse both RBC velocity and deformability.
The steps of the automated analysis of RBC velocity are:

1. background correction, to clean out images (Figure 2-5a), and average image subtraction, to eliminate the tubing wall (Figure 2-5b); the image to be subtracted is obtained by averaging a certain number of frames from the original movie. In this way, the macro can be used to discriminate between a red blood cell and the rest of the image;

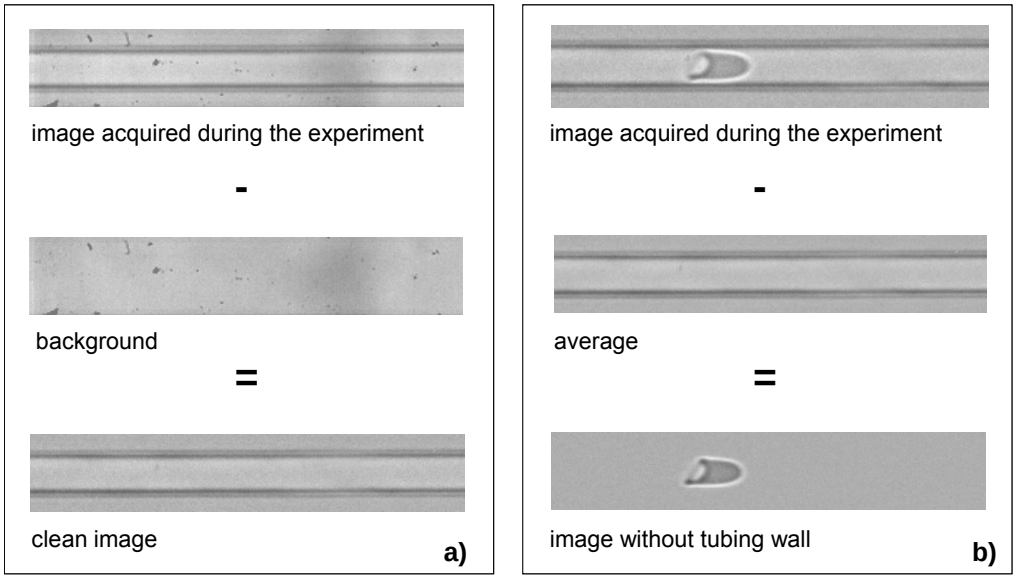

Figura 2-5: (a) Background subtraction, (b) average image subtraction

2. detection of the cell based on difference in mean gray level (MGL) between the cell and the rest of the image;
3. cell center-x and center y measurement for each frame;

4. RBC velocity calculation: knowing cell position from frame to frame it is possibile to generate a position *vs* time plot (Figure 2-6). The slope of this plot will be RBC velocity. Velocity of each RBC per pressure drop are then saved in a text document.

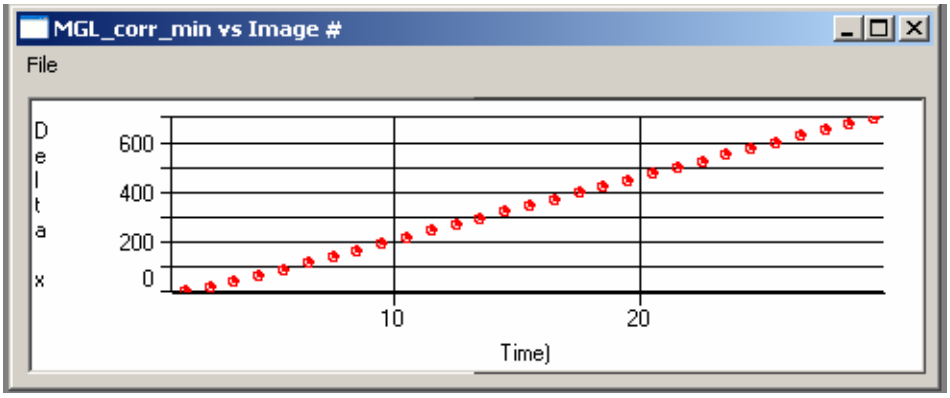

Figura 2-6: Plot of RBC position vs time

The steps of the automated analysis of RBC shape are:

1. selection of the cell by gray level thresholding (figure 2-7)
2. cell contour points measurement (Figure 2-8)

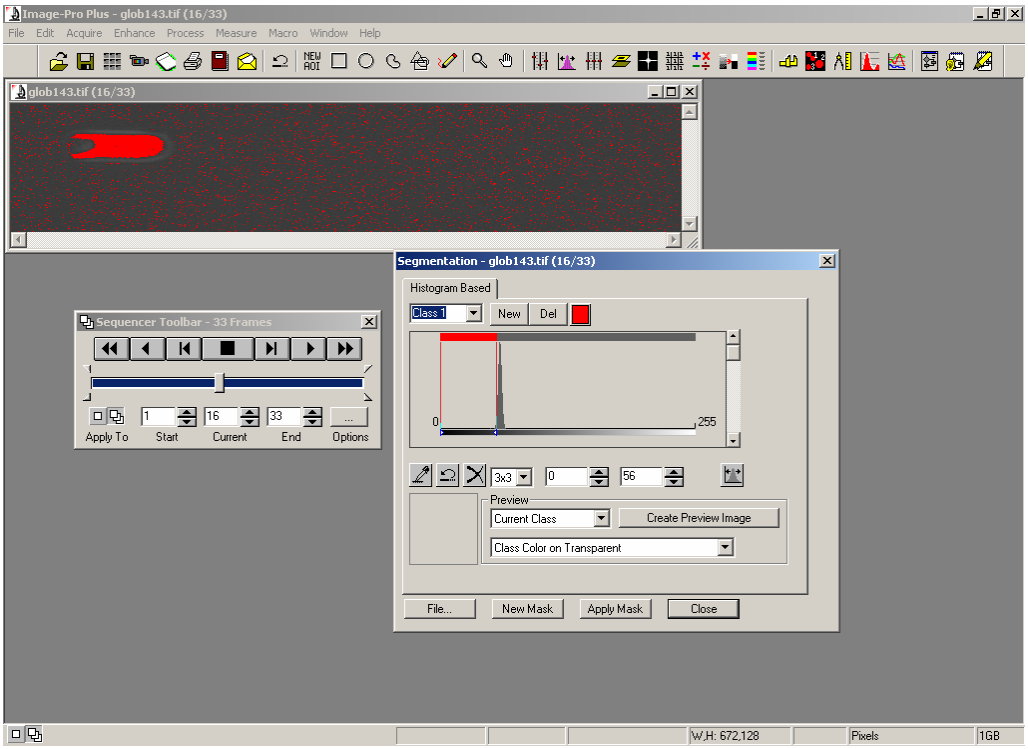

Figura 2-7: Detection af a red blood cell

3. deformation index (DI) calculation: DI is measured as the ratio between the major and the minor axis of a bounding box enclosing the cell body. Contour points and DI of each RBC per pressure drop are then saved in a text document.
A Matlab macro was also written to estimate red blood cell surface area and volume. For the axisymmetric RBCs volume and surface area were calculated from the acquired images by assuming a solid of revolution shape.

Figura 2-8: Red blood cell contour selection

2.2 RESULTS

2.2.1 Analysis of red blood cell shape and volume

The observed RBC shape is shown in Figure 2-9 as a function of microcapillary diameter and cell velocity. In the smallest microcapillary (D = 4.7 μm) all RBCs showed the typical axisymmetric bullet-like shape, tending to an asymptotic configuration at increasing cell velocity. Asymmetric shapes were mostly observed in the10 μm microcapillary, as shown in the bottom row of Figure 2-9.
At RBC velocity below 1 mm/s asymmetry was the result of folding of the cell membrane. At higher RBC velocities asymmetric shapes were due to out-of-axis cell position (which was prevented in the smallest microcapillary by the effect of confinement) and were associated with a slightly lower cell velocity.

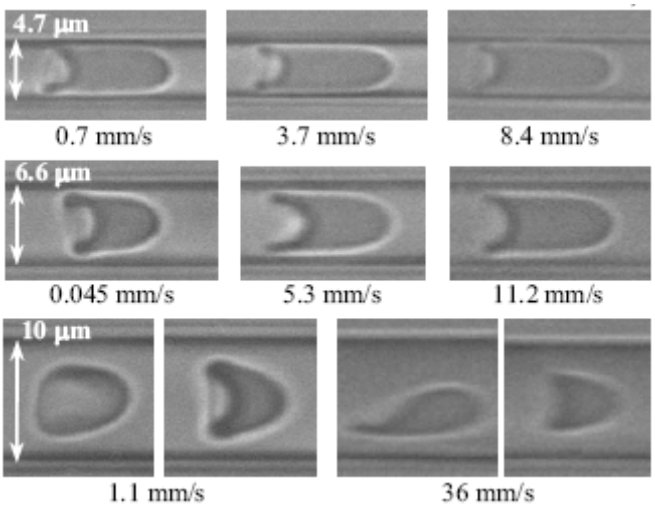

Figura 2-9: Images of RBCs flowing in microcapillaries with inner diameter D (in μm) equal to 4.7 (top), 6.6 (middle) and 10 (bottom)

As far as volume analysis is concerned, the resulting size distribution was in reasonable agreement with blood tests and data from the literature. Furthermore, a slight linear decrease of velocity with cell volume was found at any given pressure drop (Figure 2-10). This trend was paralleled by a corresponding slight increase of the suspending fluid layer surrounding the cell body in the region opposed to microcapillary wall, thus showing the fluidodynamic nature of such velocity variation.

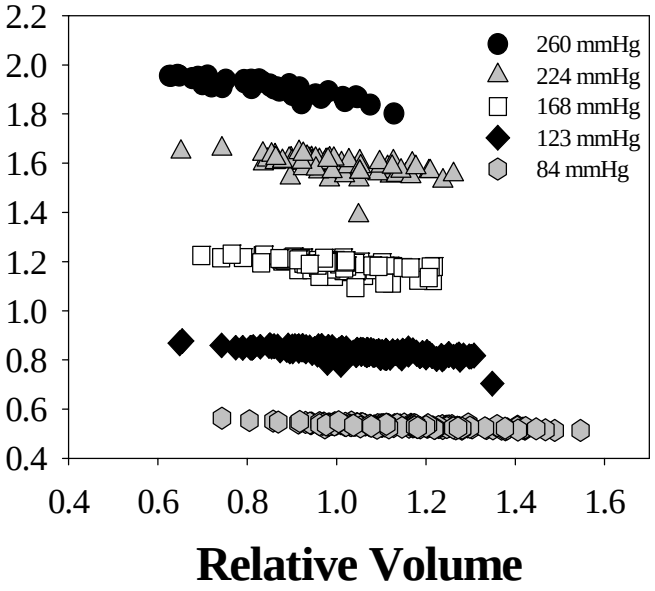

Figura 2-10: RBC velocity vs RBC volume at different pressure drop

A quantitative analysis of RBC shape is presented in Figure 2-11a, where cell length (measured as the side of a bounding box enclosing the cell body) at D = 4.7 and 6.6 μm is plotted as a function of RBC velocity in the diagram. An increasing trend is observed, with a leveling-off of cell length at values of RBC velocity around 1 mm/s.

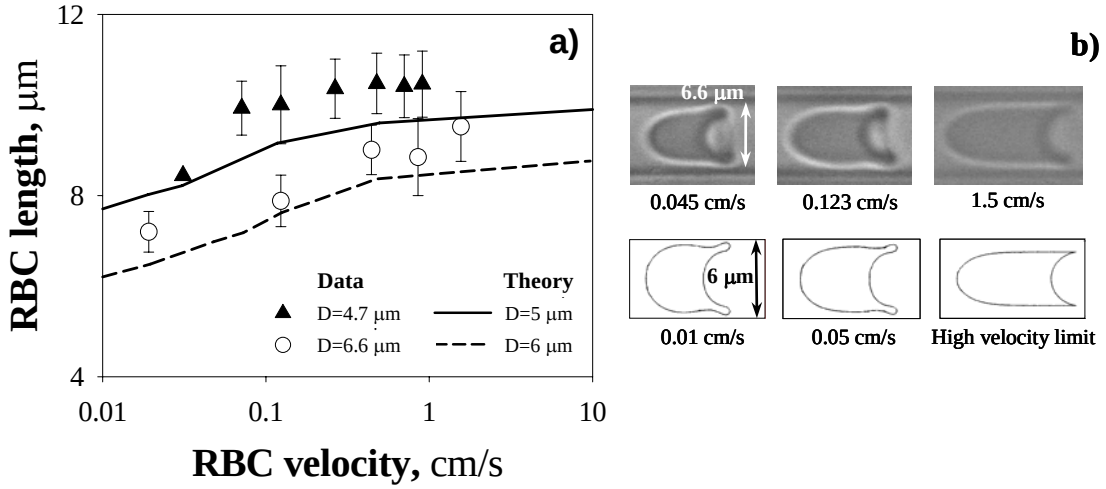

Figura 2-11: (a) plot of RBC length as a function cell velocity at microcapillary diameters of 4.7 and 6.6 μm; (b) comparison between images of flowing RBCs and theoretical predictions (Secomb 1986)

These results provide a quantitative evidence of the asymptotic shape which can be observed in the images of Figure 2-9. The continuous and dashed lines are predictions of the model by Secomb et al. (1986, 1987) for D = 5 and 6 μm, respectively. Model calculations are based on typical average values of surface area (135 μm^2) and volume (90 μm^3) for healthy RBCs, and on data of elastic shear modulus and bending rigidity of the membrane from the literature (Secomb et al. 1986, 1987) (the viscosity of the suspending fluid is taken equal to 1 cP). In other words, there are no adjustable parameters in model calculations, which makes more

remarkable the good agreement with the experimental data. Computed shapes at D = 6 μm are shown in Figure 2-11b in comparison with images at D = 6.6 μm for similar values of the RBC velocity. The predicted cell morphology is in good qualitative agreement with the observed shapes. In particular, at low RBC velocity a rim bulging outwards is found at the trailing edge, which turns out as mainly due to bending resistance in model calculations. The asymptotic configuration at high RBC velocity is calculated by assuming isotropic membrane tension, i.e., by neglecting the contribution of elastic shear and bending forces. In addition, due to the large values of isotropic membrane dilation a constant-surface area deformation is considered. In such conditions, the bullet-like flowing RBC exhibits a sharp cusp at the trailing concave edge. Inclusion of shear resistance may explain the slight buckling which is observed close to the rear region. The predicted asymptotic shape is then in good agreement with the experimental observations.

2.2.2 Analysis of red blood cell velocity

RBC velocity is plotted as a function of pressure drop in Figure 2-12 for the three microcapillaries shown in Figure 2-9 in very dilute cell suspensions (H_T = 0:5%). As expected, at the same pressure drop RBC velocity increases with microcapillary diameter. The continuous lines in Figure 2-12 correspond to the average suspending fluid velocity v_p as calculated from Poiseuille tube flow. The ratio between RBC velocity v_c and v_p is shown in Figure 2-13, and is an increasing function of D. In fact, the smaller is RBC size as compared to microcapillary diameter, the closer is cell velocity to the suspending fluid velocity at the same radial position. In each microcapillary v_c/v_p approaches a plateau value, with a value around 1.6 for D = 10 μm. Thus, RBC velocity stays in between the average and maximum velocity of the suspending fluid, the latter being twice the former in Poiseuille tube flow.

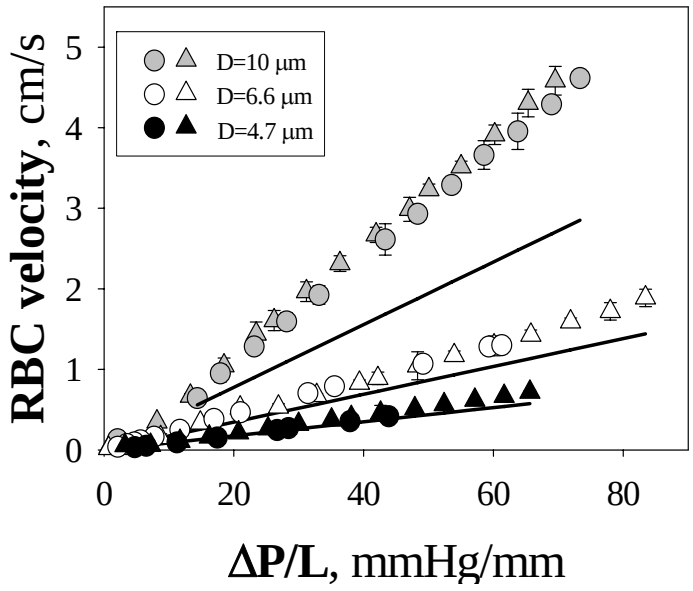

Figura 2-12: RBC velocity vs pressure drop per unit length at D = 4.7, 6.6 and 10 μm. Each set of data includes results from two independent experiments. Error bars represent the standard deviation of the measurements

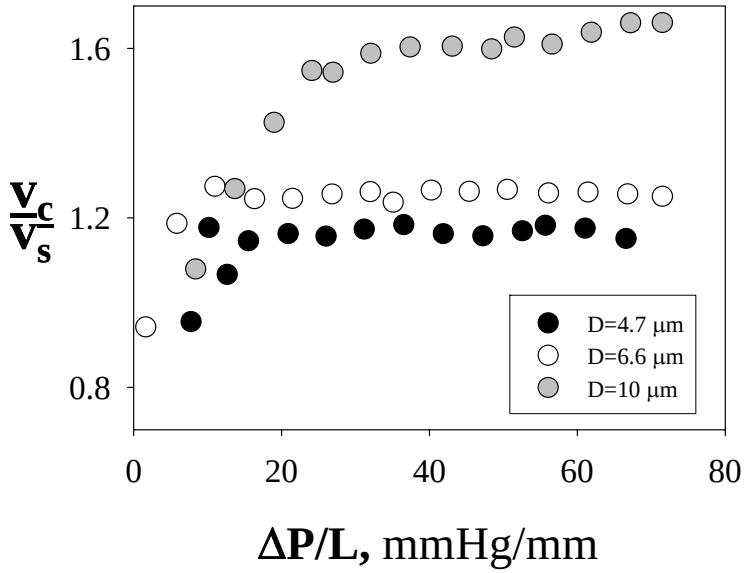

Figura 2-13: Ratio between RBC and suspending fluid average velocity (as calculated from Poiseuille flow)

The plateau values of RBC velocity are associated with the asymptotic shapes presented in Figure 2-9. In this regime, RBC velocity is a linear function of the pressure drop, in agreement with theoretical predictions. At pressure drops below the transition to the asymptotic shape the data of RBC velocity are closer to the average Poiseuille velocity of the suspending fluid. In these conditions RBCs tend to slow down the flow of the suspension and the apparent viscosity is predicted to increase at decreasing cell velocity. In Figure 2-14 the ratio H_T/H_D between tube and discharge hematocrit is plotted as a function of RBC velocity at D = 4.7 and 6.6 μm.

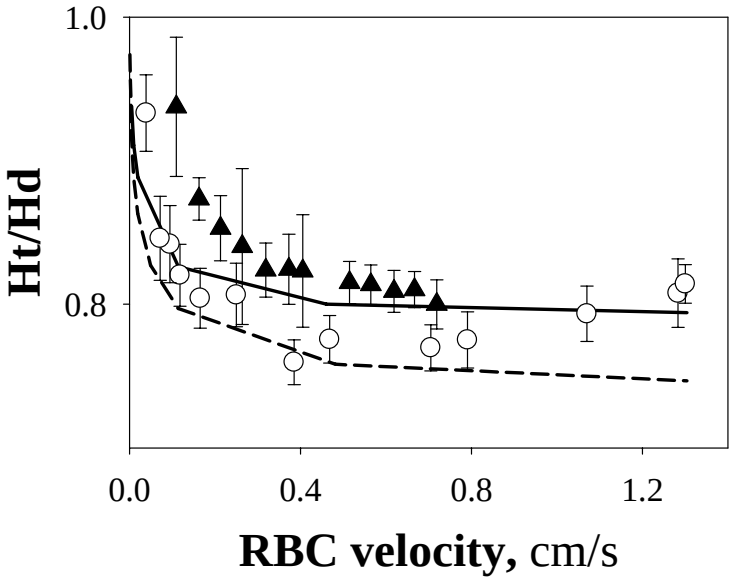

Figura 2-14: The ratio between tube and discharge hematocrit vs RBC velocity at 4.7 and 6.6 μm (full and open symbols, respectively), compared to theoretical predictions

From a material balance, $H_T/H_D = \langle v \rangle / v_c$, where $\langle v \rangle$ is the average velocity of the suspension, which is taken equal to v_p in the dilute case considered here. At both values of D H_T/H_D is a decreasing function of cell velocity, a result which can be

attributed to the fact that the velocity of RBCs relative to the suspending fluid grows with cell velocity.
Hence, RBCs leave the microcapillary earlier as compared to the suspending fluid, thus leading to a decrease of the tube hematocrit. As before, the lines are theoretical predictions (Secomb et al. 1986, 1987), and the agreement with experimental data improves at higher RBC velocities (this could be due to the slowing down at low pressure drops already mentioned, which is not taken into account in the calculation of H_T/H_D).

2.2.3 Effect of red blood cell concentration

The effect of increasing RBC concentration is presented in Figure 28, which refers to experiments at H_T = 0.2 and D = 10 μm. RBC velocity (open circles) is plotted as a function of pressure drop per unit length together with data of dilute suspensions (closed circles) from Figure 25. The star symbols (which are connected by a continuous line as a guide for the eye) are the values of the average suspension velocity as measured by tracking the motion of polystyrene beads far away from the flowing RBCs. The dashed line is the average velocity of the suspending fluid as calculated for Poiseuille flow. It can be noticed that at any pressure drop RBC velocity is quite close to that measured in the dilute case, whereas average suspension velocity is lower. Hence, the ratio v_c/v_p (which takes a limiting value around 2 at high RBC velocity) is higher than the one obtained for the dilute case (i.e., 1.6 from Figure 26). The images shown in in the inset show that RBC shapes are also quite similar to the ones observed in dilute suspensions. At low pressure drops RBCs tend to create trains or *rouleaux* led by a slightly larger cell which slows down the preceding ones, in agreement with the dependence of RBC velocity on cell size found in the dilute case.

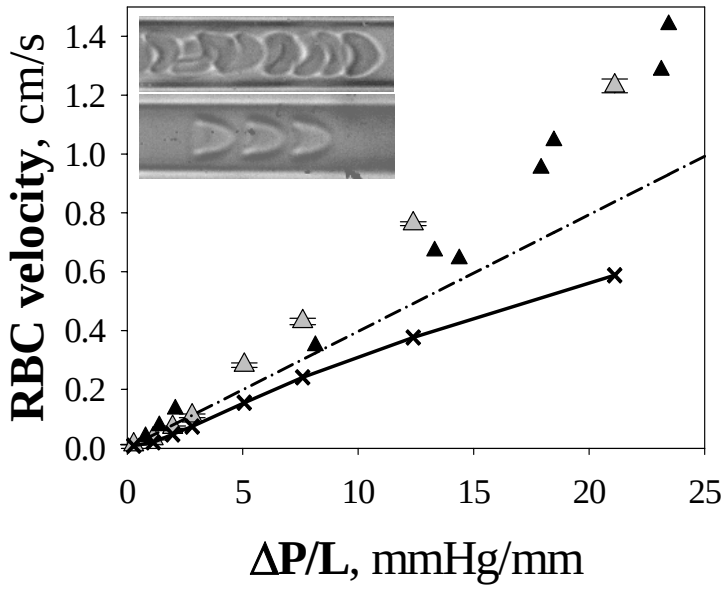

Figura 2-15: RBC velocity vs pressure drop per unit length. Images in the inset correspond to RBC velocity of 121 (top) and 1100 (bottom) μm/s

Such *rouleaux* disappear at higher pressure drops (see bottom image in the inset). A comparison with theoretical predictions is presented in Figure 2-16, where experimental data of H_T/H_D are plotted as a function of RBC velocity at D = 10 μm. The continuous line corresponds to calculations made for D = 8 μm (Secomb et al.

1986, 1987) which show some discrepancy with the experimental data. Nevertheless, the overall agreement with theoretical predictions looks quite satisfactory.

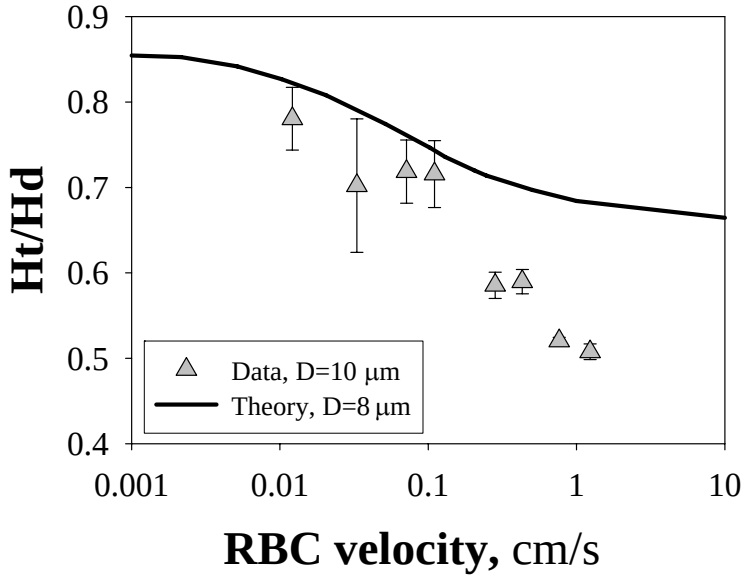

Figura 2-16: H_T/H_D vs RBC velocity at D = 10 μm and H_T = 0.22

2.2.4 Effect of albumin concentration

The effect of the supplemented albumin on RBC velocity (Figure 2-17) and shape (Figure 2-18) was also tested, and no significant dependence were found by changing the albumin concentration from 1 to 5 mg/ml.

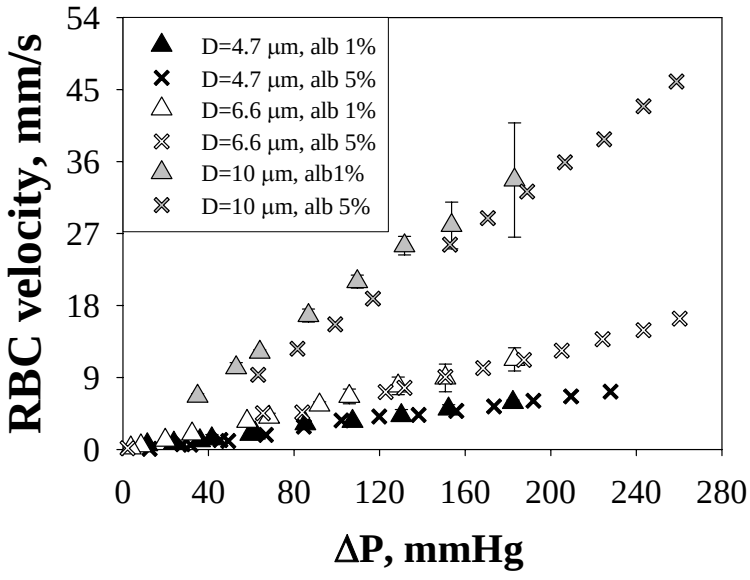

Figura 2-17: RBC velocity vs ΔP at different albumin concentrations (1% and 5%)

In Figure 2-18 is plotted the RBC deformation index *DI* (measured as the ration between the long and the short side of a bounding box enclosing the cell body) as function of pressure drop at two different albumin concentration 1 and 5 mg/ml.

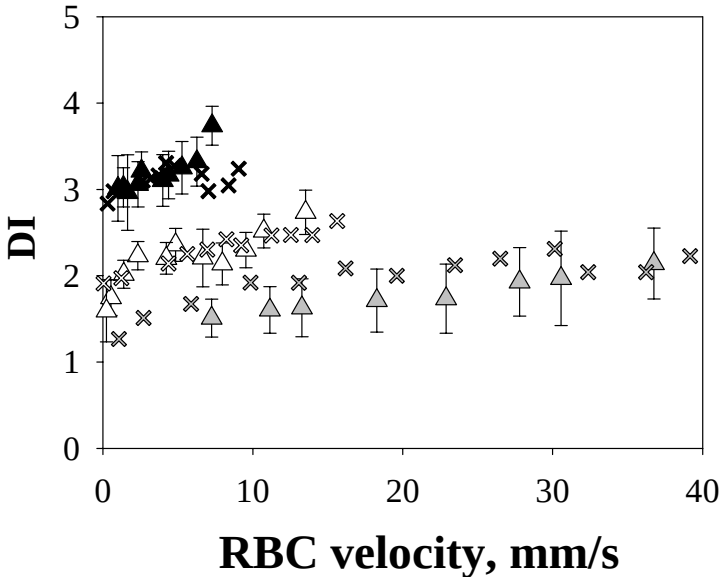

Figura 2-18: DI vs RBC velocity at different albumin concentrations (1% and 5%). Same symbols as in Fig. 30

2.3 PRELIMINARY RESULTS ON PATHOLOGICAL RBCs

The investigation of the flow behavior of blood samples from patients, apart from its biomedical significance, is also relevant to the objective of this work by providing an experimental background to evaluate how pathological blood may interact with artificial devices. In this section preliminary results on pathological red blood cells are presented and discussed; in particular, samples from patients suffering from polycythemia and from thalassemia were analyzed.

2.3.1 Polycythemia

Polycythaemia (or erythrocytosis) has been used to identify a group of various disorders in which there is a net increase in the total number of blood cells, primarily red blood cells, that are typified by a persistently raised haematocrit (Hct). The overproduction of red blood cells may be due to a primary process (*primary polycythemia)* in the bone marrow (a so-called myeloproliferative syndrome), or it may be a reaction to chronically low oxygen levels or, rarely, a malignancy. *Primary polycythemia*, often called *polycythemia vera* (PCV) occurs when excess red blood cells are produced as a result of an abnormality of the bone marrow. Often, excess white blood cells and platelets are also produced. Polycythemia vera is classified as a myeloproliferative disease. A hallmark of polycythemia is an elevated hematocrit. *Secondary polycythemia* is caused by either natural or artificial increases in the production of erythropoietin, hence an increased production of erythrocytes. In secondary polycythemia, there may be 6 to 8 million and occasionally 9 million erythrocytes per cubic millimeter of blood. Secondary polycythemia in which the production of erythropoietin increases appropriately is called *physiologic polycythemia*. Causes of secondary polycythemia include smoking, renal or liver tumors, hemangioblastomas in the central nervous system, heart or lung diseases that result in hypoxia, and endocrine abnormalities including pheochromocytoma and

adrenal adenoma with Cushing's syndrome. Athletes and bodybuilders who use anabolic steroids or erythropoietin may develop secondary polycythemia.

In this work, preliminary experiments both on secondary and primary polycythemia were carried out and compared to healthy samples.
In Figures 2-19 and 2-20 RBC velocity and shape of one secondary polycythemia patient are plotted and compared with data from healthy RBCs. It is clear that secondary polycythemia data superimpose on healty data.

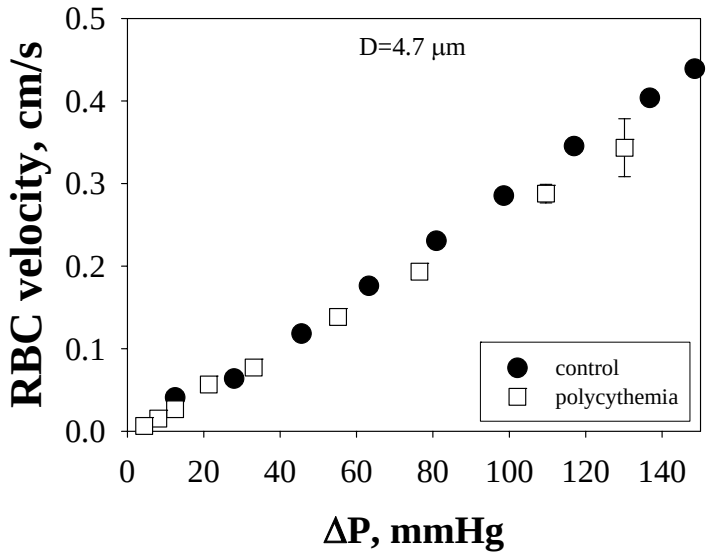

Figura 2-19: RBC velocity vs pressure drop for one samples from secondary polycythemia patient and one control from a healthy donor

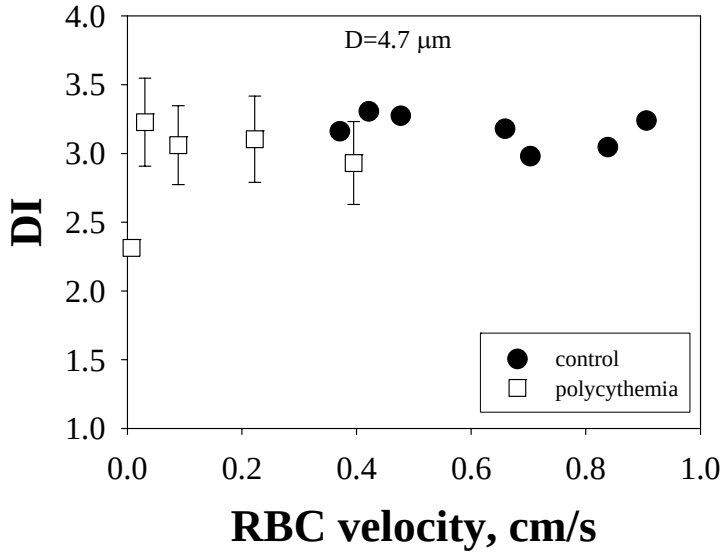

Figura 2-20: Relationship between erythrocyte velocity and deformation index for healthy control and for polycythemic erythrocytes

In Figure 2-21 the RBC velocity of one polycythemia vera patient is plotted as a function of the liquid head. In the same figure, results from healthy RBCs are also shown for comparison. In this case too, there is no difference between pathological and healthy RBC velocities.

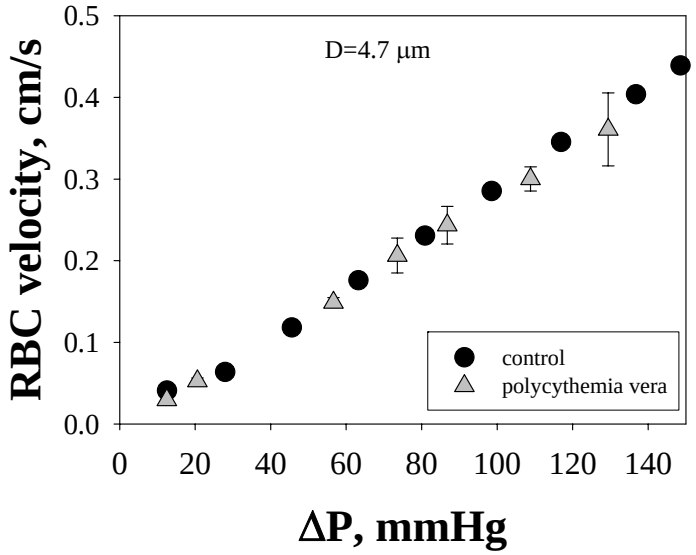

Figura 2-21: RBC velocity vs pressure drop for one sample from polycythemia vera patient and one control from a healthy donor

Concerning red blood cell shape (Figure 2-22), instead, polycythemia vera data do not superimpose on healty sample data, but exhibit different values of the deformation index. In particular, DI from pathological samples is higher as compared to the control. This is not unexpected, since the MCV (mean corpuscolar value) is equal to 119.4 fL (way out of the normal range 80-99 fL): this means that RBCs are bigger than normal.

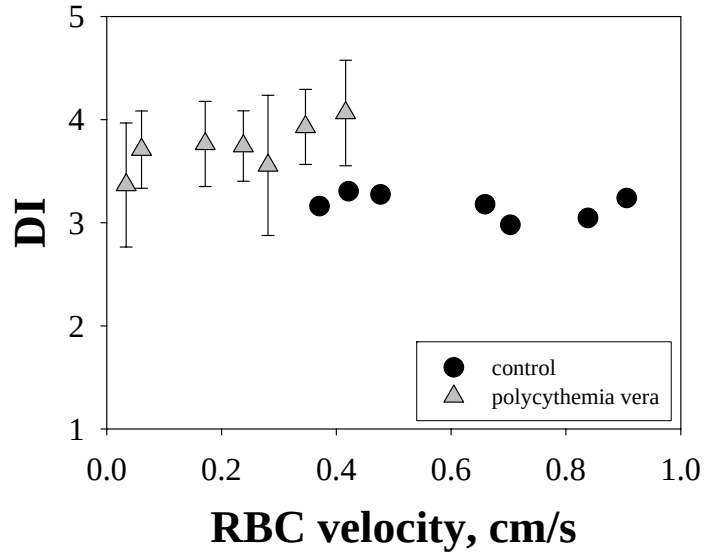

Figura 2-22: Relationship between velocity and deformation index for normal and polycythemia vera erythrocytes

Some hematological data for this case (as compared to the control) are shown in Table 2-1.

sample	HGB, g/dl	HCT, %	MCV, fL
control	13.2	42.1	85.6
PCV	12.6	38.8	119.4

Table 2-1: Haematological data of the blood samples of Figure 2-21 and 2-22

2.3.2 Thalassemia

Thalassemias are inherited blood disorders. "Inherited" means they are passed on from parents to children through genes. Thalassemias cause the body to make fewer healthy red blood cells and less hemoglobin than normal.
Normal hemoglobin, also called hemoglobin A, has four protein chains: two α globin and two β globin. The two major types of thalassemia, α and β, are named after defects in these protein chains.
Four genes are needed to make enough α globin protein chains. α thalassemia trait occurs when one or two of the four genes are missing. If more than two genes are missing, the result is moderate to severe anemia. The most severe form of α thalassemia is known as α thalassemia major or hydrops fetalis. Babies with this disorder usually die before or shortly after birth.
Two genes (one from each parent) are needed to make enough β globin protein chains. β thalassemia occurs when one or both genes are altered. The severity of β thalassemia depends on how badly one or both genes are affected. If both genes are affected, the result is moderate to severe anemia. The severe form of β thalassemia is known as thalassemia major or Cooley's anemia.
Rheological properties of many genetically variant erythrocytes with abnormal hemoglobin (Hb) synthesis or structure are known to be altered (Rachmilewitz et al. 1985, Mohandas et al. 1983, Schreier et al. 1989, Rice-Evans et al. 1982, Tillmann et al. 1979) and are likely to contribute to the shortened lifespan of such cells and other pathologic complications. Micropore filtration studies (Tillmann et al. 1979) show moderately diminished cell flexibility of erythrocytes from heterozygous β-thalassemic patients ascribed to microcytosis, rigidity of erythrocytes in homozygous patients due to altered cell shape, diminished Hb fluidity and, for splenectomized patients, the presence of inclusion bodies. Both α- and β-thalassemic erythrocytes have excess surface area in relation to cell volume, increased membrane rigidity, and decreased ability to undergo cellular deformation under hypertonic osmotic stress (Schrier 1989).

In this work preliminary experiments on α and β-thalassemia were carried out and compared to healthy samples. In Figure 2-23, the RBC velocity of four heterozygous β-thalassemia patients is plotted as a function of the liquid head. In the same figure, results from healthy RBCs are also shown for comparison. Figure 2-23 shows that data from the β-thalassemia patients investigated in this work follow a linear trend passing through the origin. At variance with the healthy RBC results, however, β-thalassemia data do not superimpose on the same “master curve”, but rather exhibit different slopes, one being even coincident with the healthy case. The remaining three pathological data sets fall significantly below the velocity of healthy RBCs (the

slopes are between 64% and 35% smaller), thus showing an increased hydrodynamic resistance in microcapillary flow. Figure 2-24 shows representative images of flowing β-thalassemia RBCs from the four samples investigated at a liquid head of ca. 6.5 mmHg. A parachute-like cell shape was observed in most images of the flowing RBCs, in analogy with the healthy samples.

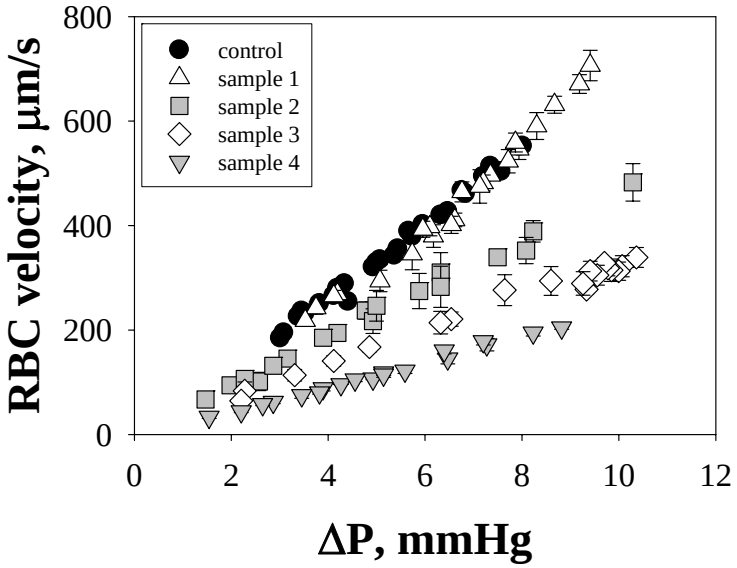

Figura 2-23: RBC velocity vs liquid head for four samples from β-thalassemia patients and one control from a healthy donor

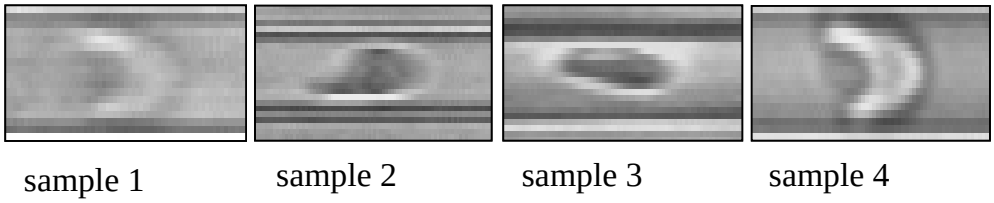

Figura 2-24: Representative images of flowing β-thalassemia RBCs from the four samples investigated

Some hematological data for the blood samples of Figure 2-24 are presented in Table 2-2. No simple correlation between RBC velocity and hematological parameters can be derived from Table 2-2.

sample	HGB, g/dl	HCT, %	MCV, fL
control	13.2	42.1	85.6
1	15	47.7	75.5
2	8.8	30.1	65.6
3	13	40.8	60.1
4	13.9	43.8	72.2

Table 2-2: Haematological data of the blood samples of Figure 2-23

Preliminary data for α-thalassemia patients are compared to the healthy case in the plot in Figure 2-25. The two pathological sets are below the healthy data and superimpose on each other. Moreover, as shown in Figure 2-26, α-thalassemia RBCs deform into a parachute-like shape, in analogy with the healthy samples.
A systematic investigation to extend these preliminary results is currently in progress.

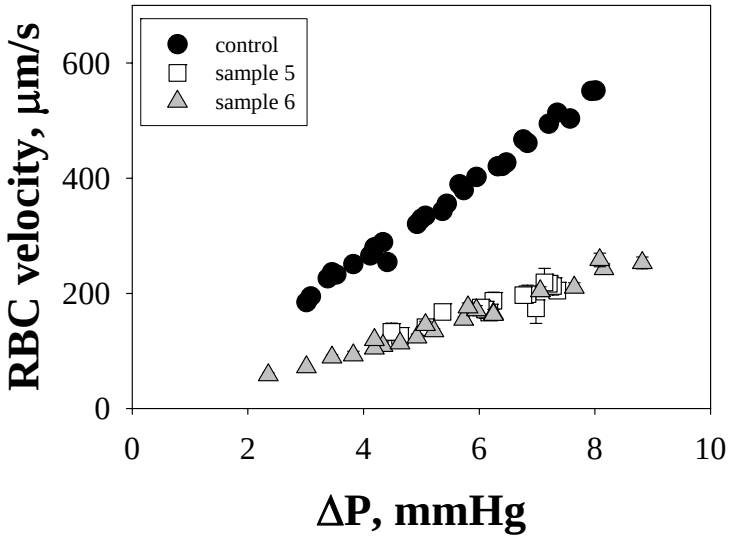

Figura 2-25: RBC velocity vs liquid head for two samples from α-thalassemia patients and one control from a healthy donor

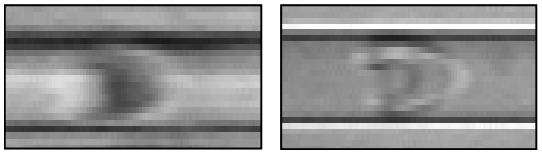

sample 5 sample 6

Figura 2-26: Representative images of flowing α-thalassemia RBCs from the two samples investigated

In conclusion, this research activity concerns a systematic investigation of RBC deformation and velocity in artificial microcapillaries with diameter comparable to cell size. We provide for the first time a thorough quantitative comparison with theoretical predictions from the literature, and find a good agreement with no adjustable parameters. The main application of these results is to provide a benchmark of healthy RBC flow behavior to be used as a reference relevant to the study of pathological conditions where an altered cell deformability is advocated, but the understanding of its implications is still elusive due to the lack of adequate experimental methods. The main application of these results is to provide a benchmark of healthy RBC flow behavior to be used as a reference relevant to the study of pathological conditions where an altered cell deformability is advocated, but the understanding of its implications is still elusive due to the lack of adequate experimental methods. The system presented here could be also used to evaluate the effects of drugs on cell deformability in microcirculation.

Chapter 3 MICROFLUIDIC DEVICE TO SIMULATE HUMAN MICROCIRCULATION

3.1 MATERIALS AND METHODS

3.1.1 Soft lithography

Soft lithography consists in the transfer of a pattern from a photomask to a photosensitive material (*photoresist*, or simply *resist*) on a substrate (*wafer*) by selective exposure to a radiation source such as light.
Typically lithography is performed as part of a well-characterized procedure, which includes the wafer surface preparation, photoresist deposition, alignment of the mask and wafer, exposure, develop and appropriate resist conditioning. The lithography process steps need to be characterized as a sequence in order to ensure that the remaining resist at the end of the procedure is an optimal image of the mask, and has the desired sidewall profile.
The *photomask* is a high precision plate containing microscopic images of the pattern to be tranferred to the resist on the wafer. It is made from very flat pieces of quartz or glass with a layer of chrome on one side. A portion of the pattern is etched in the chrome. This pattern on the mask is also called *geometry*. Cr is not transparent to UV light which makes it is possible to illuminate chosen areas of a substrate through the mask. When you order the mask you can specify it as bright field or dark field. Bright field means that the Cr mask will look exactly like your layout, while dark field means that you will get the negative. The mask used in this work is shown in Figure 3-1.

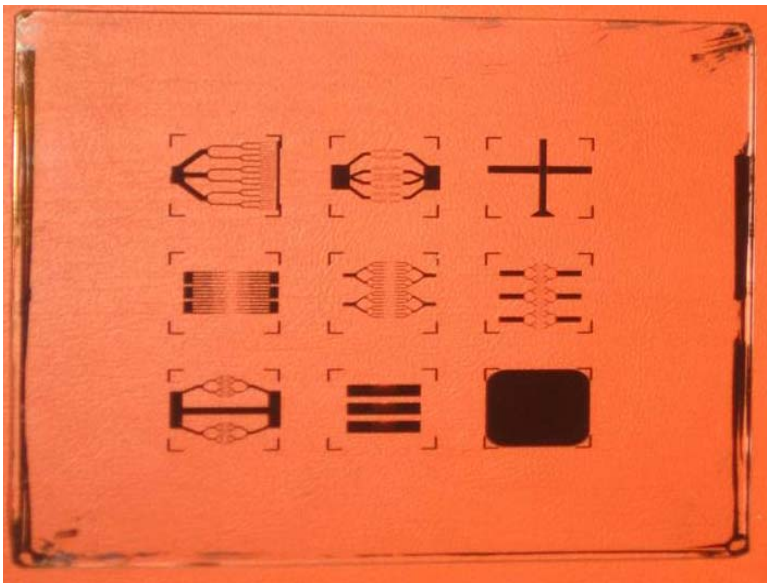

Figura 3-1: Chrome photomask

The Cr mask is in general a 5 inch square, so it is possible to draw 9 different geometries (each geometry is 1 cm square).
The network pattern (Figure 3-2 and 3-3) was drawn by a layout program, LASI 7, a commercial software widely used to draw electric microcircuits. We fabricated the microchannels to mimic capillaries with diameter between 5 (often in the middel of

the geometry) and 500 μm. The average flow velocity in the central channels constrictions was chosen to model the natural flow rates in capillaries.

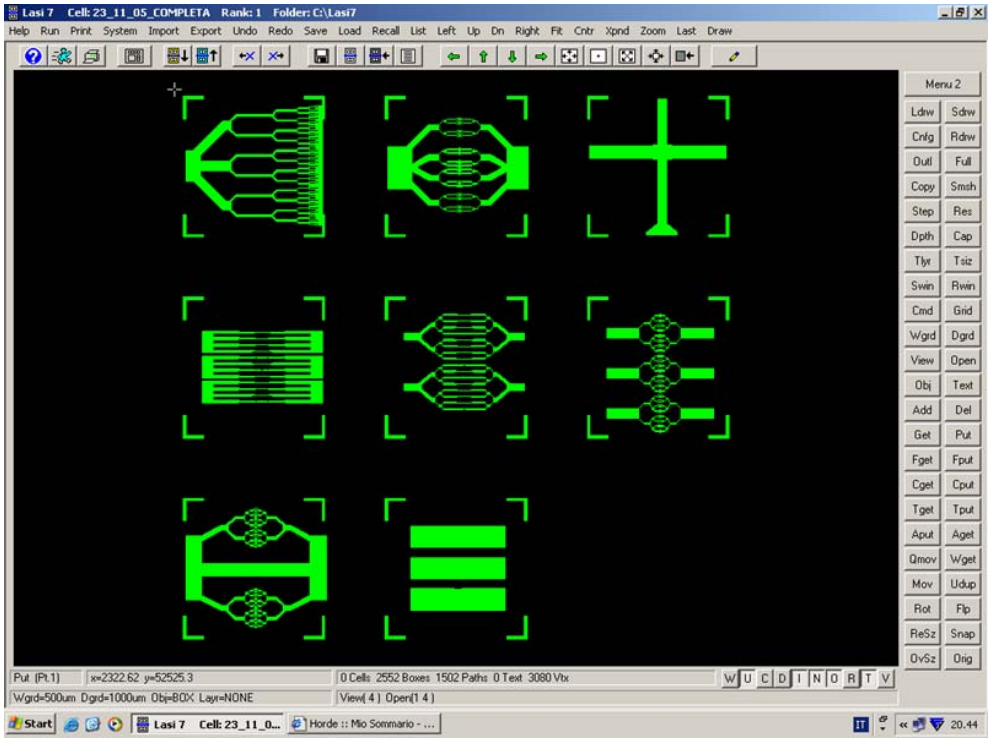

Figura 3-2: Lasi7 layout

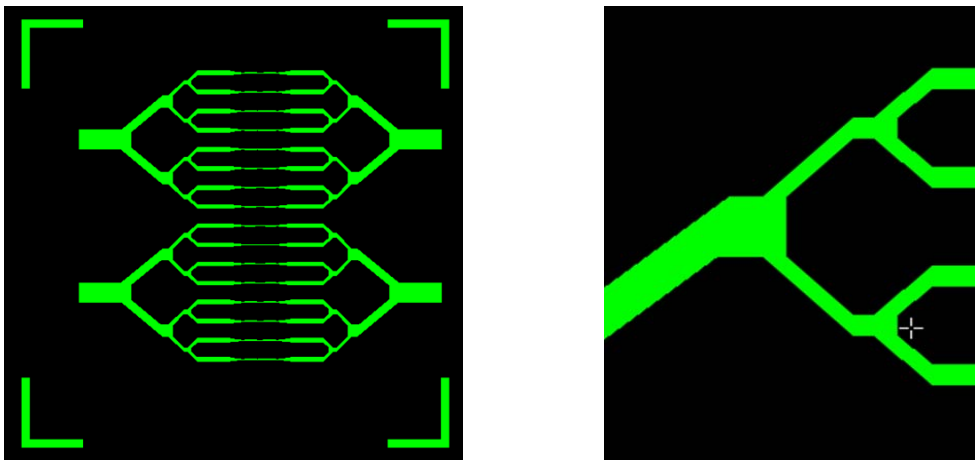

Figura 3-3: Details of one of the geometries

Concerning the *photoresists*, two types cab be used: positive and negative. For positive resists, the resist is exposed with UV light wherever the underlying material is to be removed. In these resists, exposure to the UV light changes the chemical structure of the resist so that it becomes more soluble in the developer. The exposed resist is then washed away by the developer solution, leaving windows of the bare underlying material. In other words, "whatever shows, goes". The mask, therefore, contains an exact copy of the pattern which is to remain on the wafer. Negative resists behave in just the opposite manner. Exposure to the UV light causes the negative resist to become polymerized, and more difficult to dissolve. Therefore, the negative resist remains on the surface wherever it is exposed, and the developer

solution removes only the unexposed portions. Masks used for negative photoresists, therefore, contain the inverse (or photographic "negative") of the pattern to be transferred. The figure below (Figure 3-4) shows the pattern differences generated from the use of positive and negative resist.

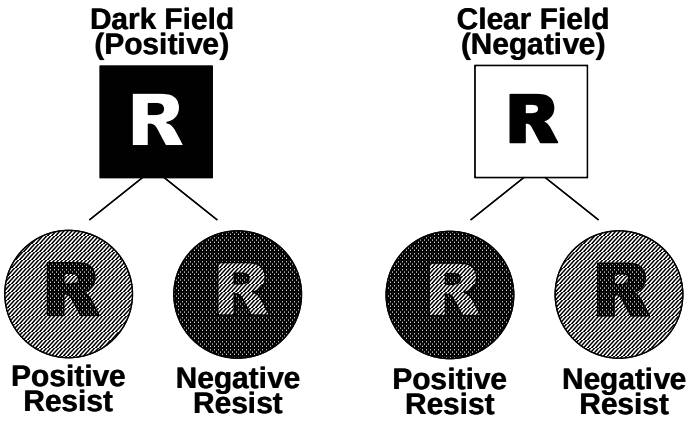

Figura 3-4: Pattern definition in negative and in positive resist

A master/template is needed to mould a stamp. A cheap and quite fast way is to provide a Si wafer with epoxy structures by common lithography. In this work the template usually consists of a 1 cm Si wafer as carrier substrate with epoxy structures on top. The epoxy used in this work is called SU-8 (Microchem). SU-8 photoresist is manufactured in different grades, determined by the amount of solids with respect to the solvent. A number behind the 'SU-8' indicates the grade of a certain SU-8, e.g. SU-8(2), SU-8(5), SU-8(10). 2 has the lowest viscosity and 500 the highest.

The standard steps found in a lithography module are (in sequence): resist spin, soft bake, alignment, exposure, post exposure bake, develop and hard bake. A brief explanation of the process steps is included for completeness.

Resist spin: coating of the wafer with resist by spinning to have an uniform coat. Figure 3-5 shows four basic stages of a typical spin coating process, in which a stream of photoresist is dispensed onto the surface of a spinning wafer; these are deposition, spin-up, spin-off and solvent evaporation.

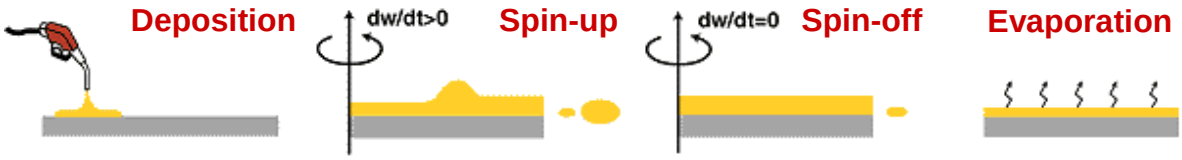

Figura 3-5: Typical stages of the spin coating process

The first three stages are somewhat overlapping and sequential in that the dispensed photoresist outflows convectively, under the influence of centrifugal force, covering the entire surface. Solvent evaporation, on the other hand, continues throughout the process. During the spin-off stage, the resist film is thinned down to a thickness

whose uniformity profile is primarily determined by two competing mechanisms (mass transfer and evaporation). According to this figure, convective outflow is the dominant thinning mechanism initially. However, increased viscosity because of relatively small but constant solvent evaporation causes convective outflow to decrease with time. A few seconds after the end of dispense, solvent evaporation becomes the dominant mechanism and determines final film thickness and uniformity. The thinning rate because of evaporation starts to decrease after about 5 sec from deposition because of lowered diffusivity of the remaining solvents within the semisolid photoresist film. Since the viscosity differs, the spin speed has to be adjusted accordingly. MicroChem Corporation has a bulletin board where characteristic thickness at different spin speeds (example in Table 3-1) can be found.

Product Name	Viscosity (cSt)	Thickness (µms)	Spin Speed (rpm)
		1.5	3000
SU-8 2	45	2	2000
		5	1000
		5	3000
SU-8 5	290	7	2000
		15	1000
		10	3000
SU-8 10	1050	15	2000
		30	1000
		15	3000
SU-8 25	2500	25	2000
		40	1000

Table 3-1: Resist thickness at different spin speeds

Successful implementation of a reduced photoresist consumption process requires a detailed understanding of these mechanisms. At the end of a coat process, the film still contains some solvent, and its thickness changes dynamically as it interacts with its local environment until it is delivered to the soft bake module, where final target thickness, uniformity and solvent content are achieved. The coating is less sensitive to the environment following the soft-bake step.
In this work SU-8 (5) was used, to have a 5 µm template thickness.

Soft bake: The wafer with the SU-8 film needs to be baked prior to the exposure. This is done to remove any remaining solvent and stabilize the film. The pre-exposure bake also makes the surface non-sticking, which prevents it from leaving remains on the Cr mask. The pre-exposure bake is done on a hot plate at 100°C for ¼ to ½ min per micrometer of film thickness. For really thick films this can take several hours. After the bake the resist needs to cool off before exposure. Minimum cooling time is ~5 min (10-30 µm film thickness).

Alignment: One of the most important steps in the photolithography process is mask alignment. The mask is aligned with the wafer, so that the pattern can be transferred onto the wafer surface. In this step, the wafer is loaded in a mask alignment tool called *mask aligner* (Karl Suss).

Exposure: After the wafer and the mask are properly aligned, the mask and the wafer are brought into contact and UV light is shined on the wafer (Figure 3-6). The dark regions of the mask will prevent UV light from reaching certain regions of the photoresist layer. The clear regions will allow UV light to chemically modify the underlying material. Depending on the photoresist type, UV may cross-link (strengthen) or increase the solubility of the resist in the developer solution.

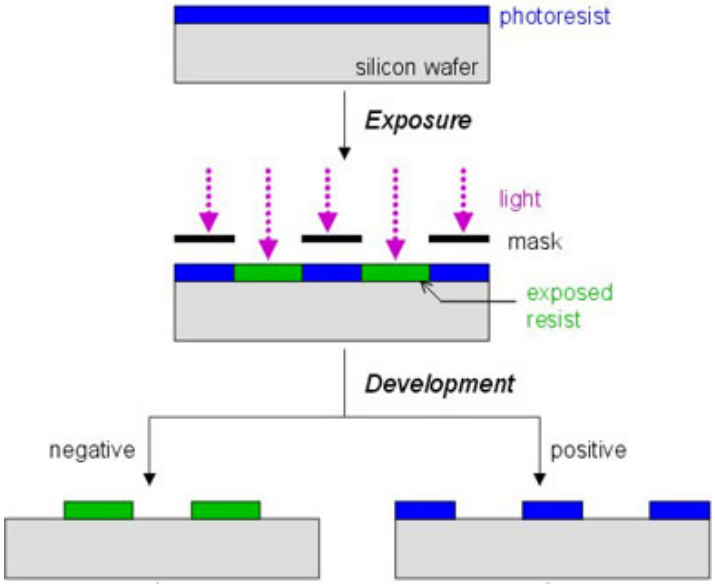

Figura 3-6: Exposure and development

SU-8 is a negative resist, meaning exposed areas will cross-link and remain after development. The exposure time/dose is depending on resist thickness. SU-8 can be over-exposed although it is not common. A ~20 s exposure is in sufficient in the 5-10 µm range of film thickness.

Post exposure bake: The post-exposure bake continues the polymerization process and is done in an oven at 100°C for 30 min. During the bake the pattern starts to stand out.

Development: The development of the photoresist consists of the selective etching of the regions either exposed or protected from UV light. This is done by placing the wafer with the film in a SU-8 developer (ethylene glycol monomethyl ether acetate) bath for a few minutes. The developer solution will attack the exposed regions and the unexposed regions at very different etch rates (i.e., the selectivity is high). In the case of SU-8 (negative resist), the regions exposed to UV light become more soluble in the developing solution.

Hard bake: Once the wafer has been inspected and approved, it is hard baked at 120 °C for 30 minutes. This will harden and strengthen the photoresist. At this point the wafer photolithography process is completed.

3.1.2 PDMS stamp

The stamp is the key in soft lithography since it is used to generate the pattern. The stamp is made of silicone, also called PDMS (polydimethylsiloxane), or Sylgard 184 (Dow Corning). PDMS is its chemical name, while Sylgard 184 its commercial name. Dow Corning Sylgard 184 is transparent and has low viscosity as uncured, both favorable features when making stamps and using them for soft lithography. PDMS has unique combination of properties resulting from the presence of an inorganic siloxane backbone and organic methyl groups attached to silicon. It has very low glass transition temperatures and hence it is fluid at room temperature. This liquid material can be readily converted into solid elastomer by cross-linking. The formulation, fabrication, and applications of PDMS elastomers have been extensively studied and are well-documented in the literature. Sylgard 184 has a very low resistance to most non-polar solvents. The stamp will in general not be destroyed by the solvents, rather deformed by swelling and will regain its original shape once the solvent has evaporated. Sylgard 184 is a two-component heat-curing system: it consists of a base part and a curing agent part. The standard steps to make a PDMS stamp are: mixing one part of curing agent and ten parts of base (by weight); degassing: after the mixing the silicone mixture will be full of air bubbles and needs degassing. This is done under vacuum. During degassing the silicone expands and starts to look like a foam. When the silicone is completely clear and transparent degassing is complete; dispensing the silicone onto the template: the material is dispensed at the center of the template from a small height, to minimize the risk of trapped air. The template is kept horizontal during dispensing; curing: PDMS is curable from less than room temperature to over 150°C. Sylgard 184 has temperature dependant shrinkage as seen below (Figure 3-7); peeling off the stamp from the template (Figure 3-8).

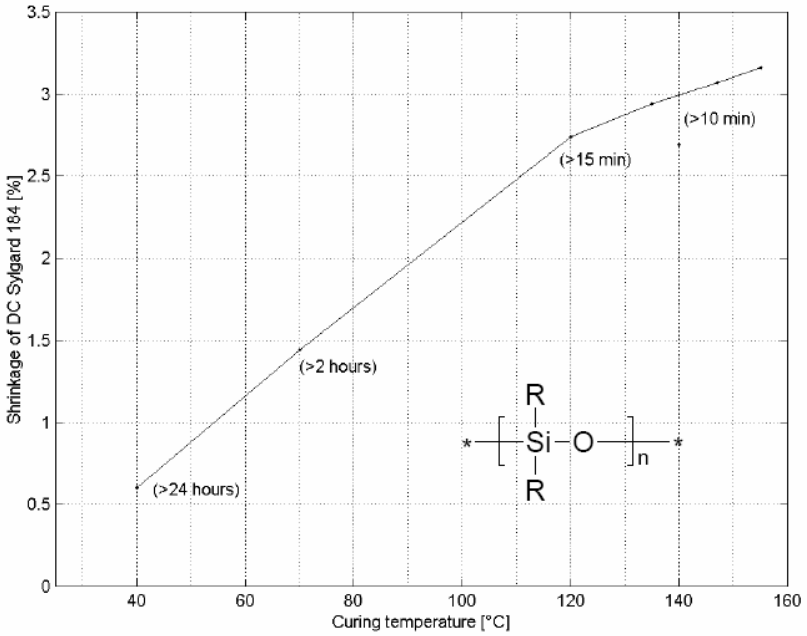

Figura 3-7: PDMS shrinkage vs curing temperature

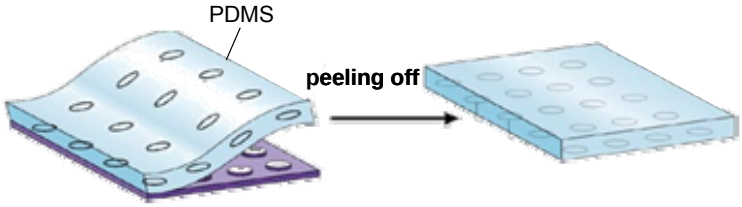

Figura 3-8: PDMS peeling off

3.1.3 Creation of microchannels

PDMS channels were sealed irreversibly to a coverslip slide by oxidizing the PDMS surface by using Corona treating, which also caused the channels to become hydrophilic. Corona treating is a very effective way to increase the surface tension of virtually any material. The result after corona treatment is a surface that is unchanged to the naked eye, but in fact is much more receptive to inks, coatings, and adhesives. The material being treated is exposed to an electrical discharge, or "corona." Oxygen molecules within the discharge area break into their atomic form and are free to bond to the ends of the molecules in the material being treated, resulting in a chemically activated surface. In this work a Laboratory Corona Treater (Figure 3-9) was used.

Figura 3-9: Laboratory Corona Treater

The Laboratory Corona Treater changes the surface energy of certain substrates by exposing them to highly charged electrical ions. The two opposing high voltage electrodes create an arc of electrons from one to the other. The electrons change the wettability of the material surface so that the inks, coatings, and adhesives cross-link with the polymer surface. Hence, the inks, coatings, and adhesives adhere properly to the part. So, to create microchannels, both PDMS stamp (the side with pattern) and glass slide surfaces were exposed to electrical discharge, then the microchannels were sealed by apposition of the glass slide (Figure 3-10) without compressive force.

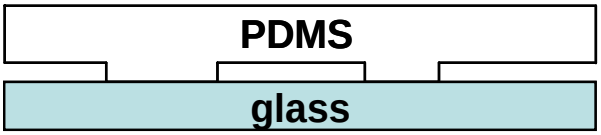

Figura 3-10: Schematic illustrating the microchannel

The coverslip slide with PDMS microchannels was inserted in the bottom plate of a flow cell very similar to the one used for silica microcapillaries. So, also in this case the flow cell (a schematic is shown in Figure 3-11) was made of two Plexiglass plates separated by a rubber spacer. A window was cut to allow insertion of the coverslip slide for observations at high magnifications with oil immersion objectives.

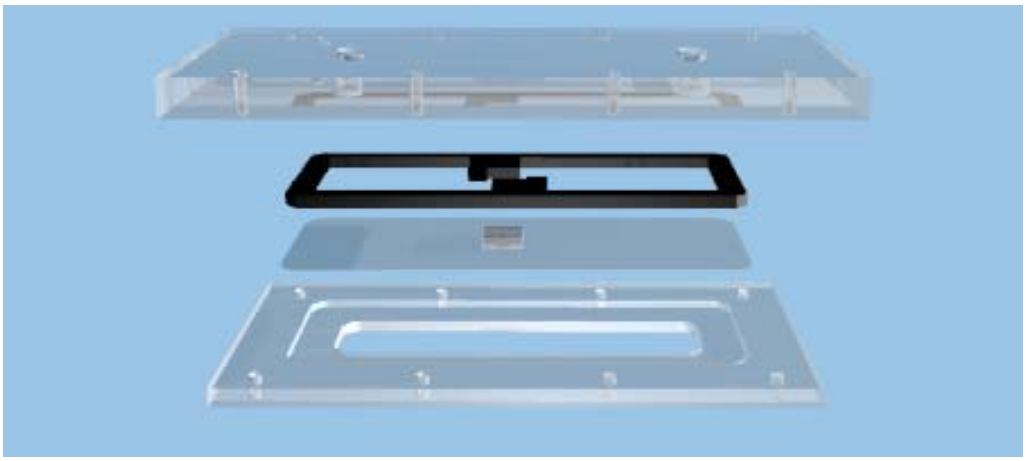

Figura 3-11: Flow cell components

In Figure 3-12 the PDMS device on the flow cell coverslip is shown.

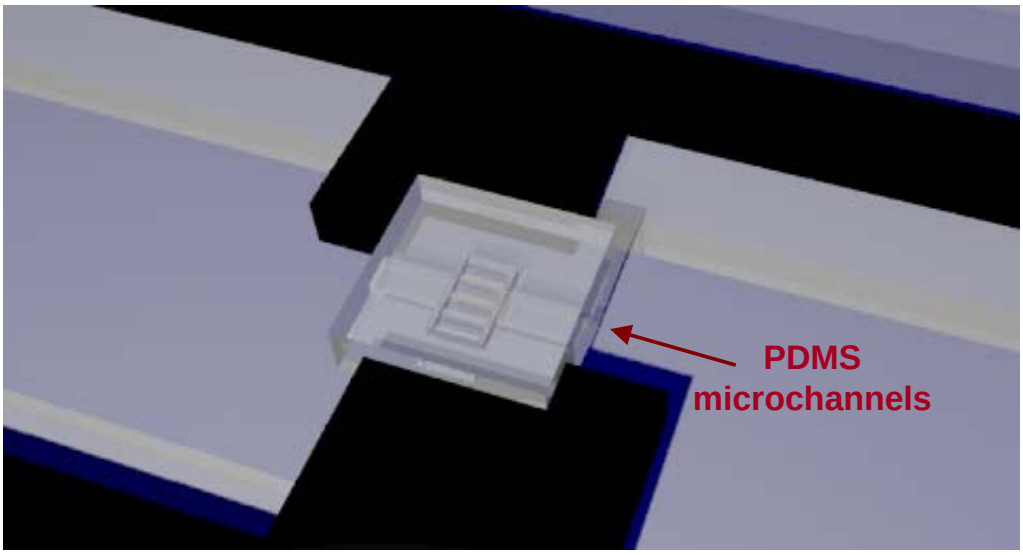

Figura 3-12: Detail of the flow cell - PDMS microdevice

3.2 RESULTS

The PDMS device contains two main network units arranged in parallel. Each network unit (Figure 3-13) consists of 4 microchannels of widths ranging from 100 to 10 μm. The starting channel is 300 μm in width and it presents a large bifurcation connected to the following two bifurcations: from here the channels narrow down, untill a width of 10 μm is reached. Channel depth was 5 μm throughout and the total lenght of the network is 3.5 mm.

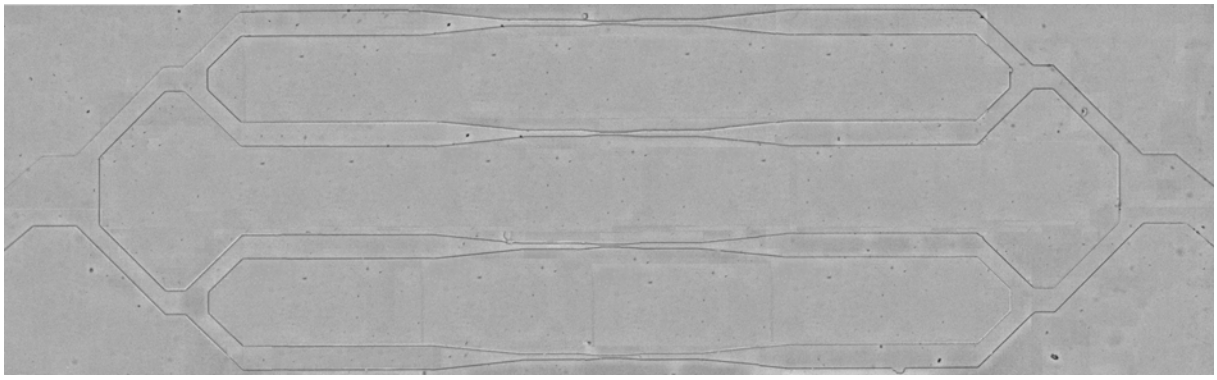

Figura 3-13: Network unit

3.2.1 Rectangular channel pressure flow

The microchannels cross-section is not circular as in the microcapillaries *in vivo*, but rectangular. For flow through rectangular channels, the flow parameters used in the previous capillary model are no longer valid. In this section, comparisons of the capillary and rectangular channel will be discussed. The pressure flow through the network is one important issue for evaluation of the PDMS device performance. To start, the pressure flow comparison, by using Eqs. (9) and (10), which represent flow rate through a single capillary and a rectangular channel, should be considered. The subscripts *tube* and *rec* represent the corresponding terms through a capillary and a rectangular channel, respectively.

$$Q_{tube} = \frac{\pi \Delta P R^4}{8 \eta L} \tag{9}$$

$$Q_{rec} = \frac{WH^3}{12\eta}\left(\frac{\Delta P}{L}\right)\left[1 - \frac{192H}{\pi^5 W}\sum_{i=1,3,..}^{\infty}\frac{1}{i^5}\tanh\left(\frac{i\pi W}{2H}\right)\right] \tag{10}$$

Eq.9 is the Poiseuille equation and is a physical law that describes slow viscous incompressible flow through a constant circular cross-section. Q is the volumetric flow rate, Δ*P* is the pressure drop across the tube, L and R are the length and the radius of the tube respectively and η is the dynamic viscosity. Eq.10, instead, is the Poiseuille equation adapted for rectangular channel. W and H are the width and the length of the channel, as shown in Figure 3-14.

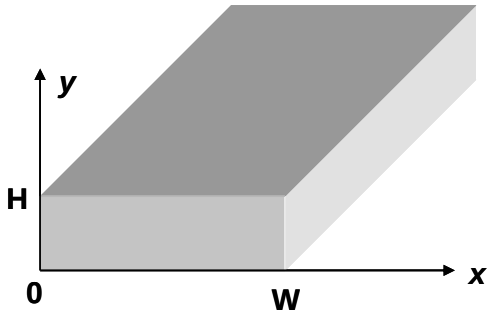

Figura 3-14: Rectangular channel geometry

To calculate the pressure drop across each different cross-section channel, the whole network was divided into ten different zones, depending on cross-section (Figure 3-15), and Eq.10 was used for each zone.

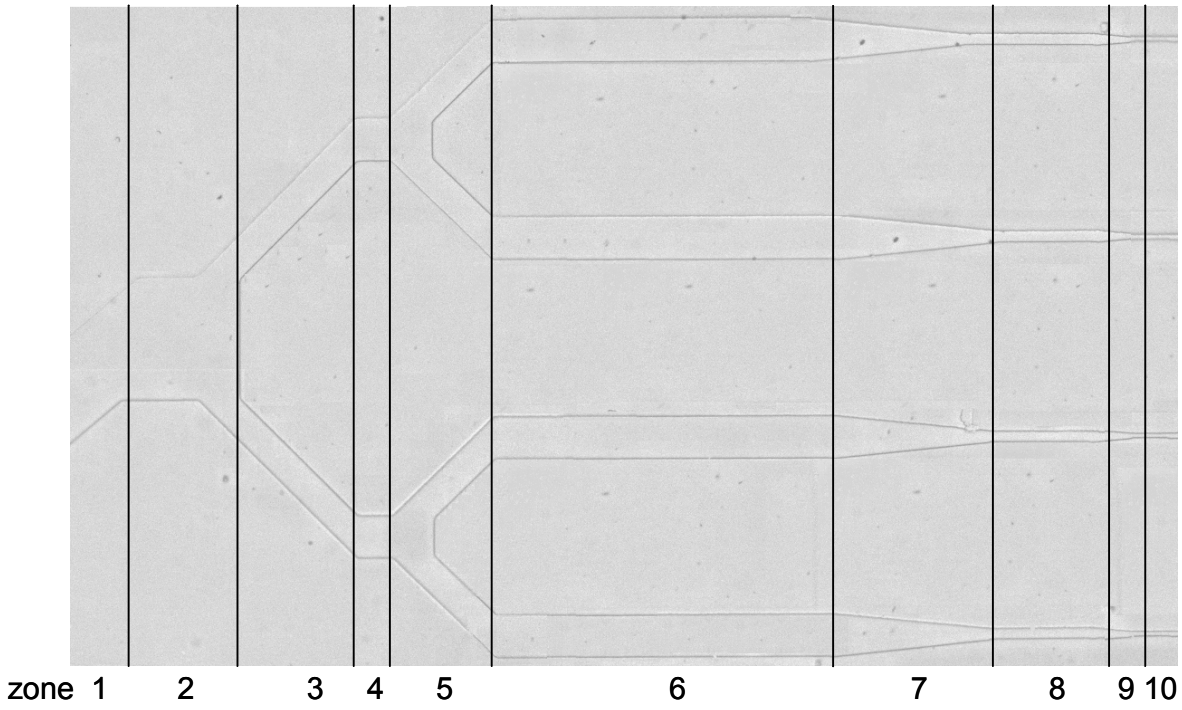

Figura 3-15: Network divided by zones under the same pressure drop

In particular, the velocity of a polystyrene microparticles (d=1 μm) along the centreline of a channel in the zone 8 (where W=25 μm) was measured: it was the maximum fluid velocity v_{max}. Dividing Eq.11 (at x=W/2 and y=H/2) by <v> as calculated from Eq.10, the ratio v_{max}/<v> was obtained (ΔP was the same in each equation and so was eliminated).

$$v_z(x,y) = \frac{\Delta P}{\mu L}\left\{\frac{y^2}{2} - \frac{yH}{2} + \frac{4H^2}{\pi^3}\sum_{i=1,3,..}^{\infty}\frac{\cosh[(i\pi/2H)(2x-W)]}{i^3\cosh(i\pi W/H)}\sin\left(\frac{i\pi y}{H}\right)\right\} \quad (11)$$

Then, by dividing v_{max} (measured) by v_{max}/<v> calculated, the mean flow velocity was known. In this way it was possible to calculate the flow rate Q_8 in a channel in the

zone 8. Once Q_8 was obtained, it was easy to calculate flow rates and then ΔP_i in each channel, just based on its geometry (as shown in Table 3-2). To know ΔP, ΔP_i was multiplied for the number of channel with the same cross-section in the whole geometry. The sum of ΔP is equal to the total pressure drop ΔP_{tot} imposed by the relative liquid levels in the entrance and the exit reservoir (in the case shown ΔP_{tot}=22.65 mmHg).

zone	Q, cm³/s	W, μm	L, μm	ΔPi, mmHg	ΔP, mmHg
1	2.341E-07	200	450	0.224	0.895
2	2.341E-07	300	250	0.082	0.329
3	1.171E-07	75	525	0.360	2.878
4	1.171E-07	100	100	0.051	0.406
5	5.853E-08	80	335	0.107	1.716
6	5.853E-08	100	750	0.190	3.043
7	5.853E-08	60	400	0.174	2.779
8	5.853E-08	25	300	0.346	5.533
9	5.853E-08	18	90	0.155	2.481
10	5.853E-08	10.6	45	0.162	2.589

Table 3-2: ΔP in dependence on cross-section

3.2.2 Comparison between capillary tubing and rectangular channel

To compare a circular with a rectangular cross-section the equivalent diameter D_{eq} was calculated. The D_{eq} is the diameter of a circular duct that gives the same pressure loss as an equivalent rectangular duct and it was calculated by using the classical Poiseuille law (Eq.9). In the smallest cross-section channel (zone 10) the equivalent diameter D_{eq} is 8.5 μm. In figure 3-16 RBC velocities both in cylindrical tubes and in microchannels are plotted as function of pressure drop.

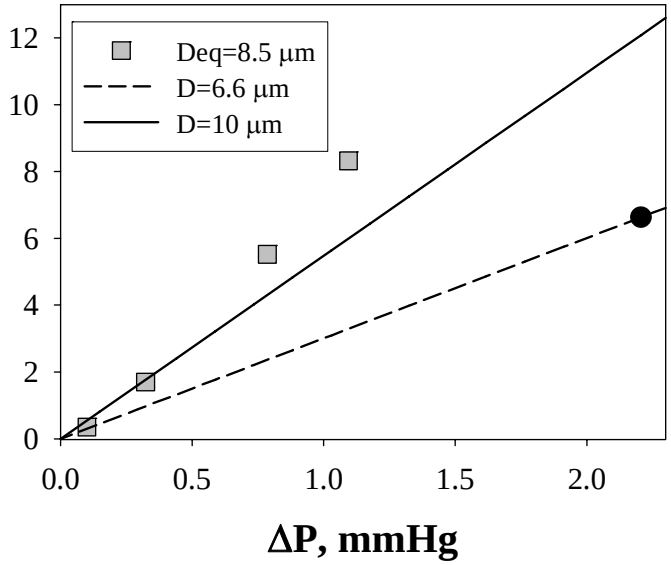

Figura 3-16: Comparison between RBC velocity in capillary tubes and in microchannels

The black dot represents an experimetal datum and the continuous and dashed lines are RBC velocities as extrapolated from experimental data for D=10 and 6.6 μm, respectively. Such extrapolation was needed because the pressure drops reached in microchannels are lower than those reached in experiments with microcapillaries. The cell velocity in rectangular channels is in good qualitative agreement with velocities in capillary tubes.

3.2.3 RBCs velocity in variable cross-section channels

RBC velocity is plotted as a function of position along the axis in Figure 3-18 for a divergent microchannel in very dilute cell suspensions (H_T = 0.5%) at a given value of ΔP_{tot}. The channel (Figure 3-17) may be divided into tre zones: 1) constant cross-section with W= 10.6 mμ and L=40 mμ; 2) variable croos-section, with W ranging from 10.6 mμ to 25 mμ with an angle= 0.09 rad, L=75 μm; 3) constant cross-section with W=25 μm and L=50 μm.

.

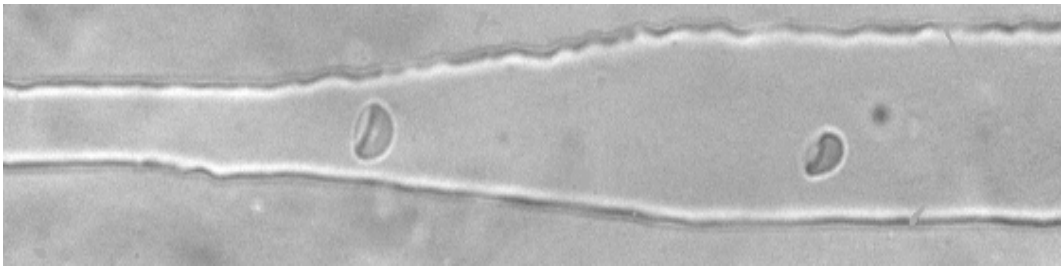

Figura 3-17: RBC flowing in a divergent microchannel

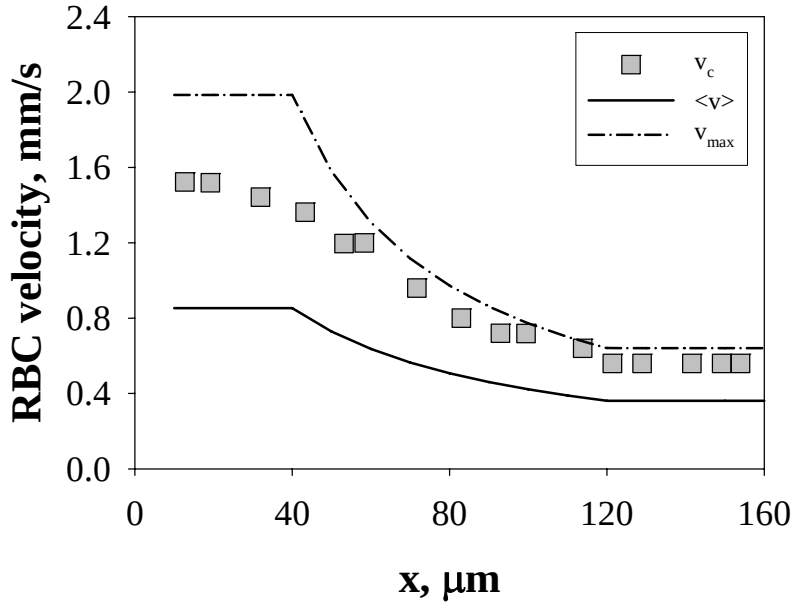

Figura 3-18: RBC velocity vs RBC position along the axis in a divergent microchannel

As expected, at the same pressure drop RBC velocity decreases with microchannel width. The continuous and dashed lines in Figure 3-18 correspond to the average and to the maximum suspending fluid velocity, respectively, as calculated from Eqs.

10 and 11. Thus, RBC velocity stays in between the average and maximum velocity of the suspending fluid. The ratio between RBC velocity v_c and v_{max} is shown in Figure 3-19, and is an increasing function of W. In fact, the higher is channel width, the closer is cell velocity to the maximum fluid velocity.

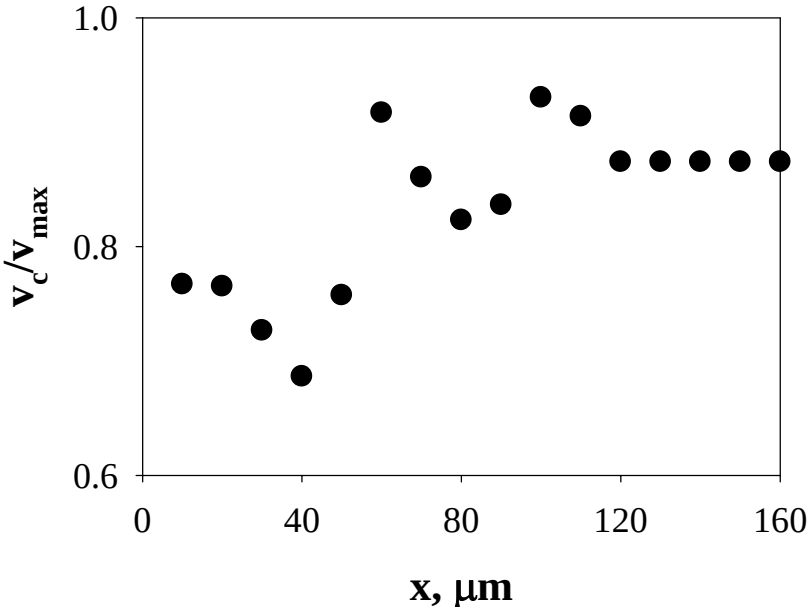

Figura 3-19: Ratio between RBC velocity and suspending fluid maximum velocity (as calculated from Eq.11)

In Figure 3-20 RBC velocity as a function of RBC position along the axis at different pressure drops is shown. Obviously, red blood cell velocity increases with ΔP_{tot}.

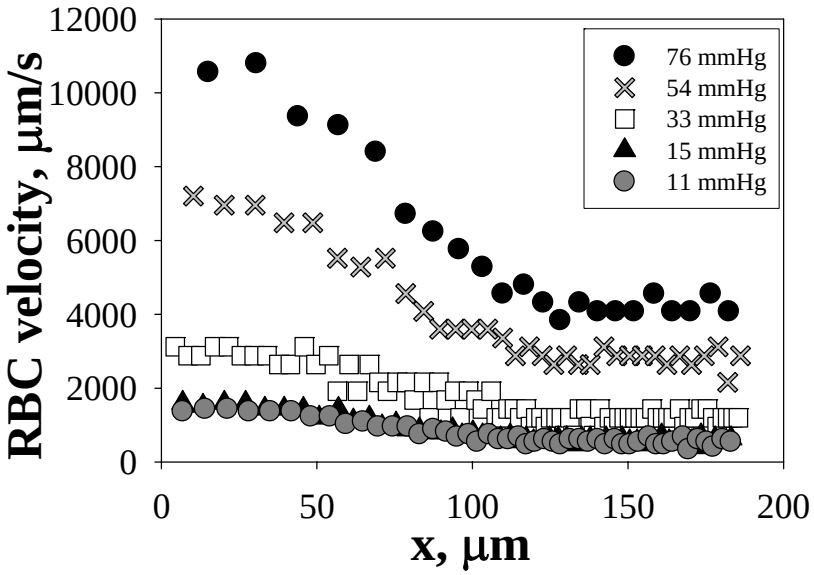

Figura 3-20: RBC velocity vs RBC position along the axis at different ΔP_{tot}

Equal and opposite behavior was found in convergent channel with equal dimensions, as shown in Figure 3-21. RBC velocity increases with channel width and with pressure drop.

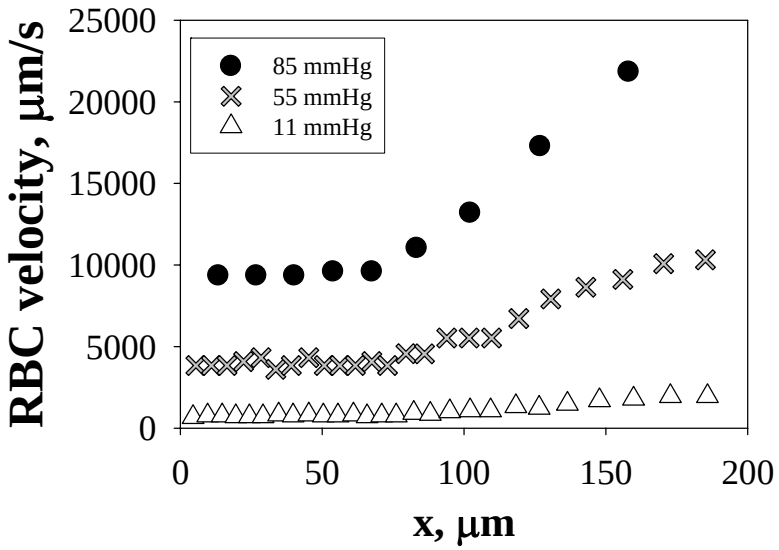

Figura 3-21: RBC velocity vs x at different ΔP_{tot}

3.2.4 Red blood cell shape recovery

Viscoelastic behavior of red cells is observed when the red cell flows through the divergent zone shown in Figure 3-17 and then reaches a stationary shape in the following constant section channel. As shown in Figure 3-22, the cell (and its membrane) recovers its shape in 0.05 s,. The time rate of recovery is related to the membrane elastic and viscous force resultants.

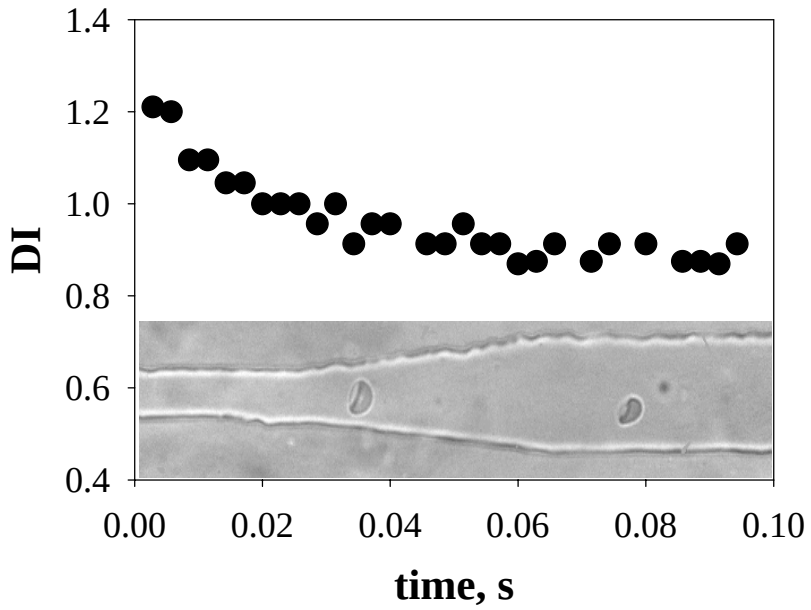

Figura 3-22: Plot of RBC deformation index as a function of time

Cell deformation index *DI* was measured as the ratio between the long and the short side of a bounding box enclosing the cell body. A decreasing trend is observed, with a leveling-off of cell *DI* at values of time around 0.05 s. Computed shapes are shown in Figure 3-23 at the beginning and the end of the divergent zone.

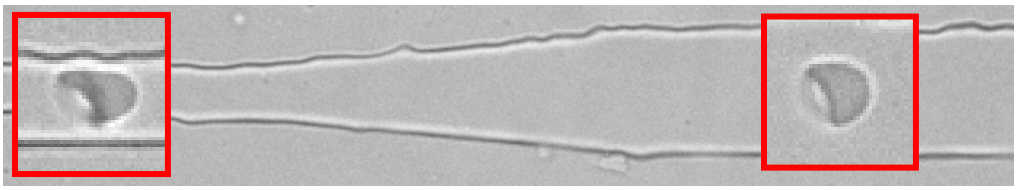

Figura 3-23: Images of RBCs in different section of the channel

In Figure 3-24 *DI* is plotted as function of RBC position along the axis: it is clear that *DI* decreases more and more when the red blood cell goes through the divergent zone and then reaches a plateau in the constant width region. Furthermore, *DI* increases with pressure drop.

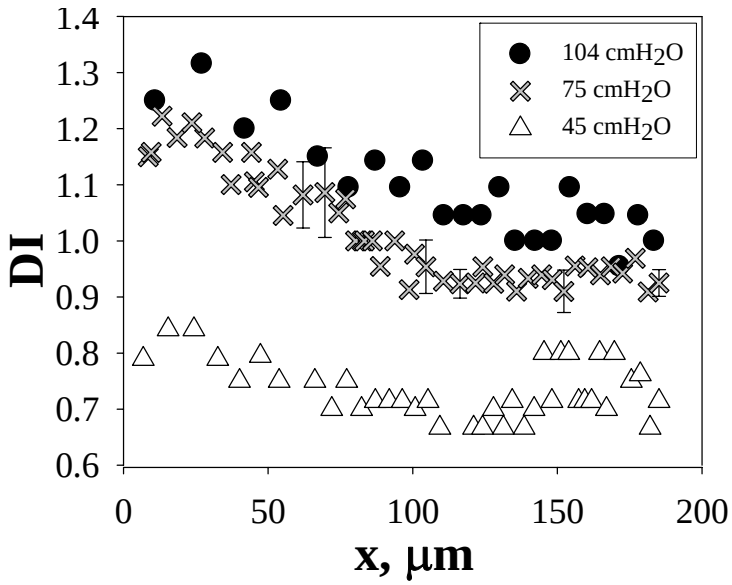

Figura 3-24: DI vs RBC position along the centreline at different pressure drop

In conclusion, the prototype microchannel network device described here is a new method of evaluating the effect of microvascular perfusion on RBC velocity and deformability by directly measuring the flow of blood through a microchannel network with realistic dimensions and architecture similar to real microcirculation.

Chapter 4 MODEL FLUIDS

4.1 MATERIALS AND METHODS

In this work the deformation of a Newtonian droplet in a Newtonian continuous liquid phase under microconfined flow both between two parallel plates and in a capillary was studied.

4.1.1 Materials

The system PB-PDMS is commonly used in the literature as a pair of immiscible Newtonian model fluids (Grizzuti, 1997; Minale, 1997, 1998; Vinckier 1998). Polybutene (PB), supplied by BP Chemicals under the trade names of Napvis or Indopol can be considered Newtonian for the range of applications considered in this work. The Silicone Oil was supplied by Dow Corning, and was also available in several grades. All the fluids were liquid and transparent at room temperature. The parallel plates experiments were carried out at fixed viscosity ratio of one (λ=1) and the fluids used were: a PolyButene liquid (Napvis 30) as the continuous phase, with a viscosity of 83 Pas at room temperature and negligible first normal stress difference and a mix of Newtonian Silicone Oils (PDMS Dow Corning, 20, 200, 1000, 20000, 60000, 100000 and 200000 cSt) of different molecular weight in such proportions to match the polybutene viscosity for the drop phase. The experiments in microcapillaries were carried out at two different values of the viscosity ratio: λ=1 and λ=4. The continuous phase was a PolyButene liquid (Indopol H7) and the drop phase was Silicon Oil 1000 for λ=4 experiments and a mix of Silicon Oils 20 and 200 for λ=1 experiments. In Table 4-1 name and properties of the fluids used are shown.

Material	**Density** (g/cm^3)	**Refraction index**	**Viscosity** (Pa s)
Silicon Oil 100000cSt	0.975	1,406	105
Silicon Oil 60000cSt	0,975	1,406	62.4
Mix SO100000cSt-SO60000cSt (57% SO100000cSt)	0,975	1,406	83.1
Napvis 30	0,8953	1,499	83.3
Indopol H7	0,95	1, 41	0.26
Silicon Oil 1000	0,975	1,406	1.03
Mix SO200cSt al 57%+ SO20 cSt	0,975	1,406	0.27

Table 4-1: Properties of the fluids at 23°C

4.1.2 Rheological characterisation

The viscosity of each polymer was measured with a cone and plate stress-controlled rheometer (Bohlin CVO120 with CP4/40 geometry) at 23°C.

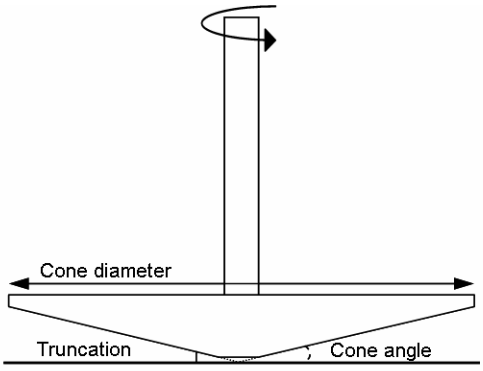

Figura 4-1: Cone and plate rheometer

Cone and plate measuring systems are usually referred to by the diameter and the cone angle. For instance a CP4/40 is a 40mm diameter cone having an angle of 4°. The cones are often truncated. These types of cones are positioned such that the theoretical (missing) tip would touch the lower plate. By removing the tip of the cone, a more robust measuring system is produced. This can be seen in Figure 4-1. The sample should just fill the gap between the upper and lower elements. If the sample is likely to shrink during the test (due to solvent loss, etc.) it is advisable to aim for a slight bulge as shown in Figure 4-2. If too much or too little sample is used, the torque produced will be incorrect leading to over- or under-estimated data, respectively.

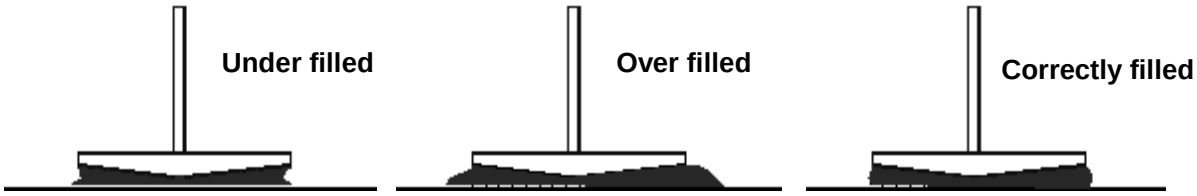

Figura 4-2: Sample loading for cone and plate measuring system

Both PolyButene and the Silicon Oil mix showed Newtonian behaviour in the shear rate range explored (0.01-100 s^{-1}). In Figure 4-3 the flow curve of a PDMS 100000 and 60000 mix at 90% of PDMS 100000 is plotted.

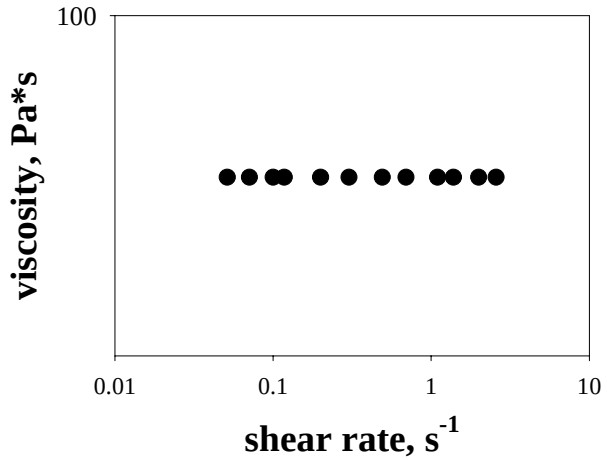

Figura 4-3: Viscosity vs shear rate of a PDMS 100000 and 60000 mix (90% PDMS 100000)at 23°C

4.2 EXPERIMENTAL APPARATUS

4.2.1 Flow cell

Three silica capillaries (Polymicro Technologies), with inner diameters = 319 μm were placed between two glass slides (50 mm x 50 mm x 1 mm) in a T-junction arrangement: the smallest one approaches the two others at right angle, but does not cross them, as shown in Figure 4-4.

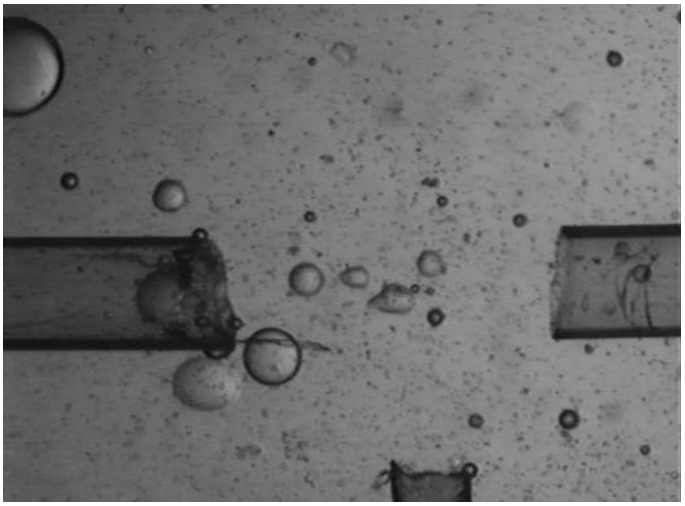

Figura 4-4: Capillaries set-up

The flow cell was placed on the motorized x-y stage of an transmitted light microscope (Axioscop FS, Zeiss), equipped with a B/W CCD video camera (KP-ME1, Hitachi) and a motorised focus system (LEP).

4.2.2 Flow generation in capillary

In Figure 4-5 injection af a drop inside the capillary is shown. The continuous and the drop phases were injected respectively into the capillary on the right and into the capillary on the bottom by using a syringe pump (11 plus, Harvard Apparatus). The pump flow rate can be changed from 0.0014 μl/hr to 26.56 ml/min; in this work flow rates from 0.1 to 1 ml/hr were used. The continuous phase, flowing continuosly from right to left, filled the space between the capillaries and reached the capillary on the left. From the capillary on the botom the drop phase was injected (Figure 4-5, t0) and a droplet was generated by Rayleigh instability (Figure 4-5, t1). The droplet was pushed by the right-to-left flow (Figure 4-5, t2) and moved into the left capillary (Figure 4-5, t3). When the drop is inside the left capillary, a constant flow rate was imposed and a Poiseuille flow was induced.

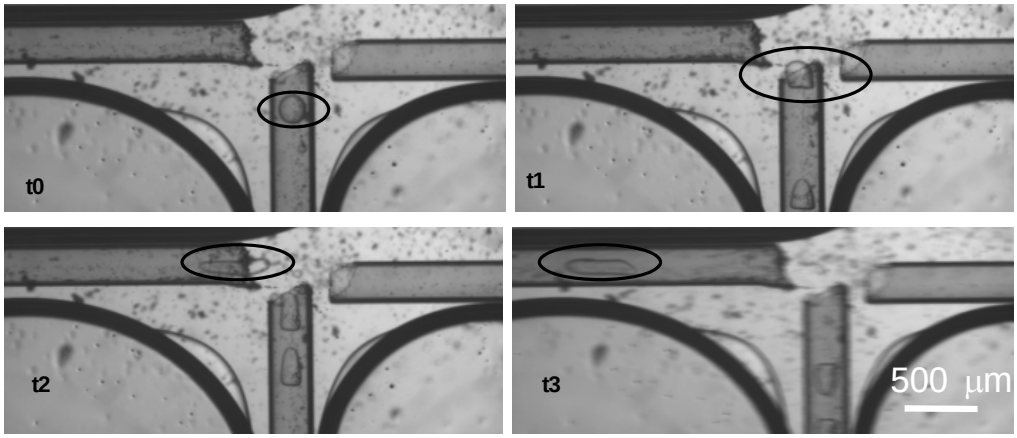

Figura 4-5: Flow generation in the capillary

Several different flow rate, that means different Capillary numbers, were analyzed. The large arrays of images recorded were processed off-line by a custom macro based the library of a commercial software package (Image Pro Plus 4.5) and allowing to isolate the subsets of images with drops passing through the field of view. Since there are no images of drops at rest, a Matlab routine was used to measure the drop diameter, by assuming a solid revolution shape for the drops. The volume was calculated from the deformed drop cross section.Then, by volume conservation and by assuming a spherical shape for droplets at rest, drop diameter was calculated.

4.3 MOTION OF DROPS THROUGH A TUBE

In this paragraph the pressure-driven transient motion of deformable drops through a cylindrical tube with inner diameter size close to droplet size will be analyzed.

4.3.1 Deformation of start-up

When a drop enters the capillary it deforms itself into an elongated shape and reaches slowly evolving quasi-steady shapes (images shown in Figure 4-5). In Figure 4-6 the behavior of the nondimensional drop axis $R_{MAX}/2a$ as a function of the nondimensional time *Vt/D* is shown, where V is the mean bulk velocity, t the experimental time and D the capillary diameter. When the drop enters the capillry (Vt/D=0) its shape is already elongated. To evaluate the behavior of the elongation whatever the injection, the flow was stopped (to allow drop relaxation) and then it was restarted.

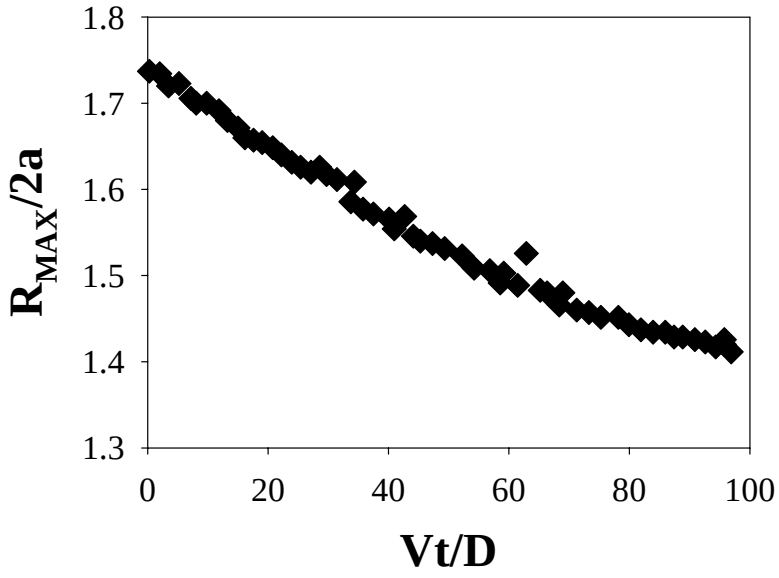

Figura 4-6: Transient drop deformation from the entrance of the capillary

In Figure 4-7 the nondimensional drop axis $R_{MAX}/2a$ as a function of the nondimensional time *Vt/D* is plotted, holding K and Ca constant. $R_{MAX}/2a$ increases with Vt/D since a constant value is reached.

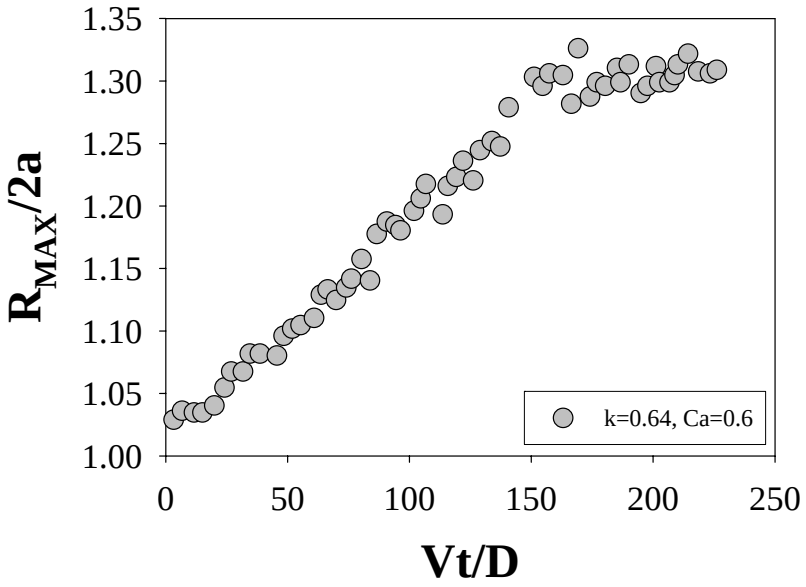

Figura 4-7: Transient drop deformation from static conditions

In Figure 4-8 and 4-9 $R_{MAX}/2a$ as a function of *Vt/D* at different k and at different Ca respectively are plotted: in both cases, as k increases, Vt/D increases too. In particular, in Figure 4-8, at k>1 and Vt/D=0 the value of $R_{MAX}/2a$ is not one: this is due to droplet size. Because the droplet radius is bigger than the tube radius, it does not have a spherical shape ($R_{MAX}/2a \neq 1$).

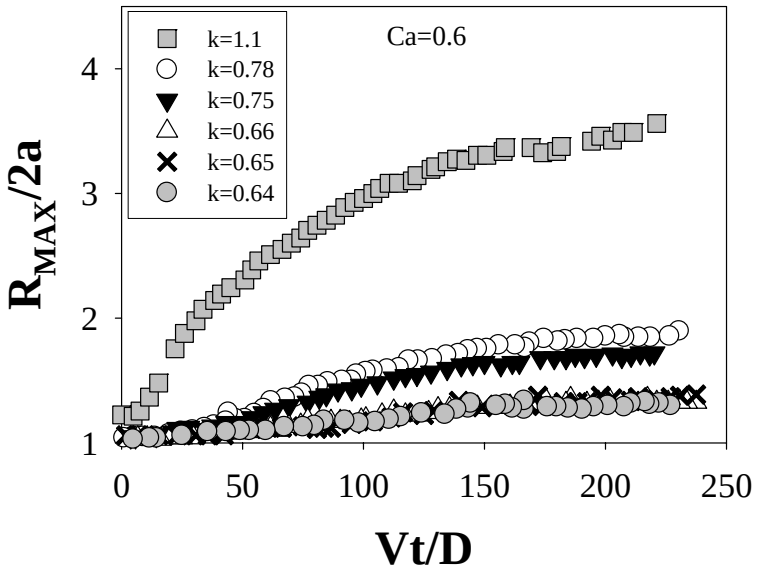

Figura 4-8: Comparison between transient drop deformation at Ca=0.6 and different k

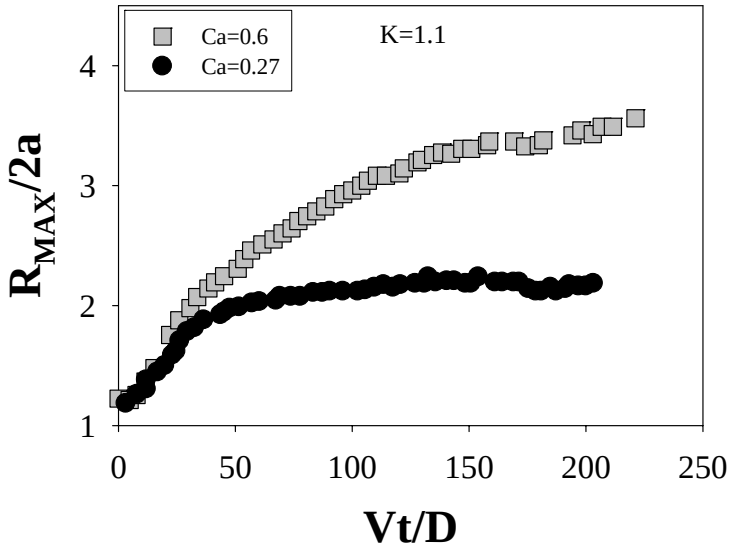

Figura 4-9: Comparison between transient drop deformation at k=1.1 and different Ca

Let's look now at the behavior of the transient for a droplet that is not along the tube axis but close to the tube wall (Figura 4-10).

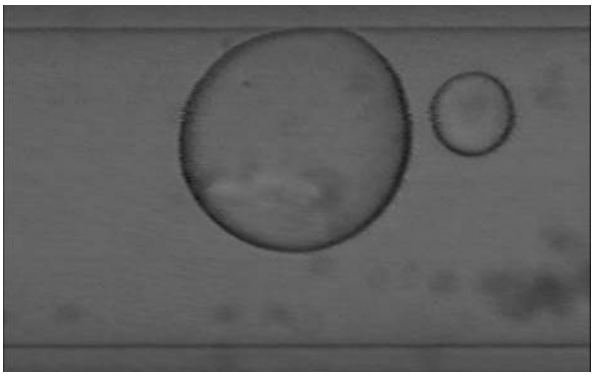

Figura 4-10: Droplt near the wall tube

As flow restarts, the drop migrates from the tube wall radially towards the centreline.

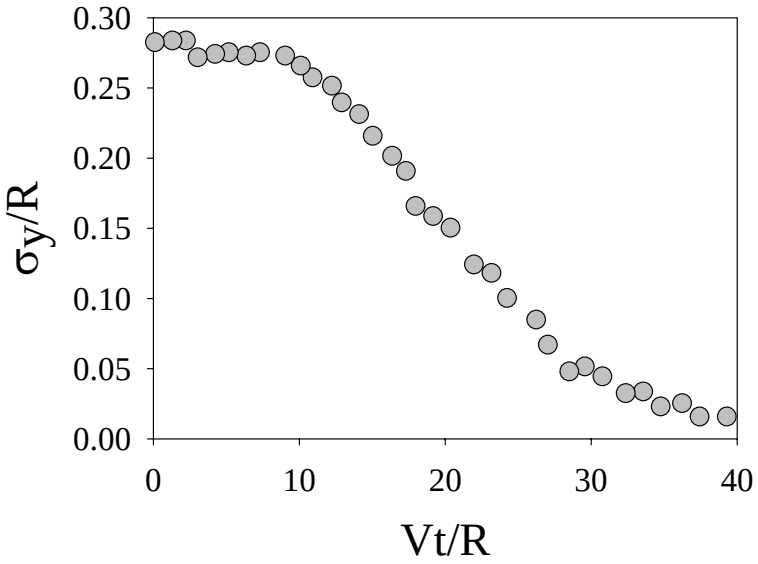

Figura 4-11: Drop alignement along the centreline

To understand this phenomenon better, in Figure 4-11 the distance from the centreline of the drop centre normalized with the drop radius ($\sigma y/R$) is shown as function of the nondimensional time. Then, in Figure 4-12 $R_{MAX}/2a$ versus Vt/D for this droplet is plotted. An initial overshoot due to the separation of the droplet from the tube wall is observed, followed by an undershoot due to alignment of the drop with the centreline.

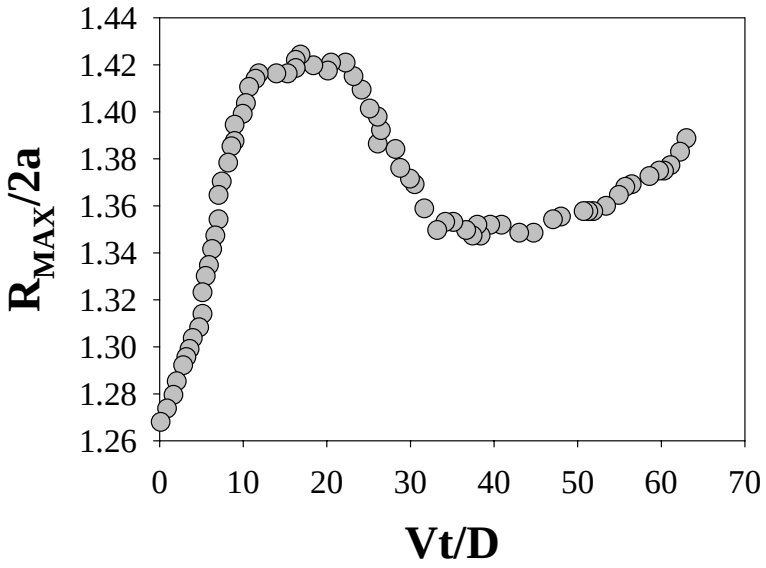

Figura 4-12: Transient drop deformation for a drop that starts far away from the centreline

4.3.2 Drop morphology

When the drops are sufficiently large and the capillary number is high the drops assume a slipper shape. In Figure 4-13 equilibrium drop shapes for increasing values of k (from top to bottom) and for increasing values of Ca (from left to right) are shown. It is evident that drops become more elongated (in the direction of motion) as Ca and k increase. Upon increasing the capillary number at sufficiently high values (in this case, due to experimetal limits, the steady-state was not reached) an evolving dimple may develop at the rear of the drops (Figure 4-14). A similar slipper shape has been observed in red blood cells. It should be pointed out, however, that the drops develop a slipper-like shape only when the capillary number is high enough, whereas the red blood cells appear to do so always, as long as the tube radius is sufficiently small.

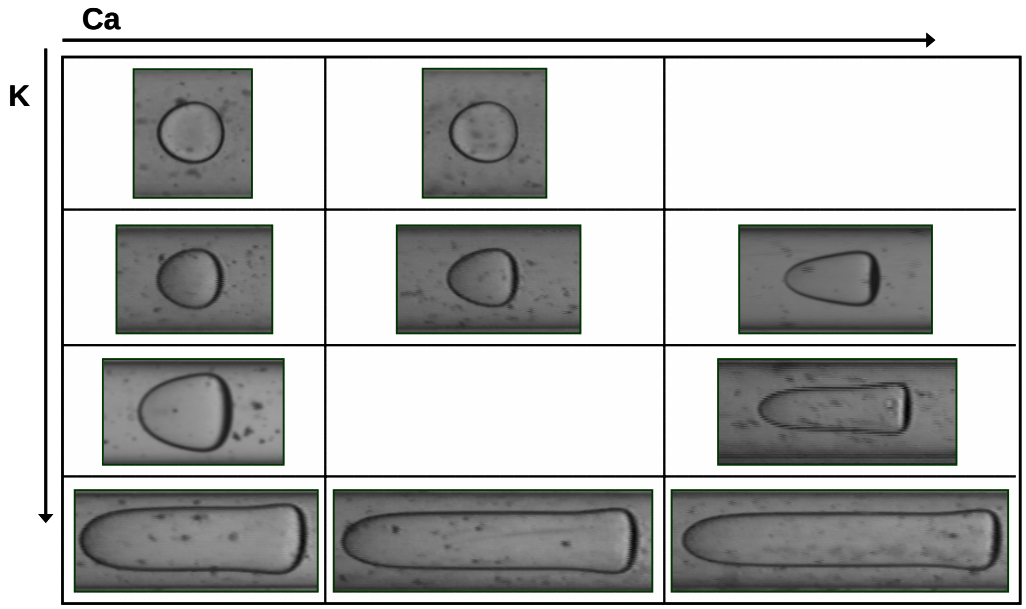

Figura 4-13: Equilibrium drop shapes for increasing values of k (from top to bottom) and for increasing values of Ca (from left to right)

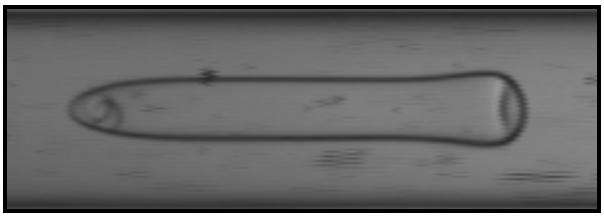

Figura 4-14: Transient drop shapes at high values of Ca

A quantitative representation of this trend is displayed in Figure 4-15, where the slightest distance between drop and tube wall (δ_{MIN}) normalized with R is plotted as function of k, at three different Capillary number. For each Ca, δ_{MIN} decreases with K and reach a plateau when k=1. Furthermore, δ_{MIN} increases with Ca, and this confirms that the drop becomes thinner and thinner as flow rate increases. At low values of k, the effect of Ca is less definite, as shown in morphological analysis.

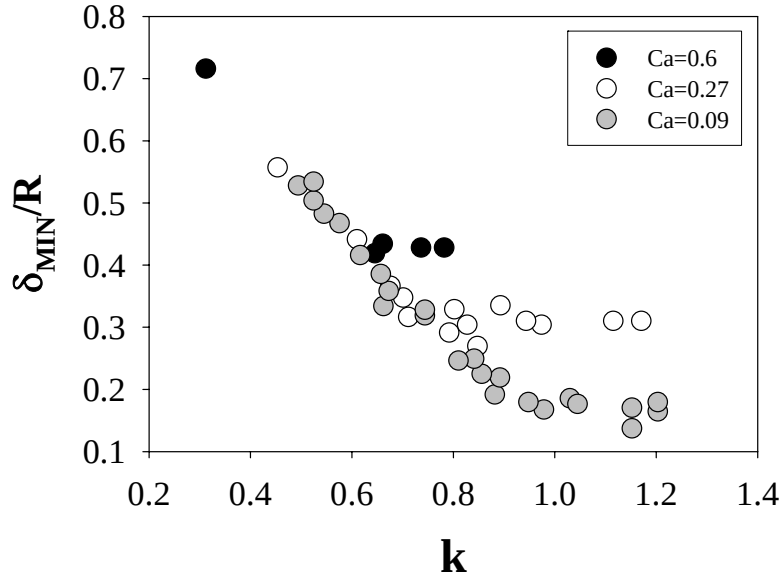

Figura 4-15: δ_{MIN}/R vs k at different Ca

The maximum drop length at steady-state, normalized with drop diameter, $L_{MAX}/2a$ is plotted as a function of k at the same Capillary number then previously in Figure 4-16. An increment both in k and in Ca corresponds to drop elongation.

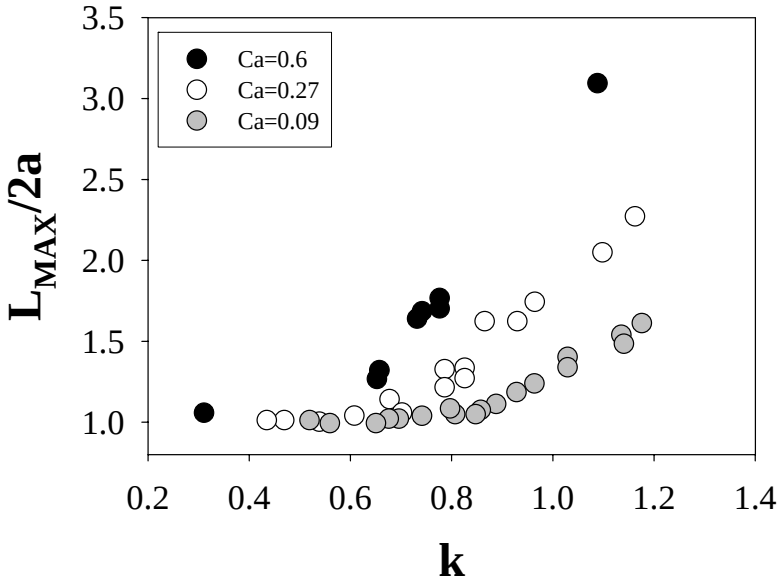

Figura 4-16: $L_{MAX}/2R$ vs k at different Ca

Finally, in Figure 4-17 the ratio between drop velocity *U* and the average suspending fluid velocity *V* as calculated from Poiseuille tube flow is shown as a function of k. As expected, at the same k drop velocity *U* increases with Capillary number. At each Ca *U/V* approaches a plateau value; thus, drop velocity stays in between the average and maximum velocity of the suspending fluid, the latter being twice the former in Poiseuille tube flow.
All the data reported on in this paragraph correspond to experiments carried out at λ=1. Data at λ=4 display a similar behavior, but they are not shown for the sake of brevity.

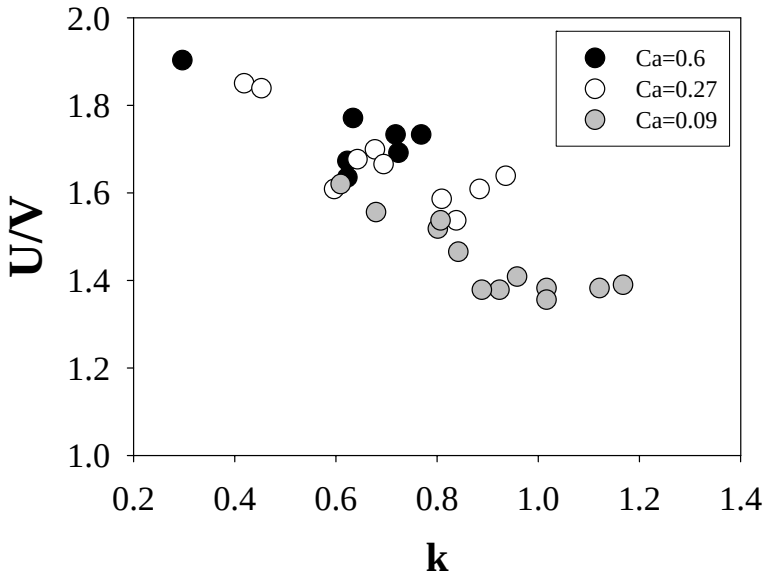

Figura 4-17: U/V vs k at different Ca

4.3.3 Streamlines

The advantage of working on a model fluid is the possibility of using dimensions which are 1-2 order of magnitude bigger than for red blood cells. For example, in order to obtain a more detailed view of the dynamics of red bllod cell motion in microcapillaries, in this work a series of flow-visualization studies on droplet motion was made, based upon stremlines pictures taken by addition of polystirene microparticles into the capillaries. To evaluate the motion around a single drop, between droplets flowing in a train and inside droplets, 2 μm polystirene particles were used.

In Figure 4-18 the motion around an isolated drop is shown. It is clear that particles flowing in the rear zone of the drop close to the centreline approach the drop surface, because of their higher velocity. When they arrive close to the droplet, their velocity decreases and they are displaced to another position along capillary radius. At this point there is an inversion of the relative motion between drop and particles, which start to flow in the opposite direction.

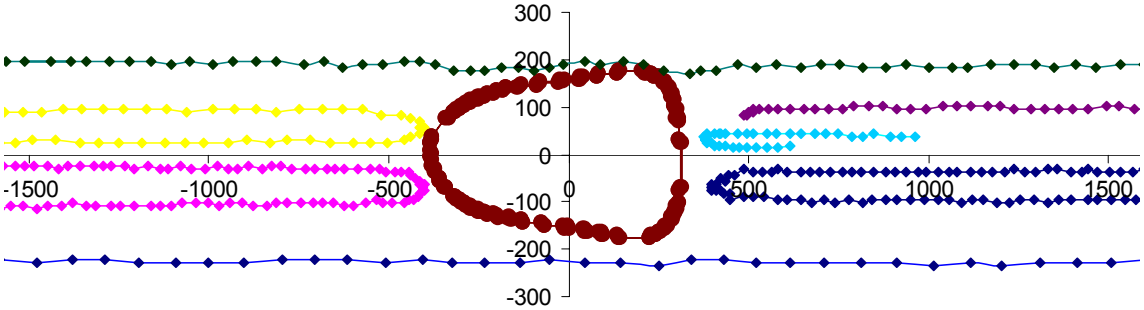

Figura 4-18: Streamlines around a single drop

A quantitative representation of this behavior is shown in Figure 4-19, where the relative fluid/particle velocity with respect to drop velocity is plotted as function of the relative position.

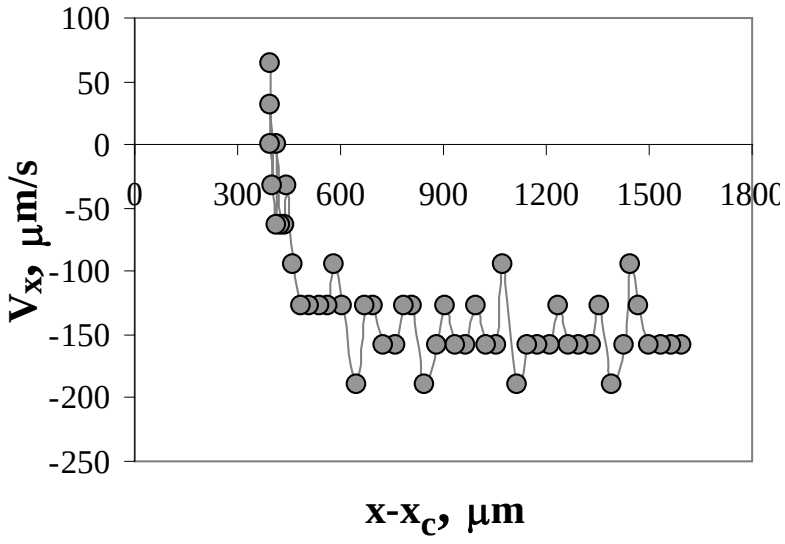

Figura 4-19: Effect of drop on fluid motion

Let's analyze the flow field in a train of drops (Figure 4-20).

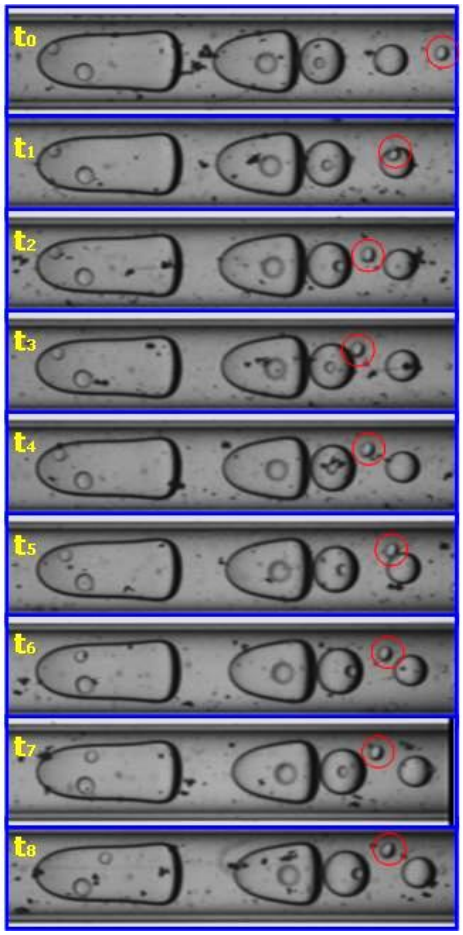

Figura 4-20: Effect of drop on fluid motion

The small droplet underlined with a red circle moves from a drop-free zone (on the right, time t0) to a zone between two larger drops. In this area a ricirculation of fluid is observed, where the small droplet is trapped, as shown in Figure 4-21.

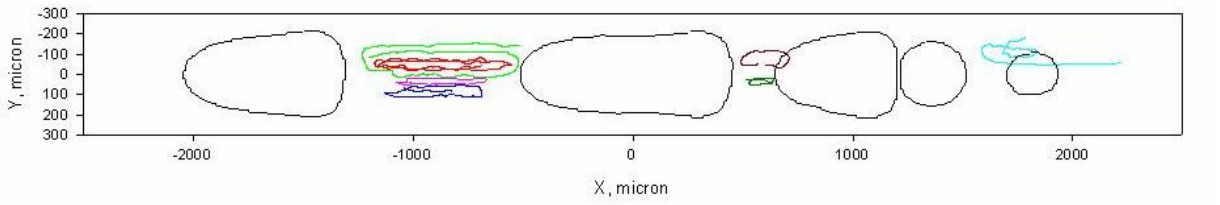

Figura 4-21: Recirculation zones between drops

Concerning the flow field inside the drops, at low values of k (k<0.7) a counterclockwise eddy develops in the drop interiors. In Figure 4-22 theoretical prediction (top) and experimental data (bottom) are shown. The centre of the eddy inside the drops at centreline nearly coincides with the drop centroid, but the centre of the eddy for drops not at the centreline is located closer to the wall. The experimetal data are in good agreement with predictions of the numerical simulation by Coulliette and Pozrikidis (1998) for L/R=2, σ/R=0.5, Ca=0.1, and a/R=0.1 and 0.4. Model calculations are based on a numerical solutions of the equations of Stokes flow obtained by the boundary-integral method.

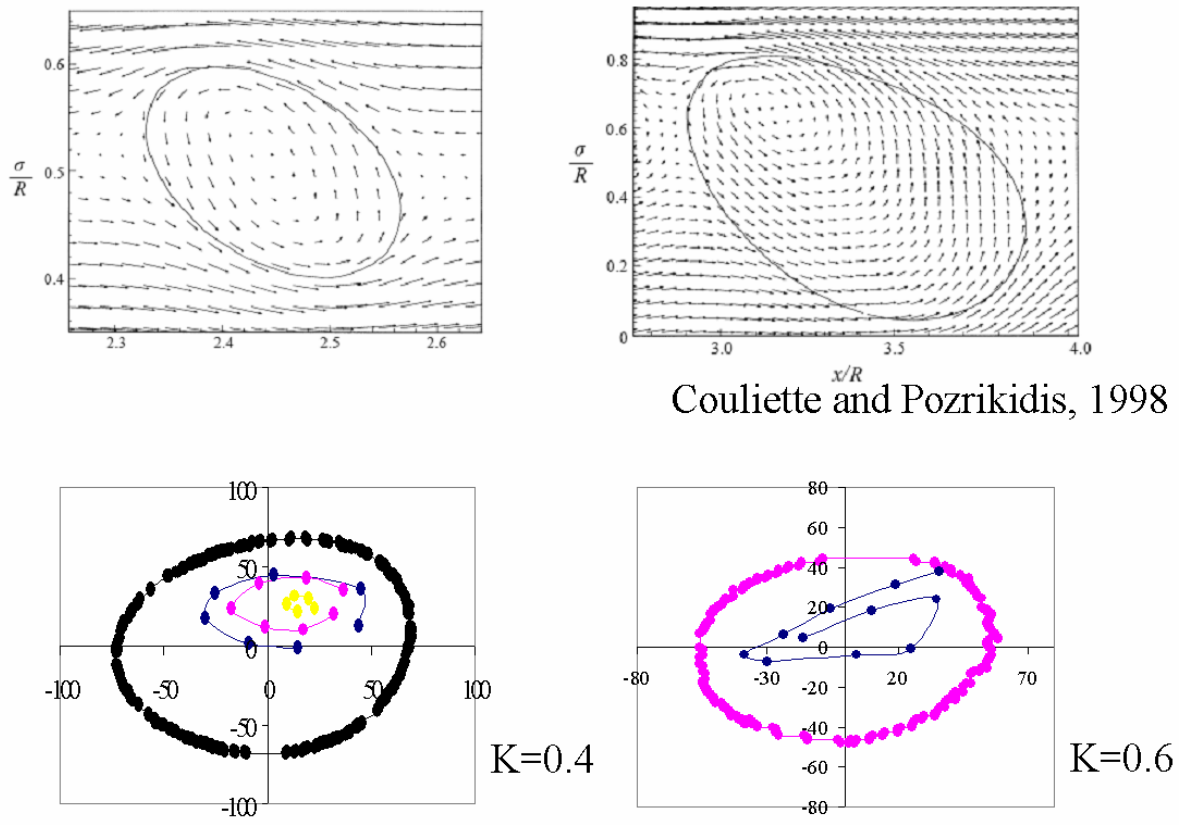

Figura 4-22: Comparison between experimental data and the predictions of Couliette and Pozrikidis for flow field interior to a drop

When k>0 the slower moving fluid near the tube wall transmits strong shear stresses across the interface and causes the presence of two eddies in the interior, at the rear of the drop. Some images and a quantitative representation of this trend are shown in Figure 4-23.

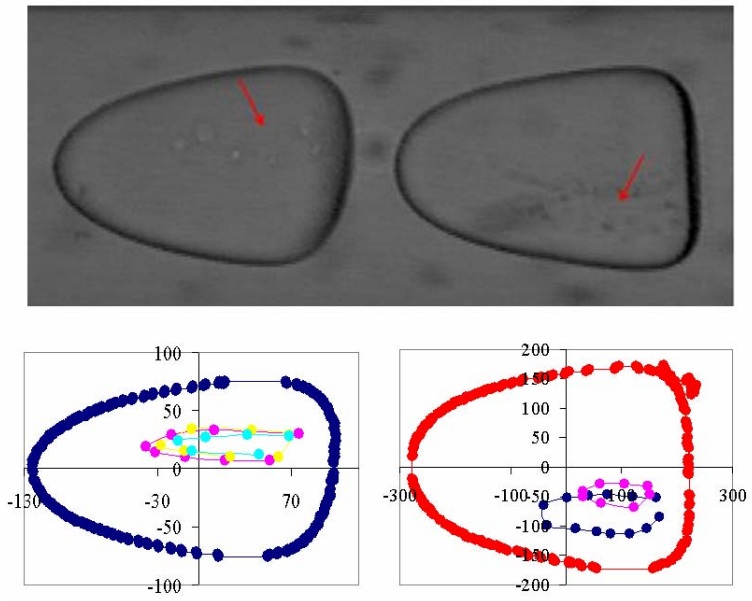

Figura 4-23: Images and quantitative representation of flow field inside a drop at k>0.7

Furthermore, a stagnant zone at the drop tip was founded (as shown in Figure 4-24).

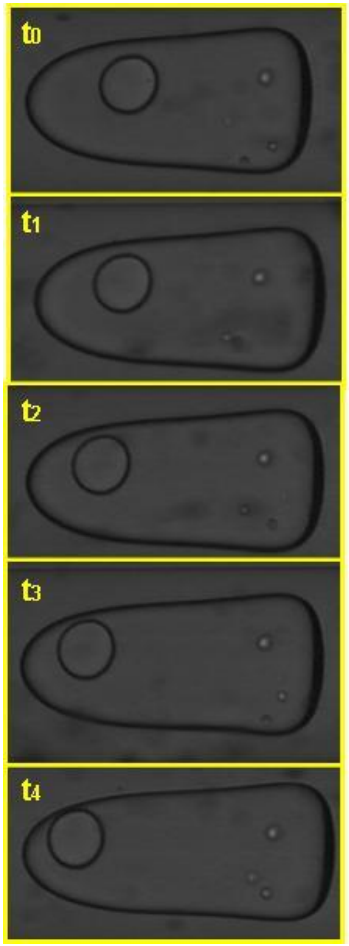

Figura 4-24: Stagnant zone at the drop tip

These data are in good agreement and, for the first time, support the numerical simulation by Martinez and Udell (1989); an image calculated from their model at k~1 by is shown in Figure 4-25.

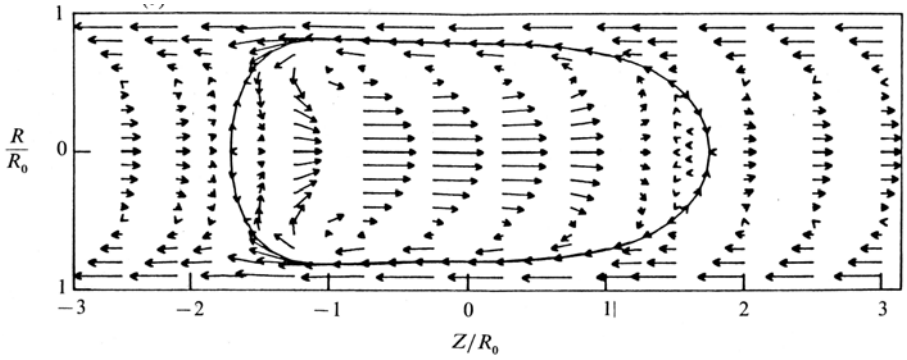

Figura 4-25: Flow field at k~1 by the model of Martinez and Udell (1989)

In conclusion, with reference to the goal of this work, that is to study a model fluid to simulate rheological and fluidodynamic behavior of blood, it is important to underline that the presence of recirculation zones, both around and inside the drops, is also found in the flow of red blood cells.

Chapter 5 Conclusions

The main purpose of this work is to study blood flow in confined geometries in order to develop a blood analog mimicking the rheological and fluidodynamic behavior of blood. Three different kinds of experiments were performed, and the main conclusions from each experiment are presented in the following.

1. An experimental methodology to investigate the deformability of RBCs flowing in microcapillaries having diameter close to the average cell size was developed. The microcapillaries are placed in a flow cell, where a suspension of RBCs is fed under the action of a liquid head in the physiological range. Video microscopy images of the flowing RBCs are acquired at high magnification and later processed by an automated image analysis macro. It was found that RBCs from healthy donors exhibit the classical parachute shape observed *in vivo*. Furthermore, for the first time a thorough quantitative comparison with theoretical predictions from the literature was provided, and a good agreement with no adjustable parameters was found.

2) A novel tool for evaluating the impact of impaired deformability of RBCs on the flow of blood in the microvasculature by directly measuring perfusion of a test microchannel network with dimensions and topology similar to the real microcirculation was presented. The measurement of microchannel network perfusion was compared with RBC flow in capillaries tubing. The direct measurement of microchannel network perfusion represents a new concept for the field of blood rheology and should prove beneficial for basic science and clinical applications.

3) An analysis of the flow of deformable droplets of one Newtonian fluid suspended in another Newtonian fluid was presented. Both a precision sliding plate apparatus and glass microcapillaries were used. The shapes of the liquid drops are similar to the morphology of red blood cells that have been observed in narrow glass capillaries as well as in blood vessels.

BIBLIOGRAPHY

1) M. Abkarian, M. Faivre and H.A. Stone, “High-speed microfluidic differential manometer for cellular-scale hydrodynamics”, *PNAS*, **103**;538-542, (2006)

2) K.H. Albrecht, P. Gaehtgens, A. Pries, “The Fahraeus Effect in Narrow Capillaries”, *Microvascular Research*, **18**, 33-47, (1979)

3) C. Alonso, A.R. Pries, P. Gaehtgens, “Time-dependent rheological behaviour of blood flow at low shear in narrow horizontal tubes”, *Biorheology*, **26**; 229-246, (1989)

4) R. Bali, S. Mishra, S. Dubey, “A mathematical model for red cell motion in narrow capillary surrounded by tissue”, Applied mathematics and computation”, (2007)

5) O.K. Baskurt, H.J. Meiselman, “Blood Rheology and Hemodynamics”, *Seminars in Thrombosis and Hemostasis*, **29**(5), 435- 447 (2003)

6) A. Borhan and J. Pallinti, “Pressure Driven Motion of Drops and Bubbles through Cylindrical Capillaries: Effect of Buoyancy”, *Ind. Eng. Chem. Res*., **37**, 3748-3759 (1998)

7) G. Bugliarello and J.W.Hayden, “Detailed characteristic of the flow of blood in vitro”, *Transaction of the Society of Rheolog*y, **VII**, 209-230, (1963)

8) A. Bunyaratvej, P. Butthep, N. Sae-Ung, S. Fucharoen and Y. Yuthavong, “Reduced deformability of thalassemic erythrocytes and erythrocytes with abnormal hemoglobins and relation with susceptibility to *Plasmodium falciparum* invasion”, *Blood*, **79**(9), 2460-2463, (1992)

9) S. Chien, Kuo-Li P. Sung, R. Skalak, S. Usami and A. Thzeren, “Theoretical and experimental studies on viscoelastic properties of erythrocyte membrane“, *Biophysical Journal*, **24**, 463-487, (1978)

10) C. Coulliette, C. Pozrikidis, “Motion of an array of drops through a cylindrical tube”, *Journal of Fluid Mechanics,* **358**, (1998)

11) P. D’Angelo, M. Barra, S. Guido, G.Tomaiuolo, A. Cassinese, “An electric criterion to evaluate glass transition temperature: dielectric relaxation measurements”, Macromole*cular Symposia*, **247**, 43-49, (2007)

12) R.A De Bruijn, “Deformation and breakup of drops in simple scorrimento flows”*, Ph.D. thesis, Eindhoven University of Technology*, (1989)

13) W. Dzwinel, K. Boryczko, and D.A. Yuen, “A discrete-particle model of blood dynamics in capillary vessels”, *Journal of colloid and interface science*”, 258, 163-173, (2003)

14) M. Faivre, M. Abkarian, K. Bickraj and H. A. Stone, “Geometrical focusing of cells in a microfluidic device: An approach to separate blood plasma”, *Biorheology*, **43**, 147-159, (2006)

15) J.M. Fitz-Gerald, “Mechanics of Red-Cell Motion through Very Narrow Capillaries”, *Proceedings of the Royal Society of London, Series B, Biological Sciences*, **174** (1035), 193-227, (1969)

16) R.W. Flumerfelt, “Drop breakup in simple scorrimento fields of viscoelastic fluids”, *Industrial and Engineering Chemistry, Fundamentals*, **11(3)**, 312-318, (1972)

17) E. Fukada, G.V.F. Seamen, D.Liepsch, M. Lee, L. Friis-Baastad, “Blood modeling using polystyrene microspheres”, *Biorheology*, 26, 401-413, (1989)

18) P. Gaehtgens, C.Duhrssen and K.H. Albrecht, “Motion, deformation and interaction of blood cells and plasma during flow through narrow capillary tubes”, *Blood Cells*, **6**, 799-812, (1980)

19) P. Gaehtgens, H. Schmid-Schönbein, “Mechanism of adaptation of mammalian erythrocytes”, *Natuewissenschaften*, **69**, 294-296, (1982)

20) F. Gauthier, H. Goldsmith, S.G. Mason, “Particle motions in non-newtonian media II: Poiseuille flow”, *Trans. Soc. Rheology*, **15**, 297-330 (1971)

21) CS. Gifford, M.G. Frank, J. Derganc, C. Gabel, R.H. Austin, T. Yoshida, M.W. Bitensky, *Biophys. J.* **84,** 623-633, (2003)

22) S. Guido, M. Simeone, A. Alfani, “Interfacial tension of aqueous mixtures of Na-caseinate and Na-alginate by drop deformation in scorrimento flow”, *Carbohydrate polymers*, (2001)

23) S. Guido, M. Villone, “Three dimensional shape of a drop under simple scorrimento flow”, *Journal of Rheology*, **42**, 395-415, (1998)

24) S. Henon, G. Lenormand, A. Richert and F. Gallet, “A new determination of the shear modulus of the human erythrocyte membrane using optical tweezers”, Biophysical Journal, 76, 1145-1151, (1999)

25) G. Hetsroni, S. Haber, E. Wacholder, “ The flow fields in and around a droplet moving axially within a tube”, *Journal of Fluid Mechanics,* **41**, (1970)

26) E. Hinch, A. Acrivos, “Long slender drops in a simple scorrimento flow”, *Journal of fluid mechanics*, **98 (2)**, 305-328, (1980)

27) B.P. Ho, L. G. Leal, “The creeping motion of liquid drops through a circular tube of comparable diameter”, *Journal of Fluid Mechanics,* **71**, (1975)

28) R.M Hochmuth, R.N. Marple, S.P. Sutera, “Erythrocyte Deformation in Glass Capillaries”, *Microvascular Research*, **2**, 409-419, (1970)

29) R.M. Hochmuth, P.R. Worthy, E.A. Evans, “Red cell extensional recovery and the determination of membrane vscosity”, *Biophysic Journal*, **26**, 101-114, (1979)

30) R. Hoffman, E.J. Benz, S.J. Shattil, B. Furie, H.J. Cohen, L.E. Silberstein, P. McGlave, “Hematology: Text with Continually Updated Online Reference”, Churchill Livingstone, (2004)

31) J.M.H. Janssen, “Dynamics of liquid-liquid mixing”, *Ph.D. thesis, Eindhoven University of Technology*, (1993)

32) K.L. Lin, L. Lopez and J.D. Hellums, “Blood Flow in Capillaries”, *Microvascular Research*, **5**, 7-19, (1973)

33) P.S. Lingard, “Capillary Pore Rheology of Erythrocytes. I. Hydroelastic Behaviour of Human Erythrocytes”, *Microvascular Research*, **8**, 53-63, (1974)

34) P.S. Lingard, “Capillary Pore Rheology of Erythrocytes. V. The Glass Capillary Array - Effect of Velocity and Haematocrit in Long Bore Tubes”, *Microvascular Research*, **17**, 272-289, (1979)

35) G. Mchedlishvili and N. Maeda, “Blood flow structure to red cell flow: a determinant of blood fluidity in narrow microvessels”, *Japanese Journal of Physiology*, **51**, 19-30, (2001)

36) N. Mohandas, P.G. Gallagher, “Red cell membrane: past, present, and future”, *Blood*, **112**, 3939-3948, (2008)

37) W.L. Olbricht, D.M. Kung, “ The deformation of liquid drops in low Reynolds number flow trough a capillary”, *Physics of fluids*, **4**, (1992)

38) R. Pal, “Rheology of concentrated suspensions of deformable elastic particles such as human erythrocytes”, *Journal of Biomechanics*, **36**, 981–989, (2003)

39) T.C. Pearson, R.R.C. Path, “Hemorheology in the Erythrocytoses”, *The Mount Sinai Journal of Medicine*, **68**(3), 182-191, (2001)

40) A.S. Popel, P.C. Johnson, “Microcirculation and hemorheology”, *Annu. Rev. Fluid Mech*., **37**, 43–69, (2005)

41) C. Pozrikidis, “Axisymmetric motion of a file of red blood cells through capillaries”, *Physics of fluids*, **17**, (2005)

42) A.R. Pries, T.W. Secomb, P. Gaehtgens, “Biophysical aspects of blood flow in the microvasculature”, *Cardiovascular Research*, **32**, 654-667, (1996)

43) J. Rallison, “The deformation of small viscous drops and bubbles in scorrimento flows”, *Annual Review of Fluid Mechanics*, **16**, 45-66, (1984)

44) A.I. Schafer, “Molecular basis of the diagnosis and treatment of polycythemia vera and essential thrombocythemia”, *Blood*, **107**(11), 4214-4222, (2006)

45) S.L Schreier, E.A. Rachmilewitz, N. Mohandas, “Cellular and membrane properties of alpha and beta thalassemic erythrocytes are different: Implications for differences in clinical manifestations”, *Blood*, **74**, 2194-2202, (1989)

46) T.W. Secomb, “Flow-dependent rheological properties of blood in capillaries”, *Microvascualr Research*, **34**, 46-58, (1987)

47) T.W. Secomb, “Red blood cell mechanics and capillary blood rheology”, *Cell Biophysics*, 231-251, (1992)

48) T.W. Secomb, R.Hsu and A.R. Pries, “A model for red blood cell motion in glycocalyx-lined capillaries”, *American Journal of Physiology,* **274**, H1016-H1022, (1998)

49) T.W. Secomb, R.Hsu and A.R. Pries, “Blood Flow and Red Blood Cell Deformation in Nonuniform Capillaries: Effects of the Endothelial Surface Layer”, *Microcirculation*, **9**, 189, 196, (2002)

50) T.W. Secomb, N. Özkaya, J.F. Gross, “Flow of axisymmetric red blood cells in narrow capillaries”, *Journal of Fluid Mechanics,* **163**, 405-423, (1986)

51) T.W. Secomb, B.S. Rekowska and A. R. Pries, “Two-dimensional simulation of red blood cell deformation and lateral migration in microvessels”, Annals of Biomedical Engineering, **35**(5), 755-765, (2007)

52) T.W. Secomb, R. Skalak, “A Two-Dimensional Model for Capillary Flow of an Asymmetric Cell”, *Microvascular Research*, **24**, 194-203, (1982)

53) J. Seki and H.H. Lipowsky, “In vivo and in vitro measurements of red cell velocity under epifluorescence microscopy”, *Microvascular Research*, **38**, 110-124, (1989)

54) J.P. Shelby, J. White, K. Ganesan, P.K. Rathod, D.T. Chiu, “A microfluidic model for single-cell capillary obstruction by Plasmodium falciparum-infected erythrocytes”, *PNAS*, **100**, 14618-22, (2003)

55) S.S. Shevkoplyas, S. C. Gifford, T. Yoshida and M. W. Bitensky, “Prototype of an in vitro model of the microcirculation”, *Microvascular Research*, **65**, 132-136, (2003)

56) S.S. Shevkoplyas, T. Yoshida, S.C. Gifford and M.W. Bitensky, “Direct measurement of the impact of impaired erythrocyte deformability on microvascular network perfusion in a microfluidic device”, *LOC*, **6**, 914-920, (2006)

57) R. Skalak, P.I. Branemark, “ Deformation of Red Blood Cells in Capillaries”, *Science*, **164**, 717-719, (1969)

58) V Sibillo, G. Pasquariello, M. Simeone, V. Cristini and S. Guido, “Drop Deformation in Microconfined Shear Flow”, *Physical Review Letters*, 97, 054502, (2006)

59) J.L. Spivak, “Polycythemia vera: myths, mechanisms, and management”, *Blood*, **100**(13), 4272-4290, (2002)

60) M. Sugihara-Seki, B. M. Fu, “Blood flow and permeability in microvessels”, *Fluid Dynamics Researc*h, **37**, 82-132, (2005)

61) M. Sugihara-Seki and R. Skalak, “Asymmetric flows of spherical particles in a cylindrical tube”, *Biorheology,* **34**, 155-169, (1997)

62) G.I Taylor, “The formation of emulsion in definable fields of flow”, *Proceedings of the Royal Society of London: A*, **138**, 41-48, (1934)

63) G.Tomaiuolo, M. Simeone, S. Guido, R. Ciancia, C. Rinaldi, V. Martinelli, B. Rotoli, “A methodology to study the deformability of red blood cells flowing in microcapillaries in vitro”, *Ann Ist Sup Sanità*, 43, 186-192, (2007)

64) K. Tsukada, E. Sekizuka, C. Oshio, H. Minamitani, “Direct measurement of erythrocyte deformability in diabetes mellitus with a transparent microchannel capillary model and high-speed video camera system”, *Microvascular Research*, **61**, 231–239 (2001)

65) G.M. Whitesides, “The origins and the future of microfluidics”, *Nature*, **442**, 368-373, (2006)

Appendix

Publications

1. Tomaiuolo G., Simeone M., Guido S., Ciancia R., Rinaldi C., Martinelli V., Rotoli B. "*A methodology to study the deformability of red blood cells flowing in microcapillaries in vitro"*, The role of hemorheology in clinical medicine, Ann Ist Sup Sanità, 2007, 43, 186-192
2. P.D'Angelo, M.Barra, S.Guido, G.Tomaiuolo and A.Cassinese "*An electric criterion to evaluate glass transition temperature: dielectric relaxation measurements*"; Macromolecular Symposia, 2007, 247, 43-49

Experiences in foreign laboratories

- Short Term Scientific Mission within the COST scientific programme on Physics of droplets at the University of Twente (24 Nov 07- 8 Dec 07)
- University of Texas Health Science Center and MD Anderson Cancer Center, Houston, Texas. Mathematical Modeling of Biological Systems and Disease (Breast cancer) under the supervision of Prof. V. Cristini and in collaboration with Prof. S. Guido of the University of Naples (1 Jun 08 – 15 Aug 08)

Conferences

- (O) G.Tomaiuolo, S.Guido, "Analisi della deformabilità di globuli rossi mediante sistemi Lab-on-Chip", Convegno Le idee della ricerca a lavoro, Napoli (Italy), February 26-27, 2008
- (O) G.Tomaiuolo, V. Preziosi, M. Simeone, S. Guido, R. Ciancia, V. Martinelli, B. Rotoli, "Deformability of red blood cells flowing in microcapillaries *in vitro*", 4th Annual European Rheology Conference AERC 2007, Napoli (Italy), April 12-14, 2006
- (P) G. Tomaiuolo, V. Sibillo, M. Simeone, S. Guido, G. Marrucci, R. Ciancia, C. Rinaldi, V. Martinelli, B. Rotoli, "Deformability-based in vitro analysis of red blood cells flowing in microcapiallries", IX Congresso Nazionale SIES (Società Italiana di Ematologia Sperimentale), Napoli, September 20-22, 2006
  20-22 Settembre 2006, Napoli
- (O) G. Tomaiuolo, M. Simeone, S. Guido, "Deformability of red blood cells flowing in microcapillaries in vitro", Atti del IX Convegno della Società Italiana di Reologia, Tropea, 20-23 settembre 2006, pp. 313-320
- (O) G. Tomaiuolo, V. Sibillo, L. Lanzaro, M. Simeone, S. Guido, "Deformability of red blood cells in microchannels", 3rd Annual European Rheology Conference AERC 2006, Crete (Greece), April 27-29, 2006
- (O) G. Tomaiuolo, V. Sibillo, L. Lanzaro, M. Simeone, S. Guido, "In vitro deformability of red blood cells flowing in microcapillaries by video-enhanced microscopy", 2nd Annual European Rheology Conference, Grenoble (France), April 21-23, 2005
- (P) G. Tomaiuolo, V. Sibillo, L. Lanzaro, M. Simeone, S. Guido, C. Rinaldi, B. Rotoli, "In vitro deformability of red blood cells flowing in microcapillaries by

video-enhamced microscopy", 13th Conference of the European Society for Clinical Hemorheology (E.S.C.H.), Siena, 26-29 giugno 2005

- (O) G. Tomaiuolo, V. Sibillo, L. Lanzaro, M. Simeone, S. Guido, "Deformability of red blood cells flowing in microcapillaries in a gel matrix", Society of Rheology 77th Annual Meeting, Vancouver (Canada), October 16-20, 2005
- (O) S. Guido, G. Tomaiuolo, M. Simeone, V. Martinelli, C. Rinaldi, B. Rotoli, "Viscosità del sangue periferico e deformabilità eritrocitaria in condizioni di ipercitosi nel flusso in microcapillari", Emoreologia: Fisiopatologia e Clinica, Istituto Superiore di Sanità, Roma, 11 novembre 2005

A methodology to study the deformability of red blood cells flowing in microcapillaries *in vitro*

Giovanna Tomaiuolo[(a)], Marino Simeone[(a)], Stefano Guido[(a)], Rosanna Ciancia[(b)], Ciro Rinaldi[(b)], Vincenzo Martinelli[(b)] and Bruno Rotoli[(b)]

[(a)] Dipartimento di Ingegneria Chimica; [(b)] Dipartimento di Biochimica e Biotecnologie Mediche, Servizio di Ematologia, Facoltà di Medicina e Chirurgia, Università degli Studi "Federico II", Naples, Italy

Summary. The deformability of red blood cells flowing in microvessels is essential to maintain optimal blood circulation and to allow gas transfer between blood and tissues. Here, we report on an experimental methodology to investigate the deformability of RBCs flowing in microcapillaries having diameter close to the average cell size. The microcapillaries are placed in a rectangular flow cell, where a suspension of RBCs, isolated by centrifugation and properly diluted in albumin-additioned ACD, is fed through a syringe under the action of a liquid head in the physiological range. Video microscopy images of the flowing RBCs are acquired at high magnification and later processed by an automated image analysis macro. It was found that RBCs from healthy donors exhibit the classical parachute shape observed *in vivo*. Furthermore, all the data of healthy RBC velocity *vs* liquid head are well represented by the same linear regression, indipendently on the donor. Preliminary results on β-thalassemia RBCs are also presented and show, on the average, a reduced velocity compared to healthy samples.

Keywords: erythrocytes, capillaries, erythrocyte deformability, microfluidics, thalassemia.

Riassunto *(Una metodologia per lo studio* in vitro *della deformabilità di globuli rossi in flusso attraverso microcapillari)*. La deformabilità dei globuli rossi circolanti nei vasi di piccolo calibro è una proprietà essenziale per mantenere un flusso ottimale e per consentire gli scambi gassosi fra sangue e tessuti. In questo contributo viene descritta una metodica sperimentale per lo studio della deformabilità di globuli rossi in flusso attraverso microcapillari artificiali di diametro paragonabile alla dimensione cellulare media. I microcapillari sono collocati in una cella di flusso rettangolare, in cui una sospensione di globuli rossi, isolati mediante centrifugazione ed opportunamente diluiti in ACD addizionato di albumina, viene inviata mediante una siringa sotto l'azione di un battente liquido nel range fisiologico. Le immagini di globuli rossi in flusso sono acquisite ad elevato ingrandimento mediante video microscopia ottica ed elaborate successivamente attraverso routine di analisi dell'immagine. I globuli rossi da donatori sani mostrano la classica forma a paracadute osservata *in vivo*. Tutti i dati di velocità eritrocitaria in funzione del battente liquido per donatori sani sono inoltre ben rappresentati dalla stessa regressione lineare, indipendentemente dal donatore. Risultati preliminari su globuli rossi da pazienti affetti da β-talassemia mostrano in media una riduzione di velocità rispetto ai campioni da donatori sani, in accordo con la ridotta deformabilità di membrana associata a questa patologia.

Parole chiave: eritrociti, capillari, deformabilità eritrocitaria, microfluidica, talassemia.

INTRODUCTION

The deformability of red blood cells (RBCs) flowing in microvessels is essential to maintain optimal blood circulation and to allow gas transfer between blood and tissues, and is implicated in several physiopathological processes. RBC deformability has been the subject of a number of investigations in the literature. One of the main research directions in this area has been the design of flow cells somehow mimicking the fluidodynamic conditions experienced by RBCs in the microcirculation *in vivo*. The experimental methods so far reported in the literature include sedimentation velocity of centrifuged blood [1], filtration through membranes with different porosity [2, 3], the time spent by RBCs in passing through a single membrane pore [4], blood viscosity as a function of the deformation velocity [5, 1], the aspiration of a single RBC in a micropipette [6, 7], the diffraction of RBC suspensions undergoing shear flow in a Couette rheometer (ektacytometer, [8], the separation between two microspheres adherent to RBC surface using optical tweezers [9-11]. A measurement associated, though indirectly, to RBC deformability is that of blood viscosity, which depends both on plasma

Indirizzo per la corrispondenza (Address for correspondence): Stefano Guido, Dipartimento di Ingegneria Chimica, Università degli Studi di Napoli "Federico II", P.le V. Tecchio 80, 80125 Naples, Italy. E-mail: stefano.guido@unina.it

composition and on the properties and concentration of the suspended cells [12]. It was indeed found that blood viscosity is higher if RBCs are made less deformable (for example, by crosslinking with glutaraldehyde [13]. From the haemorheological point of view, one of the most popular techniques is the measurement of apparent viscosity of whole blood or RBC suspensions at different concentrations in artificial capillaries, usually made of glass or silica [14]. These studies include the pioneering work of Fåhræus [15] on the variation of apparent blood viscosity with capillary diameter. Even though this rheological approach is still followed, direct measurements of deformability of RBCs flowing in microcapillaries with size smaller than cell body are scarce in the literature. In fact, observations of flowing RBCs by optical microscopy have been mainly described for capillary diameters larger than cell size [14]. Data of RBC deformability in case of pathological cells are even more limited.

The progress of the experimental techniques has been paralleled by the development of theoretical analyses to model the ability of RBC to deform and flow through channels smaller than the size of the cells at rest. The deformability, defined as the extension of the cell body under the steady state application of a fluidodynamic stress, is mainly function of three variables: internal viscosity, surface/volume ratio, and viscoelasticity of the membrane [16, 17]; The structure of RBC membrane has been modelled on a microscale as a network of elastic elements [18, 19]. The relation between deformability and morphology has been also studied, focusing on the change from the usual biconcave shape to the one observed for echinocytes and stomatocytes [20]. Notwithstanding the recent applications of numerical simulation techniques [21] the modelling of RBC fluidodynamic behavior and the comparison with experimental data are still at a preliminary stage, especially for pathological situations, and further investigations are at order.

In fact, in spite of the progress in experimental techniques, from the clinical standpoint RBC deformability is still measured by quite approximate methods, for example by measuring the time of perfusion through filters with pores of a given size. The main limits of this technique are the difficult standardization of the methodology, the intrinsic variability of pore size, the lack of information concerning single cell deformability, and the limited quantitative results that can be so obtained. Therefore, the setup of novel experimental systems *in vitro* appears as a relevant research goal towards a deeper understanding of the biological significance of RBC deformability, especially in a physiopathological perspective.

In this work, we describe an experimental methodology to investigate RBC deformability in microcapillaries having internal diameter close to cell size. Our approach is based on direct visualization of flowing RBCs by video-enhanced microscopy and automated image analysis procedures to measure cell velocity and deformation. The experimental variables investigated in this work include flow rate, size and length of microcapillaries. RBCs from healthy donors and from patients suffering from β-thalassemia have been investigated; preliminary results are presented and discussed.

MATERIALS AND METHODS

Blood samples

For analyses of β-thalassemic erythrocytes, fresh venous blood was drawn from both healthy and β-thalassemic consenting volunteers into Vacutainer tubes . Healthy samples were used as control. All blood samples were used within 4h of collection. RBC viability was checked before each experiment by observing cell morphology under static conditions at high magnification (100x objective). Approximately 1 mL of whole blood was diluted with 100 mL of anticoagulant ACD (0.6% citric acid, 1.1% dextrose anhydrous, 2.3% sodium citrate, 96% water), 5 mL of human albumin and 5 mL of PBS (phosphate-buffered saline). Such level of dilution ensured optimal performance of the flow cell. The viscosity of the suspending fluid was measured by a Ubbelohde glass viscometer immersed in a water bath at 37 °C, and was equal to 0.8 mPa·s. The presence of RBCs at the dilution used in the experiments did not change significantly the value of fluid viscosity.

Experimental apparatus

The microcapillaries used in this work were either made of silica (with 5 and 6.6 μm ID, Polymicro Technologies) or embedded in a gel matrix. In the latter case, a 2% w/w agarose solution at ca. 90 °C was cast in a rectangular mold enclosing a 5 micron diameter gold-plated tungsten wire. After gelation, the wire was gently removed from the agarose slab, thus leaving a 5 μm microcapillary. The diameter and the length of all the capillaries used in this work were carefully measured by video microscopy. The measurements were carried out by filling the capillaries with an isorefractive fluid to avoid optical distortions.

The flow cell (a schematic is shown in *Figure 1*) was made of two Plexiglass plates separated by a rubber spacer. A window was cut in the bottom plate to allow insertion of a coverslip slide for observations at high magnifications with oil immersion objectives. The RBC suspension was fed to the flow cell through an input hole by a flexible tubing connected to a syringe. The suspension coming out from the flow cell through an output hole was collected by a plastic tubing in a glass reservoir placed on a vertical translating stage. The distance between the liquid menisci in the feeding syringe and the exit reservoir was adjusted by the translating stage. Such liquid head was measured during the experiment by imaging both the syringe and the exit reservoir with a CCD video camera against a graph paper background. This allowed to monitor the pressure differential in the course of the experiment.

The flow cell was placed on the motorized x-y stage of

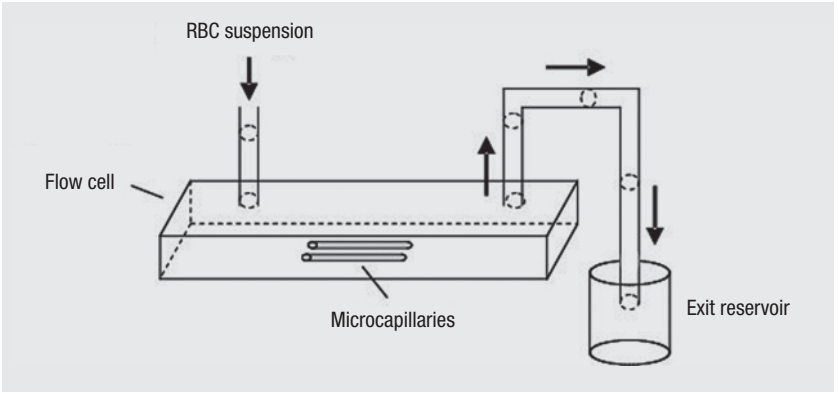

Fig. 1 | *Schematic of the flow cell.*

an inverted microscope (Zeiss Axiovert 100) equipped with a motor assembly for focus control. Sample positioning was controlled by a custom LabView routine. In each experiment sample temperature was kept at 37 °C by enclosing the microscope and the flow cell assembly (including the feeding syringe and the exit reservoir) in a Plexiglass cage equipped with an air thermostating system based on a PID controller.

Images of the flowing RBCs were acquired by another CCD videocamera (Hitachi) and the whole experiment was recorded on video tape for reference (this recording was synchronized with that of the liquid head for later comparison). Real time image sequences (1000 images at a rate of 25 frames/s) were also digitized during the experiment by means of a frame grabber (National Instrument IMAQ PCI 1409) installed on a Pentium-based host PC and saved in computer memory for later analysis. The images were processed off-line by a macro calling standard image analysis routines from the library of a commercial package (Image Pro Plus 4.5). The fully automated macro operation allowed to isolate the subsets of images from each sequence where the passage of a cell could be identified and to determine the position of the flowing cell as a function of time. From these data RBC velocity was calculated as the slope of cell displacement vs time. Images of the flowing RBC were then saved in a database to evaluate the extent of cell deformation under the action of flow.

Images of RBCs at rest were also acquired to evaluate the cell size distribution. The measurements were carried out by pouring a drop of the dilute cell suspension between a microscope slide and a coverslip and acquiring images of several fields of view (the total number of counted cells was around 200). RBC size was measured by image analysis as the diameter of the cell body in the plane of observation (tilted cells were not considered in the measurements).

RESULTS

In a typical experiment, the pressure differential across the microcapillaries was regulated by adjusting the relative liquid levels in the syringe and the exit reservoir. The liquid head was initially set to 30 cm H_2O for about 5 minutes to fill the inlet and outlet tubings and the flow chamber. Then, the liquid head was brought to 13 cm H_2O by lowering the position of the exit reservoir. The following decrease of the liquid head due to the emptying of the syringe and the filling of the exit reservoir was continuously recorded during the whole experiment by using the second CCD videocamera. From time to time, the syringe was refilled and the liquid head set back to 30 cm H_2O for about 10 minutes to prevent RBC sedimentation and the possible clogging of the outlet tubing around the exit hole.

As described in the previous section, real time image sequences were acquired throughout the experiment and processed off-line by the image analysis macro. The passage of an RBC through the microcapillary under observation was then associated to the current liquid head from the continuous recording of the distance between the two liquid levels in the syringe and the exit reservoir. A typical plot of cell displacement as a function of time in a silica microcapillary from a healthy donor sample is shown in *Figure 2a*, where the symbols refer to the data points and the solid line is the corresponding linear regression (the coefficients are also shown in the figure). Capillary length and diameter are 3.6 mm and 6.6 μm, respectively. It can be noticed that the data points follow quite closely a linear trend (the R^2 value of the regression is close to 1), thus showing that at the point of observation (which is located about halfway between the inlet and outlet microcapillary sections) RBC flow is under steady state conditions. The slope of the linear regression is the cell velocity, which is ca. 166 μm/s. An image of the flowing RBC is also shown in the inset of *Figure 2a*. The classical parachute shape, which is found *in vivo* [22], can be clearly observed in the image, and shows that the cells are indeed subjected to flow conditions similar to those experienced under physiological conditions. Similar shapes are also observed in the capillaries embedded in the agarose gels, as shown in *Figure 2b* (capillary ID is around 5 μm). It so appears that the parachute shape is due to the imposed fluidodynamics, and is essentially independent on the inner surface of the microcapillary.

The data analysis procedure illustrated in *Figure 2a* was systematically applied in a range of liquid heads

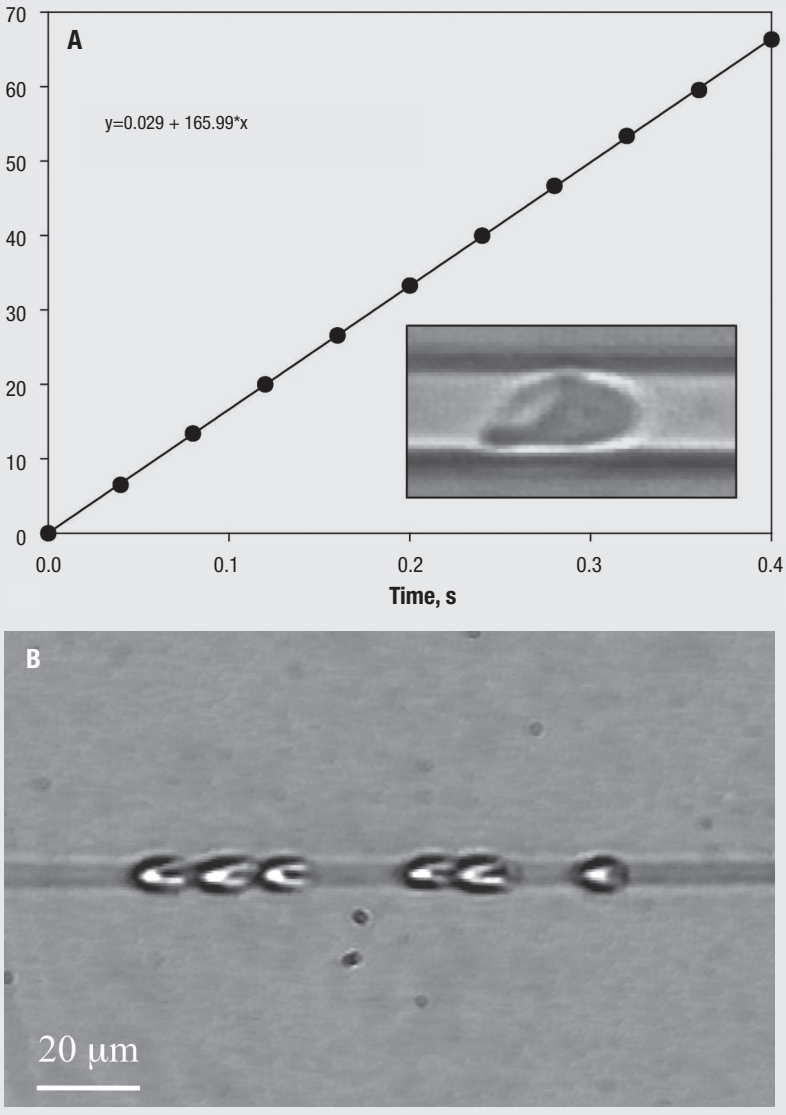

Fig. 2 | *A) Cell displacement* vs *time in a microcapillary; B) images of RBCs flowing in a microcapillary embedded in agarose gel.*

from 1 to 10 mmHg. At each value of liquid head the velocity of 10-20 RBCs was measured. The results from three different healthy donors are plotted in *Figure 3a*. Each point in *Figure 3a* is the average value of RBC velocity from several measurements at the corresponding liquid head, and the errors bars represent the standard deviation of the data. The three sets of points correspond to experimental runs from different donors with different capillary length from 3.6 to 4.9 mm, and the solid lines are linear fit to the data. All the data sets are well represented by the linear fit, and tend to zero at vanishing liquid head. This shows that the measured liquid head is dominated by the pressure drop between the ends of the microcapillaries, the other pressure losses (feeding and exit tubings, pressure drop due to converging flow to the capillary) being negligible.

In *Figure 3b* the same sets of data as in *Figure 3a* are scaled to the capillary length of 3.6 mm by assuming a direct proportionality between cell velocity and capillary length. It can be noticed that this scaling makes the three data sets superimpose each other, thus generating a "master curve" of healthy RBC velocity vs liquid head. In other words, the microcapillary flow behaviour of healthy RBCs does not depend on the donor, and it can be taken as a reference to be compared to pathological situations. The solid line shown in *Figure 3b* is the calculated value of the average fluid velocity $\langle v_z \rangle$ along the capillary axis z according to the classical equation

$$\langle v_z \rangle = \frac{\Delta P R^2}{8 \mu L} \qquad (1)$$

where ΔP is the liquid head, R and L are capillary radius and length, respectively, and μ is the viscosity of the suspending liquid (which was measured

by glass viscometry as described in the experimental section). The above equation is based on the assumption of well developed parabolic flow of a Newtonian fluid in a circular cross-section tube (Poiseuille flow), and does not contain any fitting parameters. The agreement between equation (1) and the experimental data of healthy RBC viscosity in *Figure 3b* is quite good. It shows that healthy RBCs move in a plug flow fashion inside microcapillaris of diameter comparable to cell size. The average RBC size at rest of the healthy samples was around 7 μm with a standard deviation of 0.5, as measured by optical microscopy and image analysis (see experimental section for details).

The measurements of RBC velocity vs liquid head from healthy donors were used as a control to evaluate the flow behavior of pathological blood samples. To exemplify the application of our methodology to pathological RBCs, we report preliminary data from β-thalassemia blood samples. In *Figure 4*, the RBC velocity of four heterozygous β-thalassemia patients is plotted as a function of the liquid head. In the same figure, results from healthy RBCs are also shown for comparison. *Figure 4* shows that data from the β-thalassemia patients investigated in this work follow a linear trend passing through the origin. At variance with the healthy RBC results, however, β-thalassemia data do not superimpose on the same "master curve", but rather exhibit different slopes, one being even coincident with the healthy case. The remaining three pathological data sets fall significantly below the velocity of healthy RBCs (the slopes are between 64% and 35% smaller), thus showing an increased hydrodynamic resistance in microcapillary flow. The lower panel in *Figure 4* shows representative images of flowing

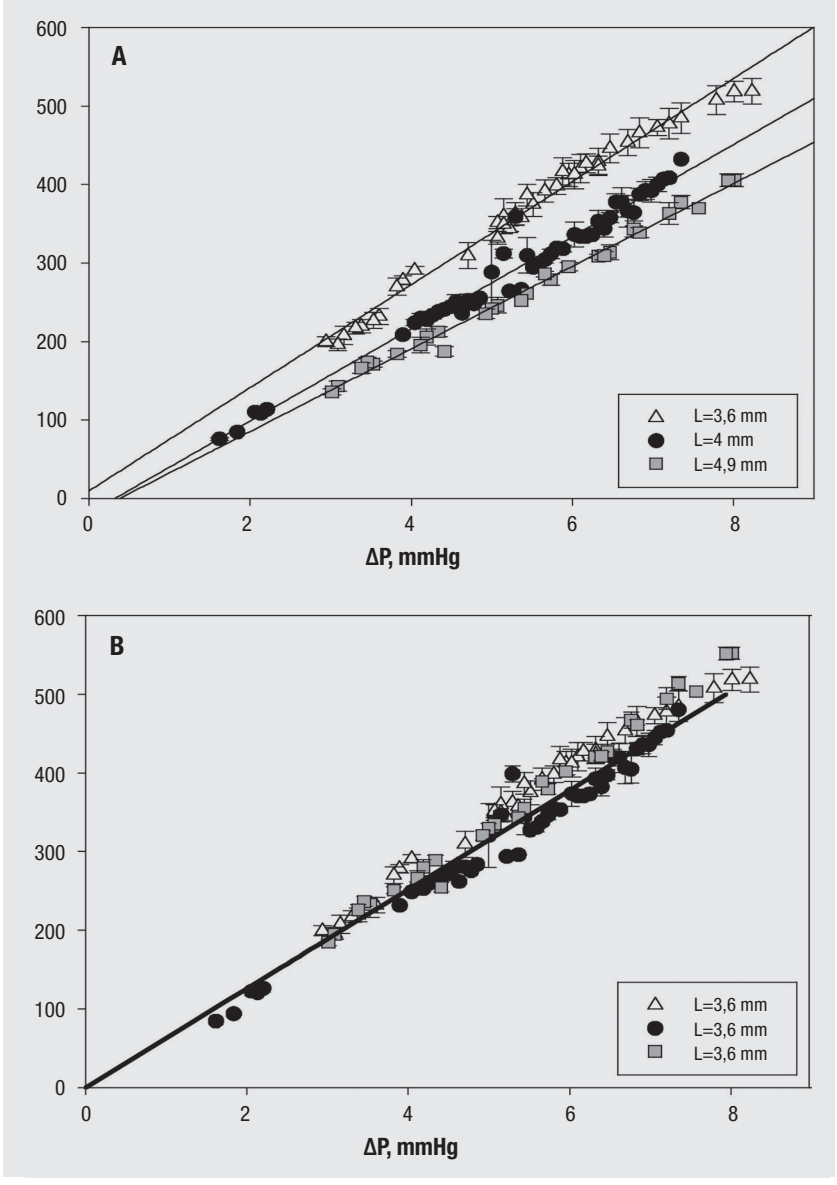

Fig. 3 | *A) RBC velocity vs liquid head for three samples from healhty donors in microcapillaries of different lengths; B) same data as in A) rescaled to the same microcapillary length by assuming direct proportionality between RBC velocity and microcapillary length.*

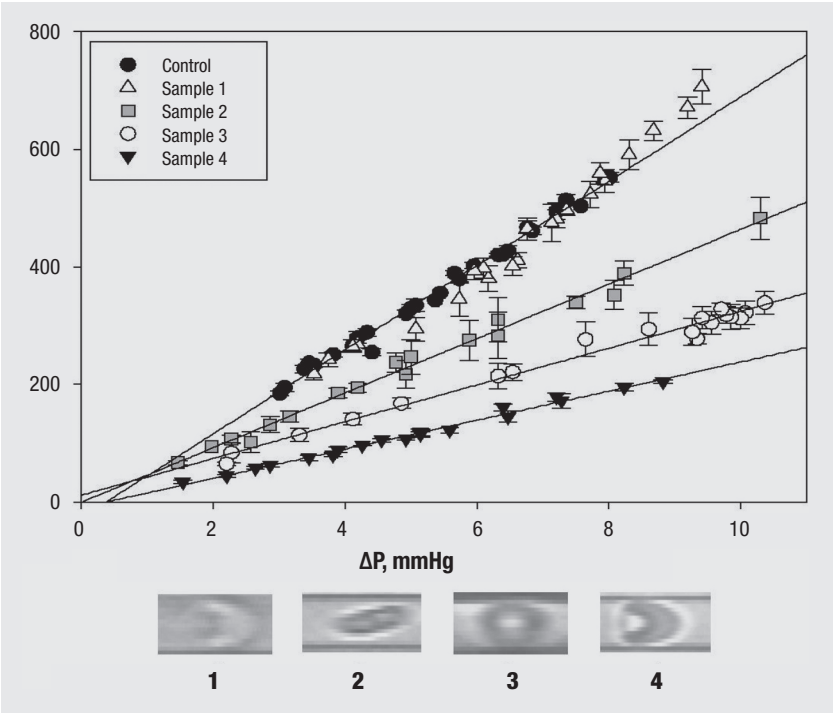

Fig. 4 | *RBC velocity vs liquid head for four samples from β-thalassemia patients and one control from a healthy donor.*

β-thalassemia RBCs from the four samples investigated at a liquid head of ca. 6.5 mmHg. A parachute-like cell shape was observed in most images of the flowing RBCs, in analogy with the healthy samples. The RBC size distribution at rest was determined by video microscopy and image analysis for the β-thalassemia samples of *Figure 4*. The average size was slightly lower compared to the healthy case, going from to 6.6 to 7.0. Some hematological data for the blood samples of *Figure 4* are presented in *Table 1*. No simple correlation between RBC velocity and hematological parameters can be derived from *Table 1*. A systematic investigation to extend these preliminary results is currently in progress.

CONCLUSIONS

In this work, we describe an experimental methodology to investigate the flow behaviour of RBCs in microcapillaries of diameter comparable to cell size. Our approach is based on imaging deformed RBCs at high magnification by a video microscopy workstation equipped with a motorized stage for precise positioning of the flow cell and a temperature control system. The acquired images are processed by image analysis techniques in an automated way to measure RBC velocity as a function of the imposed pressure differential. The performance of the apparatus was tested on blood samples from healthy donors, and it was found that RBC velocity is not dependent on the donor and is equal to the average fluid velocity in the microcapillary as calculated from the classical Poiseuille equation.

Preliminary results from heterozygous β-thalassemia patients are also reported, and show an average decrease of RBC velocity with respect to the healthy individuals. This is not unexpected, since it is well known that β-thalassemia is associated with an increased rigidity and a reduced mechanical stability of the cell membrane and cytoskeleton, leading to impaired RBC deformability [23]. Evidence

Table 1 | *Haematological data of the blood samples of Figure 4*

Sample	HGB, g/dl	HCT, (%)	MCV, fL	D* (± SD)
Control	13.2	42.1	85.6	6.9 (±0.6)
1	15	47.7	75.5	6.35 (±0.63)
2	8.8	30.1	65.6	6.5 (±0.94)
3	13	40.8	60.1	7.0 (±0.92)
4	13.9	43.8	72.2	6.4 (±0.78)

D is the RBC diameter in the plane of observation.*
SD = standard deviation.

of reduced deformability in β-thalassemia RBCs suspended in PBS viscosized with addition of dextran has been provided by laser diffractometry [24] in a flat glass cell. However, a direct visualization of RBC shape and velocity in a microcapillary of comparable size, such as in the present investigation, has not been reported so far to our knowledge. A further advantage of our approach is that it allows one to discriminate the flow deformability of RBCs from different patients and to give a quantitative evaluation of the difference with respect to the healthy case. A systematic work to elucidate the microcapillary flow behaviour of β-thalassemia RBCs and to correlate these results with clinically relevant parameters is currently in progress.

Acknowledgments

Financial support from the Italian Ministry of University under the Prin 2004 program is gratefully acknowledged.

Submitted on invitation.
Accepted on 3 April 2007.

References

1. Sirs JA. The measurement of the haematocrit and flexibility of erythrocytes with a centrifuge. *Biorheology* 1968;5:14.
2. Teitel P. Basic principles of the "filterability test" (FT) and analysis of the erythrocyte flow behavior. *Blood Cells* 1977;3:55-70.
3. Dormandy J, Flute P, Matrai A, Boger L, Mikita J. The new St. George's blood filtrometer. *Clin Hemorheol* 1985;5:975-83.
4. Kiesewetter H, Mussler K, Teitel P, Dauer U, Schmid-Schonbein H, Sphor R. New methods for red cell deformability measurement. In: Lowe GDO, Barbenel JC, Forbes CD (Ed.). *Clinical aspects of blood viscosity and cell deformability*. Berlin: Springer-Verlag; 1981.
5. Dupin PA, Sirs JA. The relationship of plasma fibrinogen, erythrocyte flexibility and blood viscosity. *Thromb Haemost* 1977;38:660-7.
6. Evans EA. New membrane concept applied to the analysis of fluid shear – and micropipette-deformed red blood cells. *Biophys* J 1973;13:941-54.
7. Chien S. Principles and techniques for assessing erythrocyte deformability. *Blood Cells* 1977;3:71-99.
8. Bessis M, Mohandas N. A diffractometric method for the measurement of cellular deformability. *Blood Cells* 1975;1:307-13.
9. Ashkin AJ, Dziedzic M, Yamane T. Optical trapping and manipulation of single cells using infrared laser beams. *Nature* 1987;330:769-71.
10. Hénon S, Lenormand G, Richter A, Gallet F. A new determination of the shear modulus of the human erythrocyte membrane using optical tweezers. *Biophys J* 1999;76:1145-51.
11. Sleep J, Wilson D, Simmons R, Gratzer W. Elasticity of the red cell membrane and its relation to hemolytic disorders: an optical tweezers study. *Biophys J* 1999;77:3085-95.
12. Hoffman R, Benz EJ Jr, Shattil SJ, Furie B, Cohen HJ, Silberstein LE, Mc Glave P. *Hematology basic principles and practice*. Philadelphia: Churchill Livingstone; 2000.
13. Fung YC. *Biomechanics: Mechanical properties of living tissues*. New York: Springer Verlag; 1993.
14. Pries AR, Neuhaus D, Gaehtgens P. Blood viscosity in tube flow: dependence on diameter and hematocrit. *Am J Physiol* 1992;263 (Heart Circ Physiol 32):H1770-8.
15. Fåhræus R, Lindqvist T. The viscosity of the blood in narrow capillary tubes. *Am J Physiol* 1931;96:562-8.
16. Mohandas N, Chasis JA. Red blood cell deformability, membrane material properties and shape: regulation by transmembrane, skeletal and cytosolic proteins and lipids. *Semin Hematol* 1993;30:71-92.
17. Mohandas N, Evans E. Mechanical properties of the red cell membrane in relation to molecular structure and genetic defects. *Annu Rev Biophys Biomol Struct* 1994;23:787-818.
18. Boey SK, Boal DH, Discher DE. Simulations of the erythrocyte cytoskeleton at large deformation. I. Microscopic models. *Biophys J* 1998;75:1573-83.
19. Hansen JC, Skalak R, Chien S, Roger A. An elastic network based on the structure of the red blood cell membrane skeleton. *Biophys J* 1996;70:1466-6.
20. Kuzman D, Svetina S, Waugh RE, Zeks B. Elastic properties of the red blood cell membrane that determine echinocyte deformability. *Eur Biophys J* 2004;33:1-5.
21. Pozrikidis C. Numerical simulation of the flow-induced deformation of red blood Cells. *Ann Biomed Eng* 2003;31:1194-205.
22. Tsukada K, Sekizuka E, Oshio C, Minamitani H. Direct measurement of erythrocyte deformability with a transparent microchannel capillary model and high-speed video camera system. *Microv Res* 2001;61:231-9.
23. Yuan, J, Bunyaratvej A, Fucharoen S, Fung C, Shinar E, Schrier SL. The instability of the membrane skeleton in thalassemic red blood cells. *Blood* 1995;86:3945-50.
24. Bunyaratvej A, Butthep P, Sae-Ung N, Fucharoen S, Yuthavong Y. Reduced deformability of thalassemic erythrocytes and erythrocytes with abnormal hemoglobins and relation with susceptibility to *Plasmodium falciparum* invasion. *Blood* 1992;79:2460-3

An Electric Criterion to Evaluate Glass Transition Temperature: Dielectric Relaxation Measurements

P. D'Angelo,[*1] *M. Barra,*[1] *A. Cassinese,*[1] *S. Guido,*[2] *G. Tomaiuolo*[2]

Summary: In this contribution, a dielectric measurement technique for the evaluation of phase transition temperature and the study of physical aging on polymeric thin films is considered. This kind of measurement provides the possibility of displaying phase transitions with a high degree of precision. Furthermore, it can be considered alternatively to techniques not applicable in the case of thin films, such as Differential Scanning Calorimetry (DSC). In this work, owing to the high sensitivity of the utilized experimental set-up, a glass transition T_G of 156 K, with a precision equal to 0.3%, and a melting $T_M = 220$ K have been assessed for 4 μm thick Polydimethylsiloxane (PDMS) films. Performing measurement as a function of time, it was possible to monitor physical aging phenomena, mainly consisting in a change of dielectric properties. As expected, the time evolution of the aging phenomena can be described by a simple logarithmic law.

Keywords: A.C. measurements; dielectric relaxation; glass transition; physical aging; Universal Dielectric Response

I. Introduction

The growing worldwide interest for organic electronics is justified by the possibility to fabricate low cost devices, which can be easily integrated with large area and flexible substrates, unlike the more traditional silicon based devices.[1,2] In this regard, the study of the properties exhibited by polymers grown as thin films, used as substrates or active layers, is very important in order to optimize their electrical behavior and investigate the real application perspectives.[3]

In particular, concerning their structural properties, it is well known that amorphous polymers undergo both a glass, T_G, and a melting, T_M, transitions, producing the change of the mechanical properties. Furthermore, polymers display also a physical aging which can be responsible for device performance degradation.

About the experimental evaluation of T_G, it should be observed that its value can be strongly affected by the conditions of the performed experiment. Indeed, it is widely reported in literature that the T_G value depends on the film thickness and on the interactions between the film and the substrate.[4,5] Due to this dependence, T_G value can change of many tens of degrees. Usually, T_G is determined by performing thermo-mechanical measurements, such as Differential Scanning Calorimetry (DSC),[6] requiring very thick specimens.[7] A more refined version of this technique, the so called Ultrasensitive Differential Scanning Calorimetry[8] can be used also on thin films, but it operates only in particular and restrictive conditions. More recently, T_G has been evaluated on thin PDMS films by means of electrical measurements; in particular R(T) measurements can highlight the glass transition but, unfortunately, these measurements require a doping procedure.[9] Actually, it is clear that by this

[1] CNR-INFM Coherentia and Dipartimento di Scienze Fisiche, Università di Napoli "Federico II", Piazzale Tecchio 80, Naples, 80125 Italy
E-mail: pdangelo@na.infn.it
[2] Dipartimento di Ingegneria Chimica, Università di Napoli "Federico II", Piazzale Tecchio 80, Naples, 80125 Italy

technique the T_G value can be modified by the presence of dopants and by their concentration.[10,11]

An alternative electrical tool for the evaluation of glass transition temperature in polymeric films is represented by dielectric relaxation measurements, consisting in the visualization of both the dielectric permittivity ε_r and the a.c. conductivity $\sigma_{a.c.}$ (i.e. dielectric losses).[12] Such measurements allow to study the local and cooperative chain dynamics of polymers, both in the liquid and solid state, across an extremely wide range of frequencies (10^{-2}–10^{10} Hz). In particular, the segmental dynamics, which is referred to as the α-relaxation (in the low and middle frequency regions, up to 10^5 Hz), reflects the dynamic glass transition. In this scenario, the temperature dependence of the dielectric function $\varepsilon(T,\omega)$ (where $\varepsilon(T,\omega) = \varepsilon^{|}(T,\omega)\text{-}i\varepsilon^{||}(T,\omega)$, with $\varepsilon^{|}(T,\omega) = \varepsilon_r(T,\omega)$ and $\varepsilon^{||}(T,\omega)^*\omega^*\varepsilon_0 = \sigma_{a.c.}(T,\omega)$), for a fixed frequency ω belonging to the above mentioned range, allows to display the phase transition and consequently to evaluate qualitatively the value of T_G. By this measurement procedure, the precision of the extracted T_G value is strictly related to the high degree of cleanliness that can be reached. Furthermore, the permittivity ε_r allows also to monitor the Physical Aging coming from the modification of dielectric properties, since the degradation is related to the cooperative motion of chains too.[13] In this paper, we report on the evaluation of T_G and T_M of PDMS (Poly-dimethylsiloxane) thin films, by using a dielectric measurement technique. A first analysis of Physical Aging undergone by the same material has been reported too. The choice of PDMS is due to the fact that it is one of the most known Semi-Crystalline Polymers. Its simple chemical constituent (Fig. 1) is a backbone $[SiO(CH_3)_2]_n$ arranged in a network-like structure, where the Si–O bonds give a considerable flexibility to the polymeric backbone. PDMS is widely studied both for its mechanical and unusual rheological properties, which render its applications interesting in several fields, such as microfluidics.[14] In addition, it is believed that due to its low dielectric constant value, it is also a good candidate for microelectronics,[15] in particular for Organic FET applications.[16]

Further developments of such technique, concerning its application to different organic materials with T_G between 300 and 400K, will be reported elsewhere.

Moreover, we are going to analyze the opportunity of describing the T_G behavior as a function of the a.c. electrical field frequency according to a logarithmic behavior related to relaxation phenomena in supercooled liquids.[17]

II. Experimental Details: Samples Preparation and Experimental Setup

The starting point of our analysis was the fabrication of simple parallel plane plate capacitors, filled with PDMS dielectric films (Fig. 1).

Usually, such devices are employed to study and characterize the dielectric and conducting properties of many materials by the determination of the permittivity, ε_r, and the a.c. conductivity, σ, as a function of frequency, temperature and d.c. bias. These quantities can be simply extracted from a measurement of the capacitance C and conductance G by the formulas:

$$\varepsilon_r = \frac{C * d}{\varepsilon_0 * S}; \quad \sigma = \frac{G * d}{S} \tag{1}$$

where ε_0 is the vacuum permittivity, S is the surface of the metallic plates and d the thickness of the material filling the capacitor. In our work, the PDMS films were sandwiched between an Ag bottom electrode (S about 9 mm^2), deposited by sputtering on glass substrates, and an Al top electrode, deposited on the top of the PDMS by thermal evaporation technique in high vacuum conditions (10^{-6} mbar).

PDMS thin films, Sylgard 184 purchased by Dow Corning, were spin coated in a clean room on the above mentioned metallic plates; in detail, Sylgard 184 is a

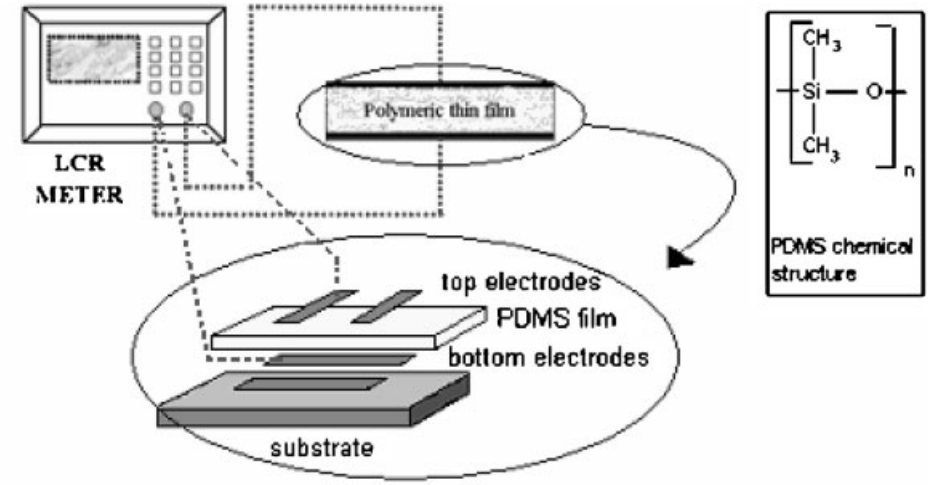

Figure 1.
Layout of the experimental set up and geometry of the manufactured capacitor. In the inset, the chemical structure of PDMS monomer is displayed.

two-component heat-curing system and consists of one part of curing agent and ten parts of base (by weight). The base and the curing agent were mixed in a plastic cup using a plastic spoon for at least a few minutes, depending on the amount of material. After the mixing, the silicone mixture needed to be degassed in vacuum in order to remove air bubbles incorporated during the mixing phase. When the silicone was completely clear and transparent it was ready to be spinned. After spinning, the samples were annealed for one hour at 100 °C. Capacitance and conductance were measured in vacuum both as a function of frequency and temperature by an Agilent LCR meter (Fig. 1). To this end, the sample was mounted in a cryogenerator which allows to perform measurements in a temperature range between 40–340 K. For higher temperatures, a vacuum probe station, already described in ref. [18], can be used. The cryogenerator, furnished with an antivibrating support, was then connected to the LCR meter by means of SMA connectors. The experimental resolution for the capacitance and conductance measurements is equal to 10^{-1} pF and 10^{-10} S, respectively. The electrical connections on the sample inside the cryogenerator were made mainly by spot weldings and, sometimes, by silver paste, avoiding contacts between the silver paste solvent and the polymer.

The analysis here reported has been performed in a temperature range starting from room temperature down to 40 K, with a cooling rate of 5K/min, and subsequently by warming up the samples with an heating rate, slower than 2 K/min. In this way, it is possible to evidence the differences induced on phase transitions by different cooling-warming rates.[19] Finally, temperature was monitored accurately with two different thermometers.

III Experimental Results: Phase Transitions and Physical Aging

As described above, the experimental set up allows to perform a complete analysis of the dielectric response as a function of temperature, frequency and applied d.c. bias. However, here, our analysis has been focused on the detection of the phase transitions and on the study of the aging effects by measurements mainly performed as a function of temperature and time. A more complete analysis, including the

dielectric response dependence on frequency and d.c. bias will be reported elsewhere, also considering different sample geometries.

Phase Transition

In Fig. 2, typical capacitance (Fig. 2.a) and conductance (Fig. 2.b) measurements, performed as a function of temperature, are reported. These measurements were carried out at a frequency of 1 KHz and with an a.c. voltage $V = 0.1$ Volt. No significant changes have been observed by increasing the a.c. voltage level up to 10 Volts.

As expected, at room temperature, the permittivity value for PDMS extracted by the formula (1) is about 2.4, while the d.c. conductance results to be limited by the experimental set-up, since as expected from the data reported in literature it is lower than 10^{-10} S.[20]

Focusing the attention on the curves displayed in Fig. 2a, the experimental measurements well agree with the predictions of the Free Volume Theory.

Below T_G, the available specific volume (where polymeric chains present a non null segmental mobility) reduces to its minimum value, so the rotation of the bonds doesn't occur any more (the material becomes hard). As a consequence, ε_r is constant and increases only approaching T_G. On the contrary, above T_G in the temperature range corresponding to the

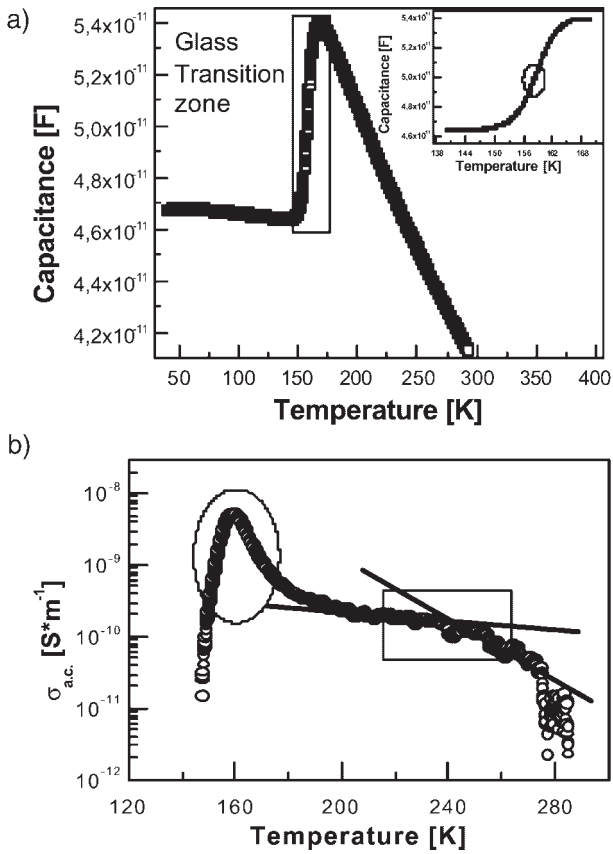

Figure 2.

Capacitance (a) and Conductivity (b) as a function of temperature measured at f = 1 KHz. The glass and melting transition regions are circled. T_G value corresponds to the maximum of the conductivity or to the inflection point of the capacitance curve. The glass transition region is magnified in the inset. T_M corresponds to the slope change in the conductivity curve (Fig. 2.b).

rubber-like phase, the regained thermal expansion of the polymeric film, frozen in the glassy phase, increases the thickness of the material, decreasing capacitance.

Here, T_G corresponds to the inflection point in the left side of the peaks evaluated by computing with ORIGIN software the second derivative (not reported).

As far as the a.c. conductivity is concerned (see Fig. 2.b), its maximum value (maximum of the losses in the material) corresponds to the T_G value. Moreover, it is noteworthy that the $\sigma_{a.c.}(T)$ shows obviously both the phase transitions occurring in the material. Indeed, one can retain that T_M corresponds to the change in slope of conductivity, as indicated in Fig. 2.b.

The frequency dependence of measurements shows that T_G undergoes a shift towards higher values of temperatures if the frequency of the applied field increases (Figs. 3, 4). As a consequence, the static value of T_G is obtained by considering the limit of the frequency towards zero (d.c. limit), as indicated in Fig. 3 with a black line.

Since the ε_r (T) curves are nearly indistinguishable at lower frequencies (Fig. 3), the quasi-static value of T_G has been extrapolated from the curve recorded at 300 Hz. Such value is equal to 156 K, in good agreement with the values reported in literature. The high degree of precision presented by our measurements is directly related to the good sensitivity of the experimental set-up, with a tolerance of about 0.3%. Finally, as shown in Fig. 4, the melting transition occurs around $220 \div 230$ K. In this case, it is believed that the melting temperature for an applied frequency of 1KHz or 100 KHz can be deduced from the slope changes occurred in the conductivity curve carried out as a function of temperature.

Physical Aging

Since the glassy phase is out of the thermodynamic equilibrium, the properties of glassy materials exhibit a time dependence, or Physical Aging, consisting in a molecular rearrangement inside the structure of the polymeric material. As a consequence, physical aging results in a modification of some physical parameters, such as permittivity.[13] Hence, physical aging in PDMS is here displayed by performing the above described permittivity measurements as a function of time. It is worth to remember that the study of aging permittivity is fundamental for possible applications based on the use of PDMS films (such as dielectric barrier in FET devices, packaging, Lab on chip applications).

About our measurements, they started 6 hours after the end of the sample

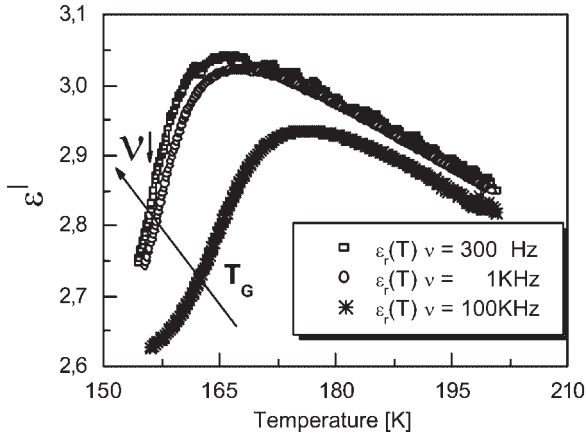

Figure 3.
Permittivity versus Temperature at different fixed values of the a.c. field frequency. T_G depends on the frequency values, as indicated by the black arrow.

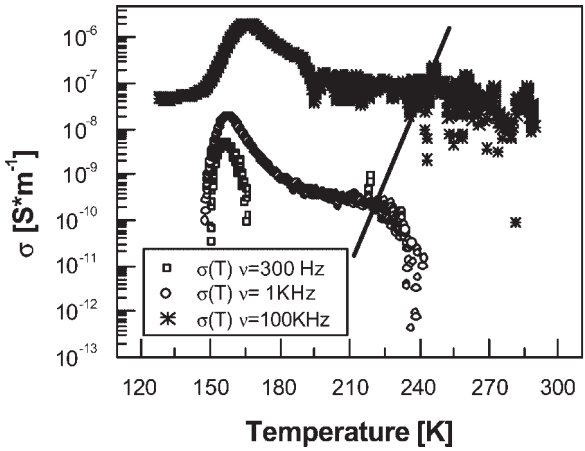

Figure 4.
Conductivity versus Temperature at different fixed values of the a.c. field frequency. TM increases by increasing the frequency of the applied field (black line).

preparation, taking care of keeping them in vacuum as long as possible. The measurements were performed at 1 KHz, in agreement with the IEEE standards,[21] during a range of 7 days, in which the sample underwent a recycling from room temperature to 40 K, always under vacuum.

Fig. 5 reports the $\varepsilon_r(t)$ measurement, normalized to its initial value, at four different temperatures: T = 200 K and T = 75 K are deeply inside the melting and glassy phases, respectively, while T = 170 K and T = 145 K represent the region where the material is partially glassy or crystalline.

The expected trend, consisting in the ε_r lowering as a function of time, is confirmed. The observed aging is less than 0.1%, confirming the high resolution of the technique.

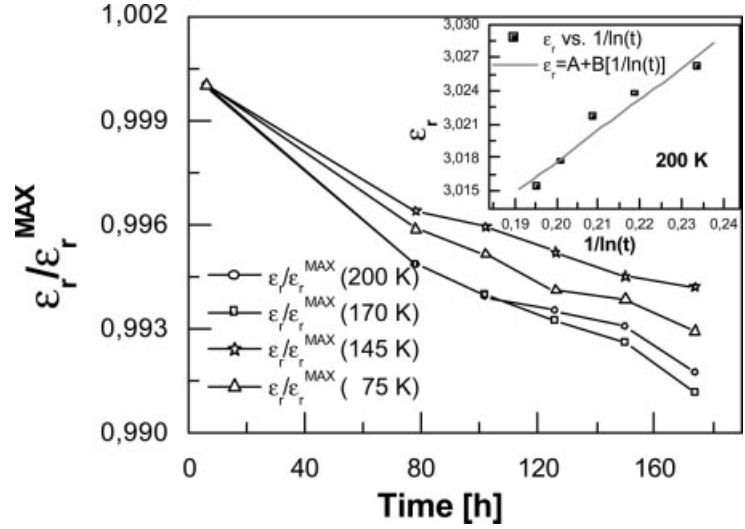

Figure 5.
Permittivity versus time, normalized to its initial value εrMAX, for different temperatures. The aging in the heart of glassy phase (75 K) is slower than that occurred in crystalline phase (200 K).

It is also shown that the aging is slower below T_G, where relaxation mechanisms are less fast, due to the lack of available free volume for the segmental mobility of macromolecules. The time dependent lowering of ε_r follows a typical logarithmic behavior:[22] $\varepsilon_r \approx \frac{1}{\ln(t)}$. To this purpose, in the inset of Fig. 5 it is shown that the predicted behavior fits the curve recorded at 200 K, plotted by linearizing the logarithmic form above mentioned. A more complete study, as a function of frequency in presence of d.c. bias, is under analysis and it will be reported later.

Conclusions

Dielectric measurements represent a simple and powerful tool for the visualization of phase transitions and physical aging in polymeric thin films. In the present work, we have employed such technique on PDMS thin films in order to visualize phase transitions and measure T_G and T_M with a high degree of precision. The extracted values of T_G, equal to 156 K, and T_M, about 220 K, are in very good agreement with those reported in literature.

As far as the physical aging is concerned, we have investigated the lowering of the dielectric constant in four different zones keeping the sample under vacuum for one week. The lowering is slower in the glassy phase, where the rearrangement of macromolecules is frozen. The technique allows to measure aging less than 0,1%.

Acknowledgements: The technical support of A. Maggio and S. Marrazzo is gratefully acknowledged.

[1] J. M. Shaw, P. F. Seidler, *IBM J. RES. & DEV.* **2001**, *45*, 3.
[2] M. Angelopoulos, *IBM J. RES. & DEV.* **2001**, *45*, 57.
[3] V. Podzorov, S. E. Sysoev, E. Loginova, V. M. Pudalov, and M. E. Gershenson., *Appl. Phys. Lett.* **2003**, *83*, 3504.
[4] J. D. Mc Coy, J. G. Curro, *J. Chem. Phys* **2002**, *116*, 9154.
[5] J. L. Keddie, R. A. L. Jones, and R. A. Cory, *Europhys. Lett.* **1994,** *27, 59*.
[6] J. M. Hutchinson, *Thermochim. Acta* **1998**, *324*, 165.
[7] J. Kaifeng, J. F. Löffler, *Appl. Phys. Lett.* **2005**, *86*, 241909.
[8] M. Y. Efremov, E. A. Olson, M. Zhang, Z. Zhang and L. H. Allen., *Phys. Rev. Lett.* **2003**, *91*, 085703.
[9] H. B. Brom, I. G. Romijn, J. G. Magis, M. Van der Vleuten and M. A. J. Michels, *Appl. Phys. Lett.* **2004**, *85*, 570.
[10] Show An Chen, H. T. Lee, *Macromolecules 28*, 2858 **1995**.
[11] T. Sugihara, K. Fujii, H. Haga, and S. Yamamoto, *Appl. Phys. Lett.* **1996**, *69*, 2971.
[12] N. G. Mc Crum, B. E. Read and G. Williams, *Anelastic and Dielectric Effects in Polymeric Solids*, John Wiley and Sons, New York **1967**.
[13] L. C. E. Struik, *Physical Aging in Amorphous Polymers and Other Materials*, Elsevier, Houstion 1978.
[14] B. Bhushan, *Nanotech.* **2005**, *16*, 467.
[15] S. Uemura, M. Yoshida, S. Hoshino, T. Kodzasa, T. Kamata, *Thin Solid Films* **2003**, *438&439*, 378.
[16] V. Podozorov, V. M. Pudalov, M. E. Gershenson, *Appl. Phys. Lett.* **2003**, *82*, 1739.
[17] P. G. Debenedetti, F. H. Stillinger, *Nature* **2001**, *410*, 259.
[18] A. Cassinese, M. Barra, M. Biasiucci, P. D'Angelo, *Macromol. Symp.* **2006**, *234*, 1.
[19] T. Dollase, H. W. Spiess, M. Gottlieb and R. Yerushalmi-Rozen., *Europhys. Lett.* **2002**, *60*, 390.
[20] J. Mark, *Polymer Data Handbook*, Oxford Univ. Press, New York **1999**.
[21] IEEE Standard for Test Methods for the Characterization of Organic Transistors and Materials; IEEE Std 1620TM **2004**.
[22] M. Nicodemi, H. J. Jensen, *Phys. Rev. B* **2001**, *86*, 4378.

